Search for Long-lived Chargino with Anomaly-Mediated Supersymmetry Breaking Scenarios in pp Collisions at $\sqrt{s} = 7$ TeV

A dissertation submitted to
Department of Physics,
Graduate School of Science,
the University of Tokyo
in partial fulfillment of the requirements for the Degree of Doctor of Philosophy

Yuya Azuma
Department of Physics, Graduate School of Science, The University of Tokyo

December 18, 2012

Abstract

A search for long-lived charginos in anomaly-mediated supersymmetry breaking (AMSB) models is performed using 4.7 fb^{-1} data of pp collisions at $\sqrt{s} = 7$ TeV with the ATLAS detector. In the AMSB models, the wino is the lightest gaugino and the lightest chargino and neutralino (as the lightest supersymmetric particle) are dominantly composed of the charged and neutral winos, respectively. Furthermore, the masses of the charged and neutral winos are highly degenerate, which results in a significant lifetime of the chargino. The lightest chargino decays into a neutralino and a soft charged pion. Due to the mass degeneracy, the momentum of the pion originating from the chargino decay is too soft to be reconstructed in collider experiments. The neutralino escapes detection, therefore, the decaying chargino could be identified as a high-momentum track breaking up in the tracking volume (*disappearing track*).

In this dissertation, a method for detecting such chargino tracks is newly developed. The transition radiation tracker (TRT) employed as one of the ATLAS inner detectors, consisting of a lot of drift tubes, is used for the identification of the disappearing track. A large number of associated hits in the TRT detector for the stable charged particles while a smaller number is expected for decaying charginos. By requiring a small number of TRT hits along a track, the chargino track is discriminated to the track of the SM particles.

After the application of selection requirements, three hundred and four candidate tracks remain. The background and signal yields are determined by an unbinned maximum likelihood fit on the pt of the tracks. The p_{T} spectrum of the candidate tracks is consistent with the background-only hypothesis and no excess of data is found.

New constraints on the chargino properties and the AMSB model parameters are then set. A chargino having a lifetime $\tau_{\tilde{\chi}_1^\pm} = 1$ ns is excluded up to $m_{\tilde{\chi}_1^\pm} \sim 120$ GeV in the region $m_{\frac{3}{2}} > 2000$ GeV at 95% Confidence Level (CL). For a chargino having a lifetime $\tau_{\tilde{\chi}_1^\pm} = 0.3$ ns, a constraint of $m_{\tilde{\chi}_1^\pm} > 100$ GeV in the region $m_{\frac{3}{2}} > 2000$ GeV is set at 95% CL.

This thesis is dedicated to my dear family, especially to my late grandparents Shizu Hatakenaka, Tadao Hatakenaka and Sadao Azuma.

Acknowledgments

I wold like to express my gratitude to many people for writing up my dissertation. I think I could not accomplish this study without instruction, help and encouragement from a number of people.

I wish deliver an address of thanks to my supervisor, Prof. Shoji Asai. While I have been a student of the graduate school, I have learned a lot from a particle physics to an attitude for the research. He always indicates the right way which I should go and his powerful voice roused me into activity. It is my great fortune that I have been spent my doctorate course.

I deeply appreciate Prof. Shimpei Yamamoto for his eager instruction, technical support and encouragement in my Ph.D period. He gave me a variety of important advices and great encouragement on my study. I really appreciate him for teaching me kindly. Without his help, my dissertation would never have completed.

I would like to express my thanks to Prof. Osamu Jinnouchi for his advice. Since I was in master course, he gave me zealous instruction on the physics analysis and the Monte Calro simulations. When I was stumbled by a difficulty, he gave me kind and patient assistance.

I would like to express my appreciation to Prof. Tomio Kobayashi, Prof. Katsuo Tokushuku and Prof. Takahiko Kondo for giving me the golden opportunity to participate in the ATLAS experiment. I am very grateful to the all staff of ICEPP at CERN, Prof. Tatsuo Kawamoto, Prof. Naoko Kanaya, Prof. Junichi Tanaka, Prof Ikuo Ueda, Prof. Koji Terashi, Prof. Yousuke Kataoka, Dr. Taiki Yamamura, Prof. Koji Nakamura and Dr. Tatsuya Masubuchi. They gave me sincere advice about basic techniques for data analysis or an excellent computing environment. I also would like to thank Prof. Tetsuro Mashimo, Prof. Yoshizumi Inoue, Prof. Hiroyuki Matsunaga, Prof. Tadaaki Isobe, Prof. Tomoaki Nakamura and Mr. Nagataka Matsui for providing me a marvelous computing environment at Tokyo.

I want to express my gratitude to Ms. Kuniko Kono and secretaries of ICEPP, Ms. Ritsuko Anbiru, Ms. Masako Shiota, Ms. Yoko Takemoto, Ms. Akiko Miyazono, Ms. Yoshie Tezuka, Ms. Megumi Suzuki, Ms. Chieko Morita, Ms. Naoko Kataoka, Ms. Eiko Yuno and Ms. Hiroko Yakushi. They have helped me a lot on paperwork and gave me secretarial supports. I want to thank all of ATLAS secretaries for their sincere help with administrative supports.

It is my great honor to express my gratitude to the members of the ATLAS collaboration for giving me a opportunity to join in this experiment. Furthermore, I would like to express my thanks to all the LHC crews for providing us a excellent data.

I appreciate the conveners and the collaborators of the SUSY working group. The conveners of the SUSY working group, Prof. George Redlinger, Prof. Pascal Pralavorio and Prof. Andreas Hoecker gave me incisive comments and excellent suggestion for physics analysis. I also

Contents

List of Figures

10

13

List of Tables

15

Chapter 1

Introduction

1.1 Symmetry

Symmetry is the most important concept in physics[1, 2] and is the property that the description of the system is invariant under some transformations. Many physicists have been attracted to symmetry as ever. Emmy Nöther is one of the greatest mathematicians. The Nöther's theorem disclaims that some conserved currents exists if the system is invariant under a continuous transformation. For example, the conservation of energy is equivalent to the time transformation symmetry. Moreover, the momentum conservation and the angular momentum conservation follow from the space transformation symmetry and the space rotation symmetry respectively.

Symmetry is important also in the particle physics. The Standard Model (SM) describes the three interactions: the electromagnetic interaction, the weak interaction and the strong interaction. The SM is the theory based on the internal symmetry of $SU(3) \times SU(2) \times U(1)$. Furthermore, Peter Higgs put forward a model that *Spontaneous Symmetry Breaking* gives masses to gauge bosons. In the Weinberg-Salam theory, the gauge symmetry is broken by considering "wine bottle potential "and weak bosons achieve masses due to this breaking. As physics beyond SM, *Supersymmetry* is introduced for the SM. Supersymmetry is the symmetry relating fermions and bosons and expected to exist because some problems in physics are solved if the symmetry exists.

This dissertation is devoted the search for a supersymmetry particle inspired by a supersymmetry model.

1.2 The Standard Model

All of the matters in the world consist of elementary particles[3]. Elementary particles contain quarks, leptons and gauge bosons.

Table 1.1 shows the summary of quarks and leptons. They have spin-$\frac{1}{2}$ and are categorized as fermions. Baryons such as protons or neutrons, and mesons such as pions are called hadrons. Quarks are elements of hadrons. Electrons, muons, taus and neutrinos are categorized as leptons. Quarks and leptons are divided into three generations. Table 1.2 shows the summary of gauge bosons. The gauge boson is a carrier of force:the gluon (g) carries the strong interaction,

Table 1.1: Quarks and leptons in the Standard Model. S, Q, T^3 and Y are Spin, charge, the third component of weak isospin and weak hypercharge, respectively.

	Particles			S	Q	T^3	Y
Quarks	$\begin{pmatrix} u \\ d \end{pmatrix}_L$	$\begin{pmatrix} c \\ s \end{pmatrix}_L$	$\begin{pmatrix} t \\ b \end{pmatrix}_L$	$\frac{1}{2}$	$\begin{pmatrix} \frac{2}{3} \\ -\frac{1}{3} \end{pmatrix}$	$\begin{pmatrix} \frac{1}{2} \\ -\frac{1}{2} \end{pmatrix}$	$\frac{1}{3}$
	u_R	s_R	t_R	$\frac{1}{2}$	$\frac{2}{3}$	$\frac{1}{2}$	$\frac{4}{3}$
	d_R	c_R	b_R	$\frac{1}{2}$	$-\frac{1}{3}$	$-\frac{1}{2}$	$-\frac{2}{3}$
Leptons	$\begin{pmatrix} \nu_e \\ e^- \end{pmatrix}_L$	$\begin{pmatrix} \nu_\mu \\ \mu^- \end{pmatrix}_L$	$\begin{pmatrix} \nu_\tau \\ \tau^- \end{pmatrix}_L$	$\frac{1}{2}$	$\begin{pmatrix} 0 \\ -1 \end{pmatrix}$	$\begin{pmatrix} \frac{1}{2} \\ -\frac{1}{2} \end{pmatrix}$	-1
	e_R^-	μ_R^-	τ_R^-	$\frac{1}{2}$	-1	0	-2

weak bosons ($W^\pm$ and Z^0) carry the weak interaction and photons (γ) carry the electromagnetic interaction. The graviton considered as a carrier of gravity but is not yet discovered. Furthermore, Higgs boson which is the origin of mass is expected to be discovered at the LHC.[1]

Table 1.2: Gauge bosons in the Standard Model.

		S	Q	T^3	Y
gluino	g	1	0	0	0
Weak boson	$W^\pm$	1	±1	±1	0
	Z^0	1	0	0	0
photon	γ	1	0	0	0

1.3   Supersymmetry

Supersymmetry is a symmetry between bosonic and fermionic degrees of freedom[6, 7, 8, 9]. Various problems in the modern physics are expected to be solved if supersymmetry exists.

1.3.1   History of Supersymmetry

The first concept of supersymmetry is put forward by H.Miyazawa in 1966[10]. This idea is the symmetry on mesons and baryons. However, this concept did not attract physicists' attention of those days. It is in the 1970s that the idea of supersymmetry on elementary particle are published. Supersymmetry is proposed by Yu.A.Golfand and E.P.Likhtman (1971) [11], D.V.Volkov and V.P.Akulov (1972)[12], and J.Wess and B.Zumino(1974) [13]. In 1981, H.Georgi and S.Dimopoulos extends the Standard Model minimally with the concept of supersymmetry[14]. This model is called the Minimal Supersymmetric Standard Model or the MSSM for short.

---

[1]In the summer of 2012 , ATLAS and CMS which are experiments at LHC claimed the discovery of Higgs-boson like particle[4, 5].

1.3.2 Issues in Physics and Supersymmetry

There are some of benefits for existing supersymmetry. Various issues are expected to be solved by the supersymmetry.

- Unification of gauge coupling
  Gauge couplings changes with energy and the all gauge couplings are expected to be unified in high energy region, which is called GUT scale. However, the unification of couplings is impossible if only the Standard Model is considered. By assuming TeV scale SUSY, the slope of coupling constant changes. As a result, the unification is achieved in the supersymmetric model. Figure 1.1 shows the evolution of the coupling constants in the Standard Model and the model with the supersymmetry assumption [15].
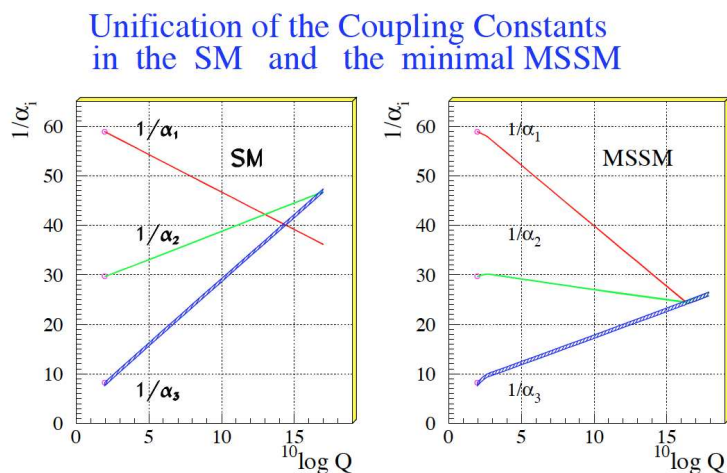
Figure 1.1: The inverse of coupling constants as a function of the energy scale. The unification of the coupling constants is failed if only the SM is assumed. Gauge coupling constants are unified in the MSSM [15].

- Hierarchy problem
  This is the problem that there is a huge difference between the Planck scale and the electroweak scale. The electroweak sector of the Standard Model have a parameter called the vacuum expectation value. This parameter sets the scale of masses of bosons. The mass of the $W^\pm$ is given by

$$M_W = \frac{1}{2}vg,$$ (1.1)

where v is the vacuum expectation value of the neutral Higgs field and g is the $SU(2)$ gauge coupling constant. The mass of the Higgs boson is given by

$$M_H = v\sqrt{-2\lambda},$$ (1.2)

where λ is the strength of the Higgs self-interaction in the Higgs potential. This is the only discussion at tree level and by considering one-loop correction. If the Higgs field couples to a Dirac fermion f with a term in the Lagrangian $-\lambda_f H\bar{f}f$, where λ_f is the

Yukawa coupling constant, the quadratic correction from a loop of a fermion added to M_H^2 is expressed as

$$\delta M_H^2 = -\frac{1}{8\pi^2}|\lambda_f|^2 \Lambda_{\text{UV}}, \tag{1.3}$$

where Λ_{UV} is an ultraviolet momentum cutoff. If there is none of new physics up to Planck scale and Λ_{UV} is set at the Planck mass

$$M_p = (G_{\text{Newton}})^{\frac{1}{2}} \approx 1.2 \times 10^{19} \text{ GeV}, \tag{1.4}$$

the correction is extremely greater than $O((100 \text{ GeV})^2)$. Therefore, *fine-tuning* is needed to lead the electroweak scale with a remarkable cancellation.

If there is a heavy complex scalar particle S having a mass m_S that couples to the Higgs with a Lagrangian term $-\lambda_S |H|^2 |S|^2$,

$$\delta M_H^2 = 2\frac{1}{16\pi^2}\lambda_S \Lambda_{\text{UV}}, \tag{1.5}$$

If mass correction from the both of fermions and bosons with $\lambda_S = |\lambda_f|^2$, the contributions from Λ_{UV} is clearly canceled out.

- A good candidate of the dark matter
  Experimental cosmology suggests the existence of the dark matter. The dark matter scarcely make interaction with other matter. A good candidate of the dark matter is the lightest supersymmetric particle (LSP).

1.3.3 Particles of the Standard Model and Their Superpartner

In the supersymmetric model, there are supersymmetric particles which correspond to the Standard Model particles. They are called *superpartner*. The Standard Model particles and the supersymmetric particles, which is also called *sparticles* for short, are summarized in the Table 1.3.

Partners of fermions in the Standard Model such as quarks or leptons has spin-0. Their name have "s"as a prefix. For example, the bosonic partner of quarks and leptons are called *squarks* and *sleptons*. The bosonic partner of fermions is also called *sfermions*. On the other hand, the names of fermionic partner of bosons in the Standard Model have "ino"as a suffix. Fermionic partners of gauge boson, Higgs boson and Graviton are *gaugino*, *higgsino* and *gravitino*, respectively. Gaugino and higgsino has spin-$\frac{1}{2}$ while gravitino has spin-$\frac{3}{2}$.

In the supersymmetric model, there are two complex Higgs $SU(2)_L$ doublets:

$$H_u = \begin{pmatrix} H_u^+ \\ H_u^0 \end{pmatrix} \tag{1.6}$$

and

$$H_d = \begin{pmatrix} H_d^0 \\ H_d^- \end{pmatrix}. \tag{1.7}$$

H_u^+, H_u^0, H_d^0 and H_d^- are complex numbers. Hence, there are eight real scalar degrees of freedom in the Higgs doublet. Three of them become the longitudinal modes of the massive vector

bosons $W^\pm$ and Z^0. The mass eigenstates of the other five are referred as H,h,A and $H^\pm$. The lightest higgs h has a properties similar to the SM higgs and the other four higgs have heavier masses.

Gauginos are *wino*($\tilde{W}^0,\tilde{W}^\pm$), *bino*($\tilde{B}^0$) and *gravitino*($\tilde{g}$) The electroweak gauge symmetry $SU(2)_L \times U(1)_Y$ is associated with spin-1 gauge bosons W^0, W^+, W^- and B^0. Mass eigenstates γ (photon), Z^0 (Z-boson) are given by mixing of the W^0,B^0 after the electroweak symmetry braking. The superpartners of gauge eigenstates W^0 and B^0 are $\tilde{W}^0$ and $\tilde{B}^0$. Neutral gauginos ($\tilde{W}^0$ and $\tilde{B}^0$) and neutral higgsinos ($\tilde{H}_1^0,\tilde{H}_2^0$) make mixing and result in *neutralinos* ($\tilde{\chi}_1^0, \tilde{\chi}_2^0, \tilde{\chi}_3^0, \tilde{\chi}_4^0$). Charged winos and charged higgsinos are also mixed to *charginos* ($\tilde{\chi}_1^\pm, \tilde{\chi}_2^\pm$).

Table 1.3: Particles in the minimal supersymmetric standard model

The Standard Model particles		Supersymmetric particles	
Names	Spin	Names	Spin
quarks (u,d,s,c,b,t)	$\frac{1}{2}$	squarks ($\tilde{u},\tilde{d},\tilde{s},\tilde{c},\tilde{b},\tilde{t}$)	0
leptons ($e,\mu,\tau,\nu_e,\nu_\mu,\nu_\tau$)	$\frac{1}{2}$	sleptons ($\tilde{e},\tilde{\mu},\tilde{\tau},\tilde{\nu}_e,\tilde{\nu}_\mu,\tilde{\nu}_\tau$)	0
gauge bosons ($\gamma,W^\pm,Z^0,g$)	1	gauginos ($\tilde{B}^0,\tilde{W}^0,\tilde{W}^\pm,\tilde{g}$)	$\frac{1}{2}$
Higgs bosons ($H,h,A,H^\pm$)	0	higgsinos ($\tilde{H}_1^0,\tilde{H}_2^0,\tilde{H}^\pm$)	$\frac{1}{2}$
graviton (G)	2	gravitino ($\tilde{G}$)	$\frac{3}{2}$

1.3.4 R-parity

In the MSSM, the new symmetry which is called *R-parity* is postulated. Using baryon number (B), lepton number (L) and spin (S), R-parity, P_R is defined as

$$P_R = (-1)^{3(B-L)+2S}. \tag{1.8}$$

The Standard Model particles have $P_R = +1$ while sparticles have $P_R = -1$.

If R-parity is conserved, there is no mixing between the SM particles and sparticles. Furthermore, the number of sparticles is even in every interaction vertex. Additionally, some of important consequences are obtained. Firstly, the lightest supersymmetric particle, which is also called *LSP* must be stable. Secondly, sparticles except for LSP decay to the state that there is an odd number of LSPs. Thirdly, an even number of sparticles are produced in collider experiments.

In the most of supersymmetric models, this symmetry is assumed from the point of view of proton decay constraints or good candidate for the dark matter.

1.3.5 Supersymmetry Breaking

If there is exact invariance under supersymmetry, there expected to be a particle having the same mass and the same quantum number with a different spin by one-half. However, such particles is not observed in nature. It means that the our world is not exactly invariant under the supersymmetry. The superpartner of the SM particle are expected to have a heavier mass than the SM particles due to this reason.

There are various models depending on mechanisms of the supersymmetry breaking. The supersymmetry breaking is considered to come to our world through some interactions from the

origin of the supersymmetry breaking, which is called *Hidden Sector*. The major models are listed below:

- Supergravity-Mediated Supersymmetry Breaking (SUGRA)
  The supersymmetry breaking is mediated by the gravity from the hidden sector to our observable world in this model. It is assumed that the all scalar particles have a common mass at GUT scale. In this model, the lightest gaugino is bino. Therefore, The LSP is a bino-like $\tilde{\chi}_1^0$.

- Gauge-Mediated Supersymmetry Breaking (GMSB)
  Gauge interactions communicates the effects of supersymmetry breaking in this models. There is another set of fields that has both SM gauge interactions and a couplings with a hidden sector. This sector is referred as *Messenger Sector*. $\tilde{G}$ is a the LSP in this model. In some case, $\tilde{\tau}$ or $\tilde{\chi}_1^0$ become the NLSP and they have a long lifetime. In the case that $\tilde{\tau}$ is the NLSP, the decay of $\tilde{\tau}$ is $\tilde{\tau} \to \tau \tilde{G}$. The lifetime of $\tilde{\tau}$ is expected to be long enough to penetrate whole detector. The $\tilde{\tau}$ is expected to be detected as a *Massive Stable Particle* or *Kink Track*. In the case that $\tilde{\chi}_1^0$ is the NLSP, the decay of $\tilde{\chi}_1^0$ is $\tilde{\chi}_1^0 \to \gamma \tilde{G}$. The $\tilde{\chi}_1^0$ signal is expected to be detected as *Non-Pointing Photon*.

- Anomaly-Mediated Supersymmetry Breaking (AMSB)
  The supersymmetry breaking is mediated by a conformal anomaly. This model is a simple model because it does not require such as Messenger Sector in GMSB. However, the model require m_0 for the masses of sfermions in order to prevent sfermions becoming tachyons. The details on this model are described in Section 1.4.

1.3.6 Masses of Sparticles

Parameters in the MSSM

There are many parameters in the MSSM. In various supersymmetric models, some assumptions are introduced and the number of parameters is lessen. The parameters widely used in the several models are listed here.

1. m_0 : Mass of scalar particle at GUT scale.

2. $m_{\frac{1}{2}}$: Gaugino mass at GUT scale.

3. $m_{\frac{3}{2}}$: Gravitino mass.

4. μ : Higgsino mass parameter.

5. $\tan\beta$: the ratio of the vacuum expectation values of doublet.

Moreover, three gaugino mass parameters are widely used: M_1, M_2 and M_3 are bino mass, wino mass and gluino mass, respectively.

Gluino Mass

The gluino is the only color octet fermion and can not mix with any other fermion because $SU(3)$ is unbroken. The mass of the gluino at tree level is simply

$$m_{\tilde{g}} = M_3. \tag{1.9}$$

Chargino Mass

The higgsinos and electroweak gauginos (wino and bino) mix with each other. The positively charged pair $(\tilde{W}^+, \tilde{H}_u^+)$ mix to form two eigenstates with charge $+1$. On the other hand, the negatively charged pair $(\tilde{W}^-, \tilde{H}_d^-)$ mix to form two eigenstates with charge -1. Using the eigenstate basis $\psi^\pm = (\tilde{W}^+, \tilde{H}_u^+, \tilde{W}^-, \tilde{H}_d^-)$, the mass term of charginos is

$$-\frac{1}{2}(\psi^\pm)^T M \psi^\pm, \tag{1.10}$$

where

$$M = \begin{pmatrix} \mathbf{0} & X^T \\ X & \mathbf{0} \end{pmatrix} \tag{1.11}$$

with

$$X = \begin{pmatrix} M_2 & \sqrt{2}\sin\beta m_W \\ \sqrt{2}\cos\beta m_W & \mu \end{pmatrix}. \tag{1.12}$$

From here, $(m_{\tilde{\chi}_1^\pm}^2, m_{\tilde{\chi}_2^\pm}^2)$ is obtained,

$$\begin{pmatrix} m_{\tilde{\chi}_1^\pm}^2 \\ m_{\tilde{\chi}_2^\pm}^2 \end{pmatrix} = \begin{pmatrix} \frac{1}{2}\left[(M_2^2 + |\mu|^2 + 2m_W^2) - \sqrt{(M_2^2 + |\mu|^2 + 2m_W^2) - 4|\mu M_2 - m_W^2 \sin 2\beta|^2}\right] \\ \frac{1}{2}\left[(M_2^2 + |\mu|^2 + 2m_W^2) + \sqrt{(M_2^2 + |\mu|^2 + 2m_W^2) - 4|\mu M_2 - m_W^2 \sin 2\beta|^2}\right] \end{pmatrix}. \tag{1.13}$$

By assuming M_2 and μ is real and $M_2 < \mu$, the eigenvalues are given by $m_{\tilde{\chi}_1^\pm} \approx M_2$ and $m_{\tilde{\chi}_2^\pm} \approx \mu$. In this assumption, $\tilde{\chi}_1^\pm$ becomes wino-like and $\tilde{\chi}_2^\pm$ becomes higgsino-like.

Neutralino Mass

The neutral higgsinos $(\tilde{H}_u^0, \tilde{H}_d^0)$ and the neutral gauginos $(\tilde{B}, \tilde{W}^0)$ combine to form four mass eigenvalues. Using the gauge-eigenstate basis $\psi^0 = (\tilde{B}, \tilde{W}^0, \tilde{H}_u^0, \tilde{H}_d^0)$,

$$-\frac{1}{2}(\psi^0)^T M \psi^0, \tag{1.14}$$

where

$$M = \begin{pmatrix} M_1 & 0 & -\cos\beta\sin\theta_W m_Z & \sin\beta\sin\theta_W m_Z \\ 0 & M_2 & \cos\beta\cos\theta_W m_Z & -\sin\beta\cos\theta_W m_Z \\ -\cos\beta\sin\theta_W m_Z & \cos\beta\cos\theta_W m_Z & 0 & -\mu \\ \cos\beta\sin\theta_W m_Z & -\sin\beta\cos\theta_W m_Z & -\mu & 0 \end{pmatrix}. \tag{1.15}$$

The mass matrix M is diagonalized by a unitary matrix N in order to obtain mass eigenstates,

$$\tilde{\chi}_i^0 = N_{ij}\psi_j^0. \tag{1.16}$$

By the calculation similarly to the chargino case, the eigenvalue of M is obtained.

Squarks and Sleptons

In many models such as SUGRA or GMSB, their running masses can be given as,

$$m_{\tilde{u}_L,\tilde{d}_L}^2 = m_{\tilde{c}_L,\tilde{s}_L}^2 = m_0^2 + K_3 + K_2 + \frac{1}{36}K_1, \tag{1.17}$$

$$m_{\tilde{u}_R}^2 = m_{\tilde{c}_R}^2 = m_0^2 + K_3 + \frac{4}{9}K_1, \tag{1.18}$$

$$m_{\tilde{d}_R}^2 = m_{\tilde{s}_R}^2 = m_0^2 + K_3 + \frac{1}{9}K_1, \tag{1.19}$$

$$m_{\tilde{\nu}_{eL},\tilde{e}_L}^2 = m_{\tilde{\nu}_{\mu L},\tilde{\mu}_L}^2 = m_0^2 + K_2 + \frac{1}{4}K_1, \tag{1.20}$$

$$m_{\tilde{e}_R}^2 = m_{\tilde{\mu}_R}^2 = m_0^2 + K_2 + K_1, \tag{1.21}$$

where K_1, K_2 and K_3 are mentioned as the renormalization gauge equation (RGE) contributions which are corresponding to the square gaugino mass. Roughly, the RGE contributions are,

$$K_1 \sim 0.15m_{\frac{1}{2}}^2, \quad K_2 \sim 0.5m_{\frac{1}{2}}^2, \quad K_3 \sim (4.5 \approx 6.5)m_{\frac{1}{2}}^2. \tag{1.22}$$

On the other hand, the sfermion mass in the AMSB model is expressed as,

$$m_{\tilde{f}}^2 = -\{\cdots\}m_{\frac{3}{2}}^2 + m_0^2, \tag{1.23}$$

where the $m_{\frac{3}{2}}^2$ term is the anomaly-mediated contribution to the scalar mass parameter. As mentioned before, the sfermion mass is amended by adding m_0^2 in order to make sfermion masses positive.

1.3.7 Production of Sparticles

Production process of QCD strength

Reactions of QCD strength at the hadron collider are

$$gg \to \tilde{g}\tilde{g}, \tag{1.24}$$

$$gq \to \tilde{g}\tilde{q}, \tag{1.25}$$

$$gg \to \tilde{q}\tilde{q}, \tag{1.26}$$

$$qq \to \tilde{q}\tilde{q}. \tag{1.27}$$

The process in (1.24) is gluino pair production process and Feynman diagrams of this process are shown in Figure 1.2. Gluino squark associate production process is shown as (1.25) and in Figure 1.3. The process in (1.26) and (1.27) is known as squark pair production process and diagrams of this process is shown in Figure 1.4.

Hard collision of partons is needed in order to produce heavy particles such as sparticle. Contributions from gluon-gluon collision, gluon-quark collision and quark-quark collision are large at proton-proton collider like LHC. There are also contributions from quark-antiquark collision and these processes are important at proton-antiproton collider like Tevatron.

(a)   (b)   (c)
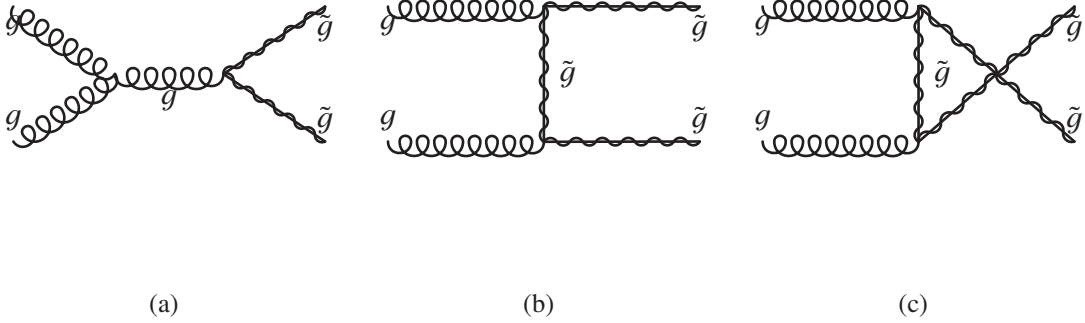
Figure 1.2: Feynman diagrams for gluino pair production process.

(a)   (b)   (c)
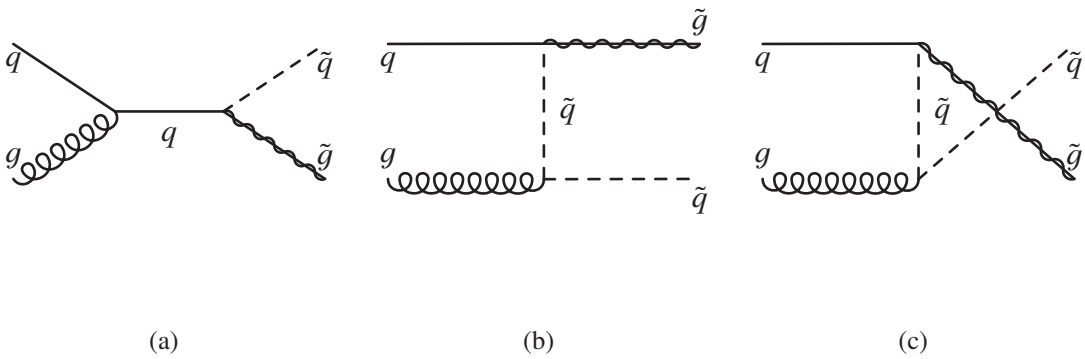
Figure 1.3: Feynman diagrams for gluino squark associate production process.

(a)   (b)   (c)

(d)   (e)
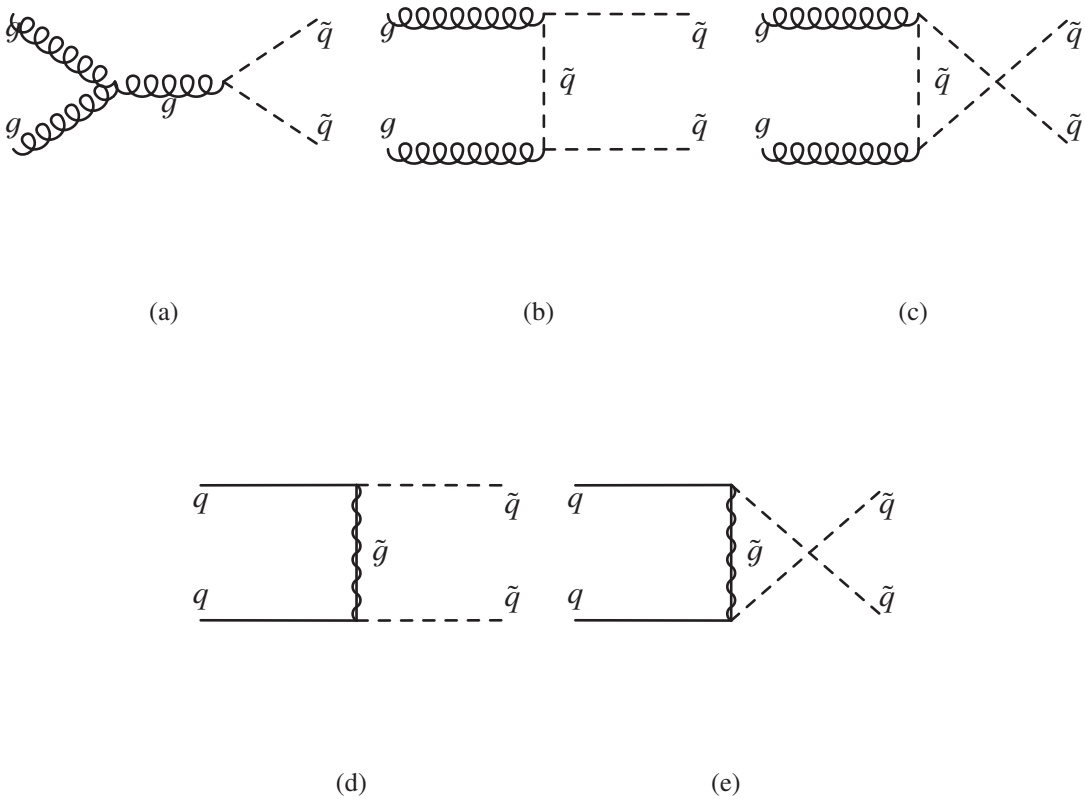
Figure 1.4: Feynman diagrams for squark pair production process.

Production Process of Electroweak Strength

Reactions in (1.28) - (1.33) are production process of sparticles are via parton collisions of electroweak strength.

$$q\bar{q} \to \tilde{\chi}_i^+ \tilde{\chi}_j^-, \tilde{\chi}_i^0 \tilde{\chi}_j^0 \tag{1.28}$$

$$u\bar{d} \to \tilde{\chi}_i^+ \tilde{\chi}_j^0 \tag{1.29}$$

$$d\bar{u} \to \tilde{\chi}_i^- \tilde{\chi}_j^0 \tag{1.30}$$

$$q\bar{q} \to \tilde{l}_i^+ \tilde{l}_j^-, \tilde{\nu}_i \tilde{\nu}_j \tag{1.31}$$

$$u\bar{d} \to \tilde{l}_L^+ \tilde{\nu}_l \tag{1.32}$$

$$d\bar{u} \to \tilde{l}_L^- \tilde{\nu}_l \tag{1.33}$$

These reactions have contributions from electroweak gauge bosons in s-channel and from squark exchange in t-channel. These process are important at the Tevatron collider.

1.3.8 Decays of Sparticles

In this section, the decay pattern of sparticles in the MSSM is shown. By assuming that R-parity is conserved, the decays of gluino, squarks, sleptons, charginos and neutralinos are described qualitatively.

Gluino Decays

The gluino decays can be occurred via either on-shell squarks or virtual squarks. When the two-body decay, $\tilde{g} \to q\tilde{q}$ is possible, this process is dominant.

If the mass of the all squarks is heavier than the gluino mass, then the two-body decay is impossible. In this case, the three-body decay through virtual squarks occurs: $\tilde{g} \to qq'\tilde{\chi}^0$ or $\tilde{g} \to qq'\tilde{\chi}^\pm$.

Squarks Decays

If the two-body decay, $\tilde{q} \to q\tilde{g}$ is possible, this process is dominant. If this is not the case, squarks decay to charginos or neutralinos, that is, $\tilde{q} \to q\tilde{\chi}^\pm$ or $\tilde{q} \to q\tilde{\chi}^0$. In this case, The direct decay to the LSP such as $\tilde{\chi}_1^0$ is favored. For instance, in the case bino is the lightest in some models such as mSUGRA, right-handed squarks ($\tilde{q}_R$) decay to $\tilde{\chi}_1^0$ ($\tilde{q}_R \to q\tilde{\chi}_1^0$) dominantly.

However, left-handed squarks ($\tilde{q}_L$) tend to decay to heavier charginos or neutralinos ($\tilde{q}_L \to q\tilde{\chi}_2^0$ or $\tilde{q}_L \to q\tilde{\chi}_1^\pm$) because the squark-quark-wino coupling is much bigger than squark-quark-bino coupling. The squark decay to higgsino-like charginos and neutralinos is not very important except for the case stops or sbottoms decay. Stops and sbottoms have sizable Yukawa couplings.

If two-body decay such as $\tilde{t}_1 \to t\tilde{g}$ or $\tilde{t}_1 \to t\tilde{\chi}_1^0$ is open, then the lighter stop may makes two-body decay to chargino ($\tilde{t}_1 \to b\tilde{\chi}^\pm$) or the three-body decay to neutralino ($\tilde{t}_1 \to bW\tilde{\chi}^0$). Even if these decays are kinematically forbidden, flavor-suppressed decay to charm quarks ($\tilde{t}_1 \to b\tilde{\chi}^0$) or four-body decay ($\tilde{t}_1 \to bff'\tilde{\chi}^0$) can be happened. In this case, these decays can be occurred in late and the lighter stop is quasi-stable and hadronized into bound state.

Slepton decays

Sleptons decay to leptons plus charginos or neutralinos: $\tilde{l} \rightarrow l\tilde{\chi}_i^0$, $\tilde{l} \rightarrow \nu\tilde{\chi}_i^\pm$, $\tilde{\nu} \rightarrow \nu\tilde{\chi}_i^0$ and $\tilde{\nu} \rightarrow l\tilde{\chi}_i^\pm$. These decay modes have strength of weak interaction. The direct decays to the lightest neutralino ($\tilde{l} \rightarrow l\tilde{\chi}_1^0$ and $\tilde{\nu} \rightarrow \nu\tilde{\chi}_1^0$) is kinematically allowed when $\tilde{\chi}_1^0$ is the LSP. Furthermore, modes of two-body decay to the heavier charginos or neutralinos such as $\tilde{l} \rightarrow l\tilde{\chi}_2^0$, $\tilde{l} \rightarrow \nu\tilde{\chi}_1^\pm$, $\tilde{\nu} \rightarrow \nu\tilde{\chi}_2^0$ and $\tilde{\nu} \rightarrow l\tilde{\chi}_1^\pm$ also have to be considered.

Right-handed sleptons do not have the coupling to $SU(2)_L$ gauginos. For that reason, two-body decay of these sleptons ($\tilde{l}_R \rightarrow l\tilde{\chi}_1^0$) occurs when $\tilde{\chi}_1^0$ is the LSP and bino-like. On the other hand, left-handed sleptons decay to $\tilde{\chi}_1^\pm$ or $\tilde{\chi}_2^0$ if these decay modes are kinematically allowed and $\tilde{\chi}_1^\pm$ or $\tilde{\chi}_2^0$ are wino-like.

Chargino Decays

Charginos are admixtures of charged wino and charged higgsino. Charginos decay to the lighter chargino or neutralino plus Higgs boson or electroweak gauge bosons ($\tilde{\chi}_i^\pm \rightarrow W^\pm\tilde{\chi}_j^0$, $\tilde{\chi}_i^\pm \rightarrow Z^0\tilde{\chi}_1^\pm$ and $\tilde{\chi}_i^\pm \rightarrow h^0\tilde{\chi}_1^\pm$). Additionally, if sleptons or squarks are sufficiently light, the decays of charginos to lepton plus slepton or to quarks plus squarks are open ($\tilde{\chi}_i^\pm \rightarrow l\tilde{\nu}$, $\tilde{\chi}_i^\pm \rightarrow \nu\tilde{l}$ and $\tilde{\chi}_i^\pm \rightarrow q\tilde{q}'$). However, decay modes to heavier Higgs such as $\tilde{\chi}_i^\pm \rightarrow A^0\tilde{\chi}_1^\pm$, $\tilde{\chi}_i^\pm \rightarrow H^0\tilde{\chi}_1^\pm$ and $\tilde{\chi}_i^\pm \rightarrow H^\pm\tilde{\chi}_j^0$ are unlikely because h^0 is required to be light

One or more of decay modes of the heavier chargino $\tilde{\chi}_2^\pm$ is kinematically allowed. Furthermore, if the decay of the chargino which has sizable component of higgsino to third-generation quark plus squarks are open, this mode is enhanced by top-quark Yukawa coupling.

When two-body decay are forbidden, chargino makes three-body decay such as $\tilde{\chi}_i^\pm \rightarrow ff'\tilde{\chi}_j^0$ and $\tilde{\chi}_2^\pm \rightarrow ff'\tilde{\chi}_1^0$.

Neutralino Decays

Neutralinos are admixtures of bino, neutral wino and neutral higgsino. Hence, decays of neutralinos can be considered in the same way as chargino. Possible decay modes of neutralino are,

- Two-body decays to lighter neutralino or chargino plus Higgs boson or electroweak gauge boson

  $\tilde{\chi}_i^0 \rightarrow Z^0\tilde{\chi}_j^0$, $\tilde{\chi}_i^0 \rightarrow W^\pm\tilde{\chi}_j^\mp$ and $\tilde{\chi}_i^0 \rightarrow h^0\tilde{\chi}_1^0$

- Two-body decays to sleptons or squarks in the case sleptons or squarks are light

  $\tilde{\chi}_i^0 \rightarrow l\tilde{l}$, $\tilde{\chi}_i^0 \rightarrow \nu\tilde{\nu}$ and $\tilde{\chi}_i^0 \rightarrow q\tilde{q}$

- Three-body decays when two-body decays are forbidden

  $\tilde{\chi}_i^0 \rightarrow ff\tilde{\chi}_j^0$ and $\tilde{\chi}_i^0 \rightarrow ff'\tilde{\chi}_j^\pm$.

1.4 Anomaly-Mediated Supersymmetry Breaking

Anomaly mediation of supersymmetry breaking [16, 17] is very attractive for the anomaly mediation is the simplest mechanism since the mediation of supersymmetry breaking. This mechanism occurs in any supersymmetry models.

In the minimal anomaly mediated supersymmetry breaking models, three gaugino masses (M_1,M_2 and M_3) can be given with the gravitino mass and the gauge coupling at TeV scale:

$$M_1 = \frac{g_1^2}{16\pi^2}(\frac{33}{5}m_{\frac{3}{2}}),$$ (1.34)

$$M_2 = \frac{g_2^2}{16\pi^2}(m_{\frac{3}{2}}),$$ (1.35)

$$M_3 = \frac{g_3^2}{16\pi^2}(-3m_{\frac{3}{2}}),$$ (1.36)

where g_1,g_2 and g_3 are the gauge coupling constants of $U(1)$,$SU(2)$ and $SU(3)$ gauge groups, respectively. The wino mass is the lightest of the three gaugino mass. Therefore, the lightest neutralino and chargino are expected to be wino-like. The charged wino becomes slightly heavier than the neutral wino by radiative correction. So the LSP is the lightest wino-like neutralino ($\tilde{\chi}_1^0$) and the NLSP is the lightest wino-like chargino($\tilde{\chi}_1^\pm$). The wino-like chargino and neutralino with near-degeneracy indicate the important phenomenological feature [18]. Near-degenerate particles are not unusual in SUSY phenomenology. The small mass difference $\Delta M_\chi = M_{\tilde{\chi}_1^\pm} - M_{\tilde{\chi}_1^0}$ leads to the long lifetime of the lightest chargino. The lightest chargino may have a lifetime long enough to be reconstructed as a charged track with a detector. Figure 1.5 shows the life-
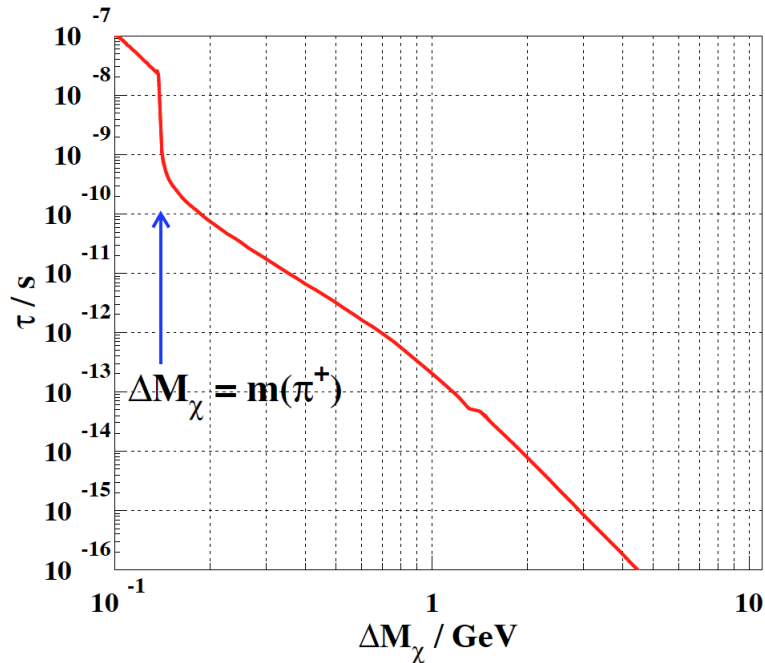
Figure 1.5: The lifetime of the lightest chargino as a function of the mass difference ΔM_χ [18].

time of the lightest chargino as a function of the mass difference ΔM_{χ}. A lifetime of the lightest chargino having the mass difference which is around the pion mass (140 MeV) corresponds to $O(0.1) \sim O(1)$ ns. The chargino mass in this analysis is assumed to be around 100 GeV and the mass difference of this chargino corresponds to about the pion mass. Hence, the analysis for AMSB charginos relies on the search for tracks of the lightest charginos.

In this case, $\tilde{\chi}_1^{\pm}$ decays into $\tilde{\chi}_1^0$ with low-momentum charged particles:

$$\tilde{\chi}_1^{\pm} \to \tilde{\chi}_1^0 + \pi^{\pm}, \tag{1.37}$$

$$\tilde{\chi}_1^+ \to \tilde{\chi}_1^0 + e^+ \nu \ (\tilde{\chi}_1^- \to \tilde{\chi}_1^0 + e^- \bar{\nu}) \tag{1.38}$$

Neutralino or low-momentum charged particles is hard to be detected. The signal of decaying chargino in the tracking volume is expected to be exotic. The methods for identifying chargino track is mentioned in Chapter 4.

In the AMSB scenarios, the universal scalar mass at GUT scale needs to be large otherwise the scalar leptons becomes tachyons. Then all of sfermions becomes too heavy to be produced in proton-proton collisions at $\sqrt{s} = 7$ TeV. Due to the relatively large masses of squarks, a very precise fine-tuning of parameters is needed to obtain the correct electroweak symmetry breaking, which solves many serious problems of the standard SUSY models. First, the flavor-changing neutral current and CP-violation problems become very milder thanks to the larger masses of squarks and sleptons. Second, AMSB gives a natural explanation to no discovery of proton decay induced by dimension-five operators.

1.4.1 Recent Results of the Long-lived Charginos

The recent search for the long-lived charginos was performed by experiments at LEP2 [19, 20, 21]. These analyses are based on the search for events with the ISR photon. The combined results in the LEP2 search excludes chargino having a mass < 92 GeV[22]. Figure 1.6 shows the constraint on a long-lived charginos obtained by the combination of the results of the LEP2 experiments.A chargino having a mass $M_{\tilde{\chi}_1^{\pm}} < 92$ GeV for $\Delta M \equiv M_{\tilde{\chi}_1^{\pm}} - M_{\tilde{\chi}_1^0}$ of about 150 MeV is excluded.

The long-lived chargino search is also performed with the ATLAS detector with 1.0 fb^{-1}data [23]. The analysis with 1.0 fb^{-1} data is also based on the search for the chargino track. The results presented in this dissertation are obtained by the extension of the analysis of 1.0 fb^{-1} data. Figure 1.7 shows the constraint on the chargino mass and lifetime with 1.0 fb^{-1} data. A chargino having a mass $m_{\tilde{\chi}_1^{\pm}} < 92$ GeVand lifetime $0.5 < \tau_{\tilde{\chi}^{\pm}} < 2.0$ ns is excluded in the framework of minimal AMSB model by the analysis of 1.0 fb^{-1} data and the results comparable to the LEP2 search are obtained.

1.5 Outline of Dissertation

- Chapter 1
  In this chapter, physics motivation of this study presented in this dissertation is described. The recent results concerning to this study is also shown.
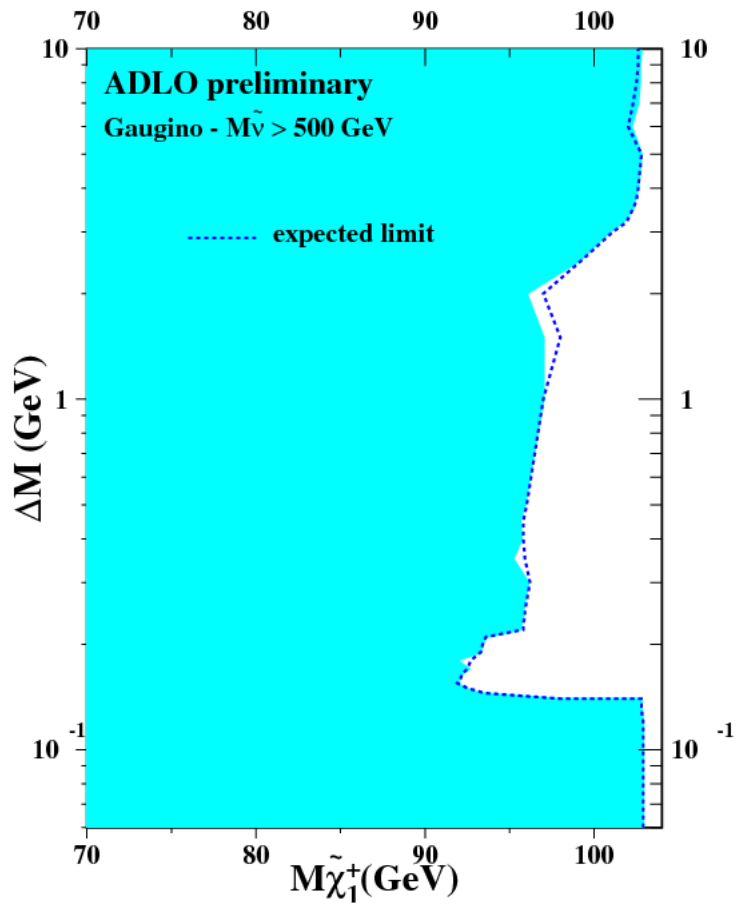
Figure 1.6: The constraint on long-lived chargino obtained by combination of the results of LEP2 experiments[22].
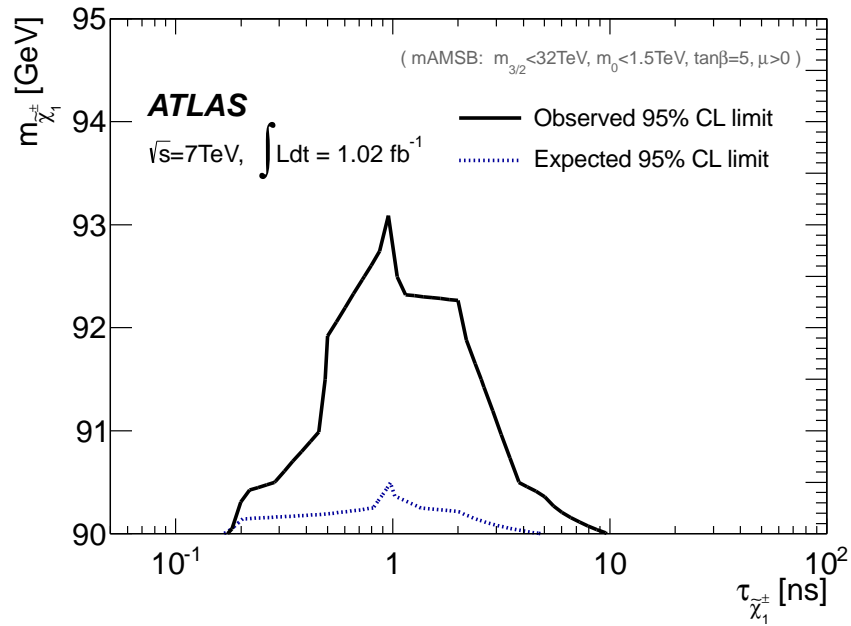
Figure 1.7: The constraint on the chargino mass and lifetime with 1.0 fb^{-1}data. The observed bound is set at 95% CL and a chargino having a mass $m_{\tilde{\chi}_1^\pm} < 92$ GeVand lifetime $0.5 < \tau_{\tilde{\chi}_1^\pm} < 2.0$ ns is excluded [23].

- Chapter 2

  The details of the experimental apparatus in this research are shown. This analysis is performed by using data of pp collision at $\sqrt{s} = 7$ TeV provided by Large Hadron Collider. The data is collected by the ATLAS detector.

- Chapter 3

  As a contributions to the ATLAS collaboration, performance study of the TRT using cosmic data is performed. The studies of TRT detector are shown here.

- Chapter 4

  The methods dedicated for identifying chargino track are newly developed. The character of chargino track, the methods for identification of chargino and the event topology of AMSB events are described.

- Chapter 5

  The details of object reconstruction of ATLAS data are summarized here. The dataset and Monte Carlo simulation are also described.

- Chapter 6

  In accordance with the event topology, the selection in this search is summarized.

- Chapter 7

  The studies on the backgrounds in this analysis are described. The properties of backgrounds are investigated. The control samples extracted by using these properties are made use of estimation of backgrounds and extraction of signal yields.

- Chapter 8

  The systematic uncertainties in this analysis are investigated.

- Chapter 9

  In this chapter, background estimation and signal extraction are performed. For the estimation, simultaneous fitting method is employed. The details of fitting method, fitting results and validation of the fitting are shown.

- Chapter 10

  Using the results of the analysis, the physical interpretation is given in this chapter.

- Chapter 11

  The summary of this dissertation is described.

Chapter 2

Experimental Apparatus

2.1 Large Hadron Collider

Large Hadron Collider (LHC) [24] is a two-ring superconducting pp accelerator collider which is designed to have the center-of-mass energy $\sqrt{s} = 14$ TeVand the luminosity is 10^{34} cm^{-2}s^{-1}. It is installed in the tunnel which is 26.7km long. The main goal of the LHC is the discovery of the physics beyond the Standard Model.

Various experiments are held at the LHC. Two high luminosity experiments are ATLAS [25] and CMS [26]. These experiments are operated at peak luminosity $L = 10^{34}$ cm^{-2}s^{-1} for proton-proton collision. Two low luminosity experiments are LHCb[27] and TOTEM [28]. LHCb is operated at peak luminosity $L = 10^{32}$ cm^{-2}s^{-1}. TOTEM is operated at peak luminosity $L = 2 \times 10^{29}$cm^{-2}s^{-1}. Moreover, one heavy ion experiment is ALICE [29]. ALICE is operated at peak luminosity $L = 10^{27}$ cm^{-2}s^{-1} for lead-lead ion collision. The energy of Pb ions 2.8 TeVper nucleon.

Figure 2.1: Large Hadron Collider

2.1.1   Injection Chain

The LHC is supplied with proton beams by the injector chain shown in Figure 2.2. The injector chain consists of LINAC2, Proton Synchrotron Booster (PSB), Proton Synchrotron (PS) and Super Proton Synchrotron (SPS).

In the early stage of the injector chain, protons are accelerated by linear accelerator which is called LINAC2. The proton sources is a duoplasmon. Protons from duoplasmon are sent to LINAC2, which is a linear accelerator of protons. LINAC2 accelerates protons up to 50 MeV. Beam current results in 180 mA. Proton beam is sent to the PSB.

The PSB is a synchrotron which consists of four superposed rings of 25m radius. It accelerates protons from LINAC2 up to 1.4 GeVand send them to the PS.

The PS is also a synchrotron which is about 628m circumference. In the PS protons are accelerated up to 25 GeV.

Proton beam from the PS is sent to the SPS. The SPS is a synchrotron of approximately 7km circumference. It accelerates protons up to 450 GeVand sent to the LHC ring. The SPS was running as a proton-antiproton collider called Sp$\bar{p}$S in 1980's. It contributed to the discovery of W and Z bosons[30, 31, 32, 33].
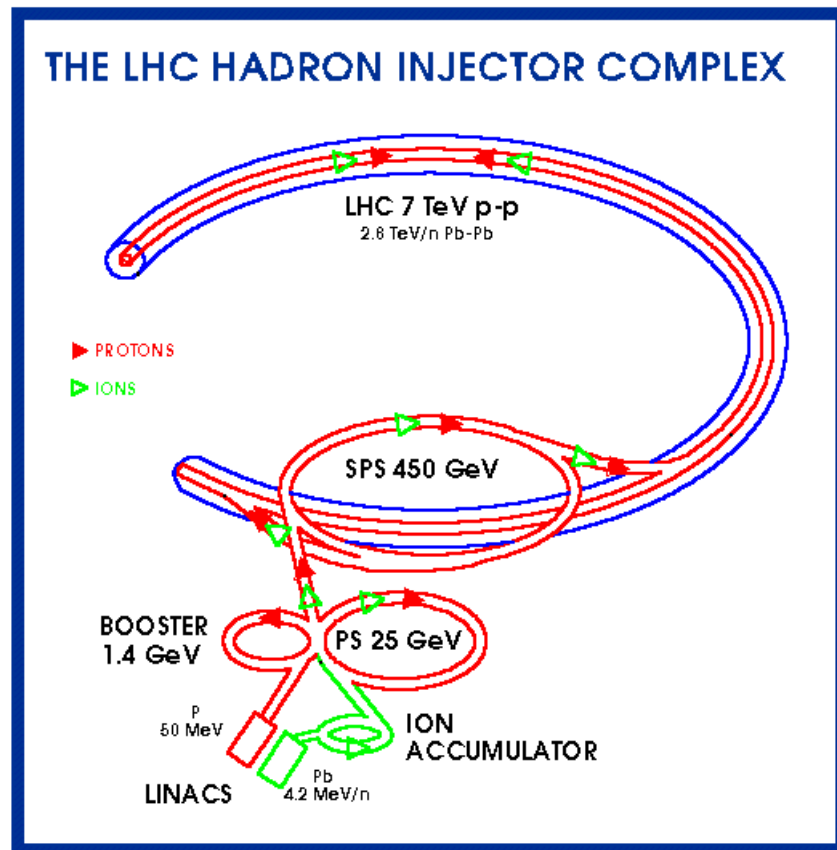
Figure 2.2: The LHC injector complex.

2.1.2 Main Machine Layout

The LHC main ring is installed in the LEP tunnel. LHC consists of eight arcs and eight straight sections. The straight section is 528m long and has experimental insertions. The layout of LHC lattice is shown in Figure 2.3. Two high luminosity experiments are arranged on the opposite points:ATLAS is located at Point 1 and CMS is located at Point 5. ALICE and LHCb are located at Point 2 and Point 8, respectively. At the remaining four sections there are no beam crossings. There are two collimation systems at each Point 3 and 7. The insertion at Point 4 are two RF systems. There are beam dump insertions at Point 6. An arc of LHC consists of 23 arc cells. An arc cell is 106.9m long and is separated to two half cells of 53.45m long. Each half cell contains three 14.3m dipole magnet, cryostat and a short straight section (SSS). Two aperture of Ring 1 and Ring 2 are separated by 194mm.

The LHC uses superconducting magnets similarly to the other large accelerator such as Tevatron or RHIC. The LHC magnet system uses NiTi cables, cools magnets to approximately 4.2K by superfluid helium and operates at magnetic fields above 8T. Almost all of the superconducting magnet is two-in-one structure due to space limitation. The LHC ring has 1232 main dipole magnets.
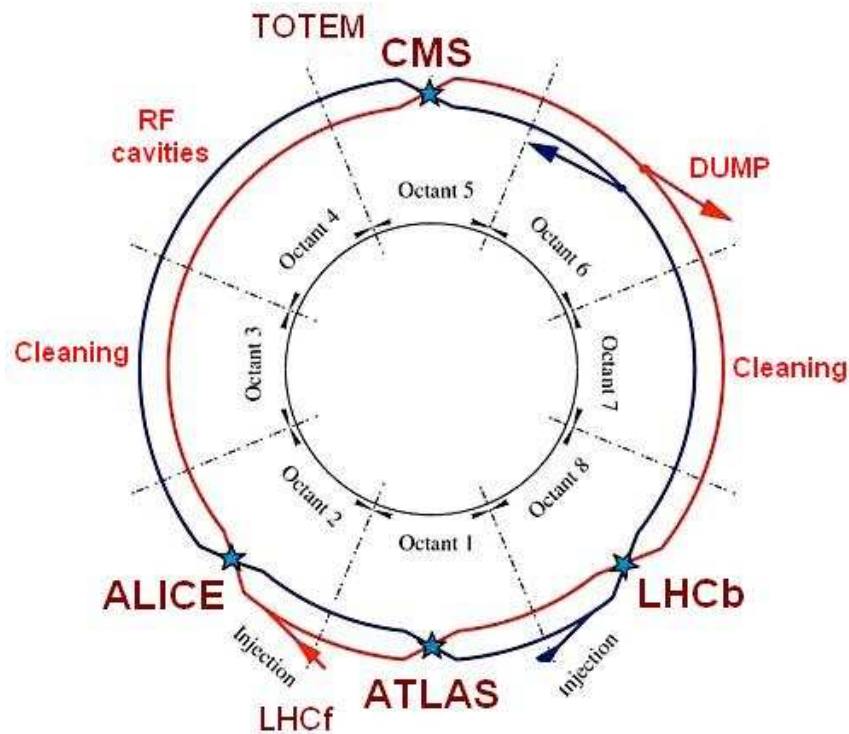
Figure 2.3: The layout of the LHC lattice.

2.1.3 The LHC Performance

The designed parameter of the LHC is summarized in Table 2.1.

The number of bunches is 2808. The number of protons per bunches is 1.15×10^{11}. Bunch length is 7.55cm. Bunch spacing is 25ns.

Table 2.1: LHC design parameters

Maximum proton energy	7 TeV
Number of bunches	2808
Bunch length (r.m.s)	7.5 cm
Circumference of ring	26658.883 m
Frequency of bunch collision	25 ns
Number of collision point	4
Injection energy	450 GeV
Number of particles per bunch	1.15×10^{11}
Luminosity	$10^{34}\text{cm}^{-2}\text{s}^{-1}$

The main goal of the LHC is revealing physics beyond the Standard Model. The LHC is designed to achieve the center of mass energies of 14 TeV. Designed peak luminosity is $10^{34}\text{cm}^{-2}\text{s}^{-1}$. The LHC is operated with the center of mass energies of 7 TeVin 2011.

2.2 The ATLAS Detector

The ATLAS (A Toroidal LHC Apparatus) detector [34, 35] is one of the multi purpose detector at LHC experiments. Discovery of Higgs particle or the particle which is beyond the Standard Model such as supersymmetry model is expected in this experiment. The ATLAS detector covers nearly 4π around the collision point. The height is 25m and the length is 44m. The overview of the ATLAS detector is shown in Figure 2.4.
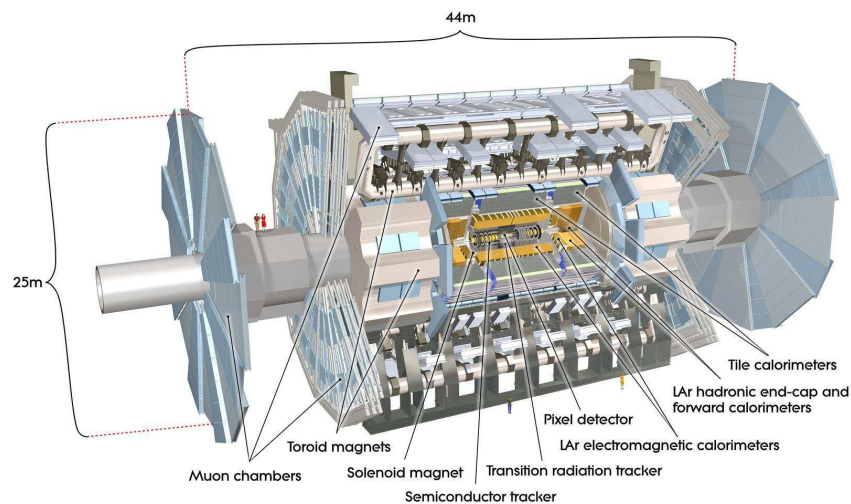
Figure 2.4: The overview of the ATLAS detector.

2.2.1 ATLAS Coordinate

ATLAS uses a right-handed coordinate system. The origin is the nominal interaction point (IP) which is the center of the detector. The z-axis is along with the beam-pipe and the x-axis points to the center on the LHC-ring.

Cylindrical coordinate (r, ϕ, z) are used in the transverse plane. The definition of the r,ϕ is

$$r = \sqrt{x^2 + y^2}, \tag{2.1}$$

$$\phi = \arctan(\frac{y}{x}). \tag{2.2}$$

Furthermore, the polar angle θ is defined as,

$$\theta = \arctan(\frac{r}{z}). \tag{2.3}$$

The rapidity y_{rap} is defined as

$$y_{\mathrm{rap}} \equiv \frac{1}{2}\ln(\frac{E + p_z}{E - p_z}), \tag{2.4}$$

where E and p_z are the energy and the momentum in z-direction of a particle.

The pseudo-rapidity η is also often used in collider physics. This variable is the limit of the rapidity as the mass of a particle approaches zero and expressed with the polar angle as

$$\eta = -\ln(\tan(\frac{\theta}{2})). \tag{2.5}$$

The region that $\eta > 0$ is called A-side, on the other side the region that $\eta < 0$ is called c-side.

Furthermore, the distance in the η-ϕ plane is frequently used in analyses. This variable is defined as,

$$\Delta R \equiv \sqrt{(\eta_i - \eta_j)^2 + (\phi_i - \phi_j)^2}, \tag{2.6}$$

where $\eta_{i(j)}$ and $\phi_{i(j)}$ are pseudo-rapidity and azimuthal angle of $i(j)$-th object.

2.2.2 Magnet System

ATLAS has four superconductive magnet subsystem. The magnet system is 22 m in diameter and 26 m in length. A stored energy is 1.6 GJ.

The spacial arrangement of the magnet system is shown in Figure 2.5. The ATLAS magnet system consists of a central solenoid magnet, a barrel toroid magnet and two end-cap toroid magnets. A barrel solenoid is aligned on the beam axis. It provides a 2 T axial magnetic field for the inner detector. A barrel toroid and two end-cap toroids produce a toroidal magnetic fields of around $0.5 \sim 1$ T for the muon spectrometers.
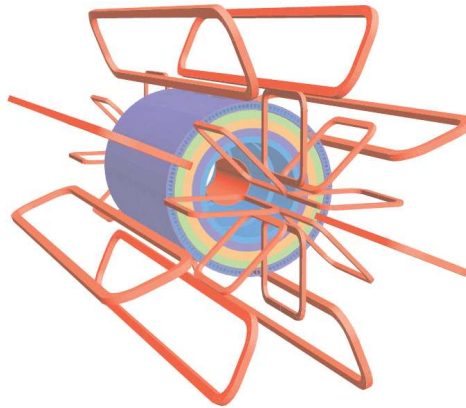
Figure 2.5: The overview of ATLAS magnet system.

Central Solenoid Magnet

Figure 2.6 displays the central solenoid. The central solenoid magnet is designed for tracking of charged particles with the inner detector. It is surrounding the inner detector and is along with beam axis.

Figure 2.7 shows the dependencies for r and z of the radial and axial magnetic field components. It provides a 2T axial magnetic field for the Inner Detector. The solenoid magnetic fields drops steeply from nearly 1.8 T at $z = 1.7$ m to 0.9 T at the end of the cavity of the inner detector. The flux is returned by the steel of the ATLAS hadronic calorimeter. The inner and
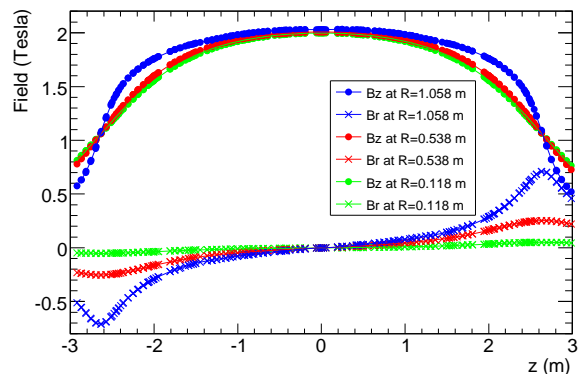
Figure 2.6: The central solenoid magnet of AT-LAS.

Figure 2.7: Dependencies for r and z of the radial and axial magnetic field components in the inner detector cavity.

outer diameters of solenoid are 2.46 and 2.56 m, respectively. Its axial length is 5.8 m. The single layer coil is wound with a NbTi conductor. The radiation length of the magnet results in ~ 0.66 at nominal incidence. The parameters of the central solenoid magnet is shown in Table 2.2.

Table 2.2: Parameters of the central solenoid

Inner diameter	2.46 m
Outer diameter	2.56 m
Axial length	5.8 m
Number of coils	1
Mass	5.7 t
Turns per coil	1154
Nominal current	7.73 kA
Stored energy	0.04 GJ
Peak field in the windings	2.6 T
Field range in the bore	0.9-2.0 T

Toroid Magnet

Figure 2.8 (a) and (b) show the barrel and end-cap magnets, respectively. Table 2.3 is the summary of the parameters of the toroid magnets.

This system is designed for the precise measurement of muons. The toroidal magnet fields enable to measure the momentum for low-p_T muon by bending for θ-direction. Magnetic field made by the toroid magnetic system is not uniform. The toroidal magnetic field has not only ϕ component but also z component.
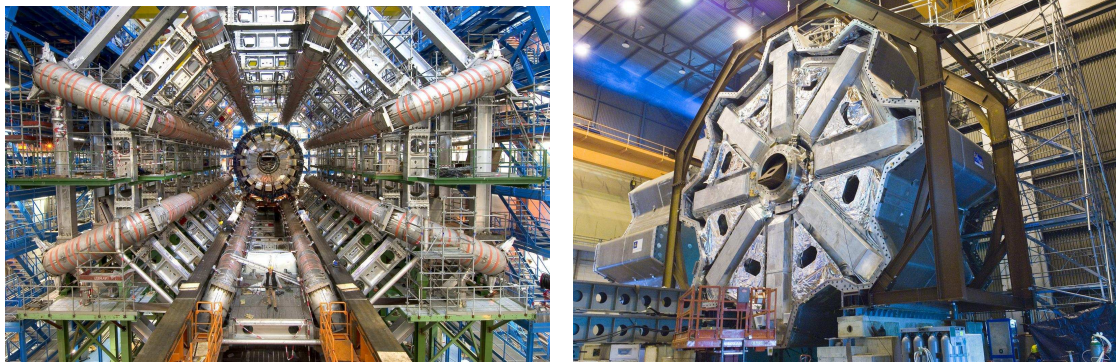
(a) Barrel toroid magnet   (b) End-cap toroid magnet

Figure 2.8: Toroid magnets of the ATLAS. (a) is barrel toroid magnet and (b) is end-cap toroid magnet.

Figure 2.9 shows the field integral as a function of $|\eta|$ from the innermost to the outermost MDT layer in one toroid octant. A good magnetic field covers up to $|\eta| \sim 2.6$.

Barrel Toroid The barrel toroid system is shown in Figure 2.8 (a). The overall size of the system is 25.3 m length, the inner diameter of 9.4 m and the outer diameter of 20.1 m.

This system consists of eight coils encased in racetrack-shaped and stainless-steel vacuum vessel. The barrel toroid system is arranged with eight-fold rotational symmetry for beam-axis.

Table 2.3: Parameters of barrel and end-cap toroid magnets

Property	Barrel toroid	End-cap toroid
Inner diameter	9.4 m	1.65 m
Outer diameter	20.1 m	10.7 m
Axial length	25.3 m	5.0 m
Number of coils	8	2×8
Mass	830 t	2×239 t
Turns per coil	120	116
Nominal current	20.5 kA	20.5 kA
Stored energy	1.08 GJ	2×0.25 GJ
Peak field in the windings	3.9 T	4.1 T
Field range in the bore	0.2-2.5 T	0.2-3.5 T
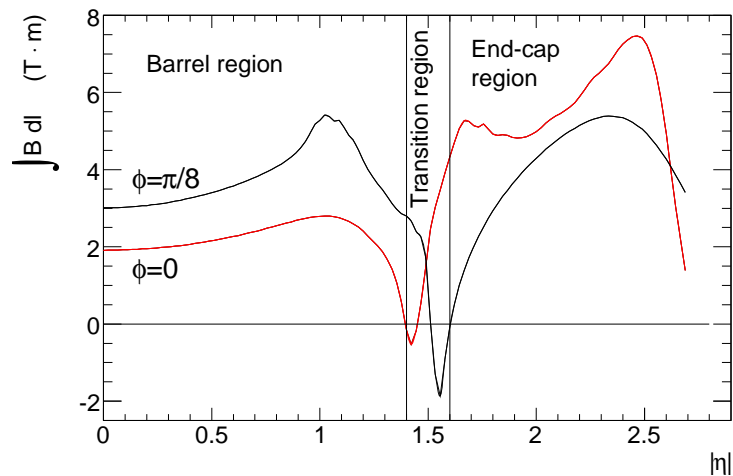
Figure 2.9: Predicted magnetic field integral as a function of $|\eta|$ from the innermost to the outermost MDT layer in one toroid octant. The red and black lines corresponds to $\phi = 0$ and $\phi = \pi/8$, respectively.

40

End-cap Toroid The main parameters are listed in Table 2.3 and the end-cap toroid is shown in Figure 2.8 (b). The end-cap toroid system is 5.0 m length, the inner diameter of 1.65 m and the outer diameter of 10.7 m.

This system is also arranged with eight-fold rotational symmetry.

2.2.3   Inner Detector

The Inner Detector [36, 37] is the innermost detector of the ATLAS detector. The Inner Detector is designed for the tracking of the charged particles.

Figure 2.10 shows the side-view of the Inner Detector of the ATLAS. The Inner Detector consists of three sub-detectors, that is, pixel detector, Semiconductor Tracker (SCT) and Transition radiation Tracker (TRT). Figure 2.11 shows the cross section of the Inner Detector. The Inner Detector is contained within a cylindrical envelope of length ±3512 mm and of radius 1150mm. The Inner Detector is surrounded by the solenoid magnet. The magnetic field up to the 2T is applied for the Inner Detector in order to track charged particles. The detail of the solenoid magnet is described in Section 2.2.2.
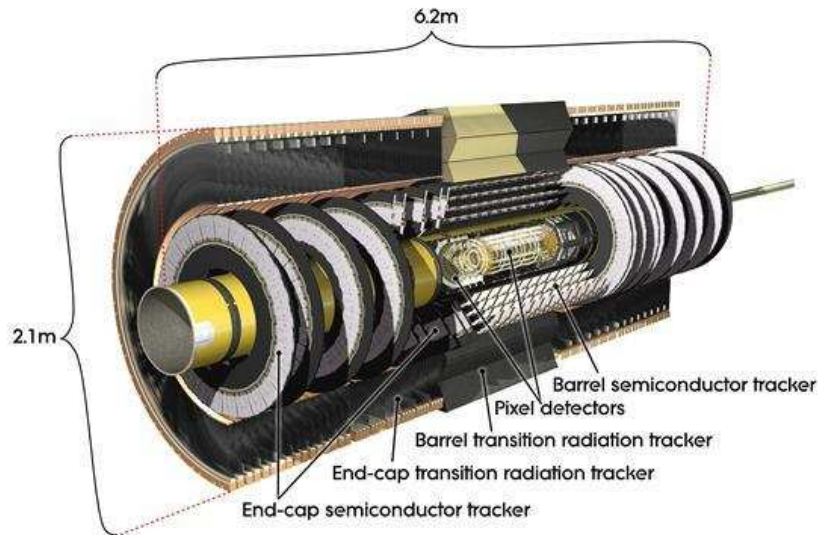
Figure 2.10: The overview of Inner Detector.

Figure 2.12 and 2.13 show the sensors and structural elements traversed by 10 GeV tracks in the barrel and end-cap regions, respectively. The charged track at $|\eta| = 0.3$ traverses successively the beam-pipe, the three cylindrical pixel layers, the four cylindal double layers of barrel SCT and approximately 36 straws contained in the barrel TRT modules. The charged track at $|\eta| = 1.4$ traverses successively the beam-pipe, the three cylindrical pixel layers, four of the disks with double layers of the end-cap SCT and approximately 40 straws contained in the end-cap TRT. The track at $|\eta| = 2.2$ traverses successively the beam-pipe, only the first of the cylindrical pixel layers, two end-cap pixel disks and the last four disks of the end-cap SCT.
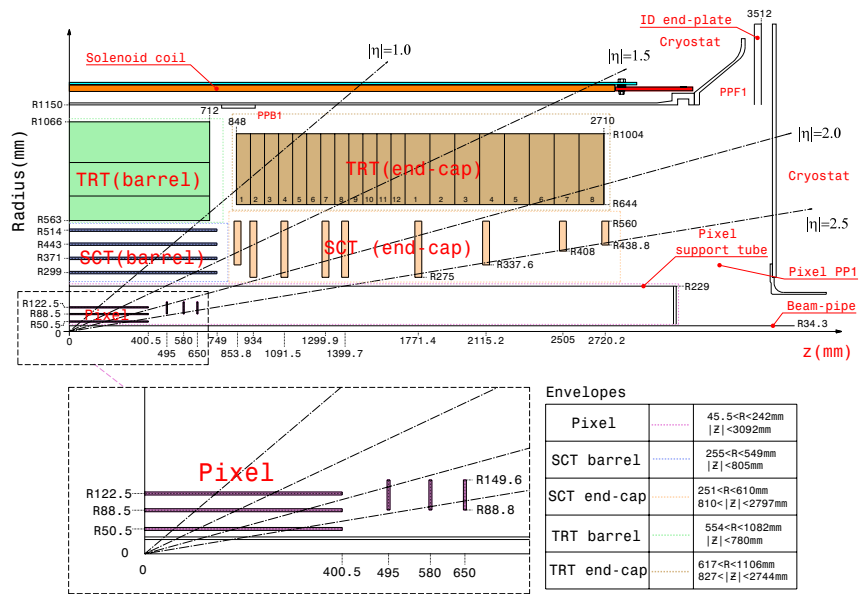
Figure 2.11: The cross section of the Inner Detector on *r-z* plane. Each of the major detector elements with its active dimensions and envelops is shown.
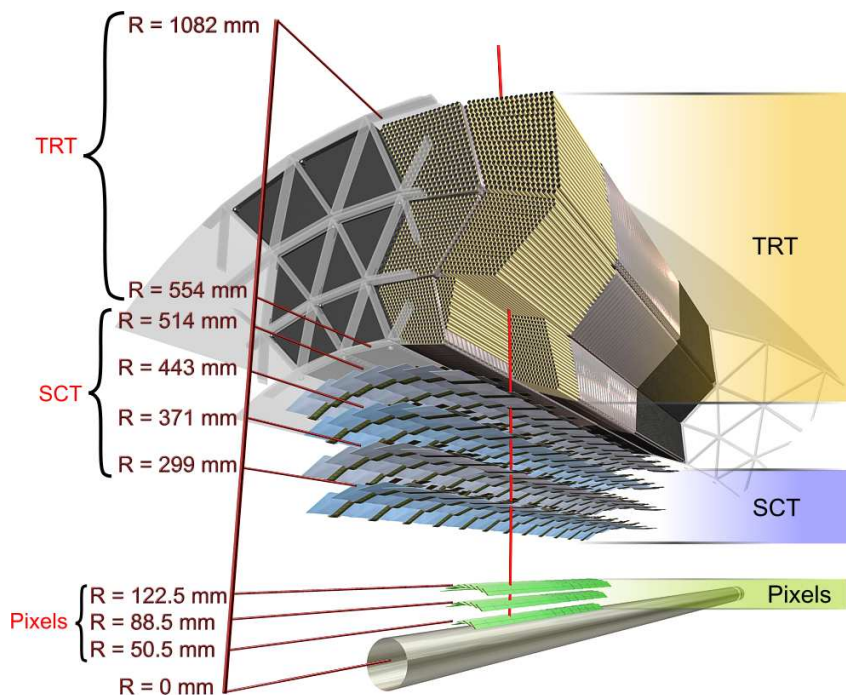
Figure 2.12: Drawing of the sensors and the structural elements traversed by a charged track of 10 GeV in the barrel region ($|\eta| = 0.3$).
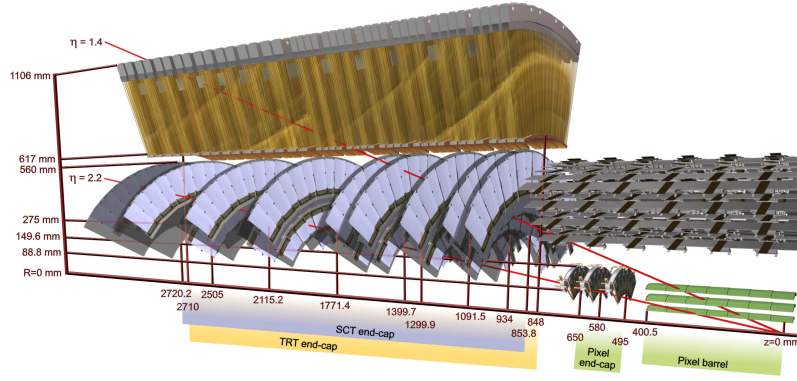
Figure 2.13: Drawing of the sensors and the structural elements traversed by a charged track of 10 GeV in the end-cap region ($|\eta| = 1.4$ and 2.2).

Pixel Detector

The nearest detector to the beam-pipe is the Pixel detector. The pixel detector has fine granularity. The parameters of the Pixel detector are summarized in Table 2.4.

All 1744 pixel sensors on each module are identical. Operating voltage is about 150V. Nominal size of each pixel is $50 \times 400\mu$ m and there are 47232 pixels on each sensor. However, there are ganged pixels on the sensor due to the reason for the space. The total number of readout channels are 46080. In or PbSn are used for bump bonds by which pixel sensors are connected to the readout channels. The pixel sensor is 63.4×24.4mm^2 and of approximately 250μm thick.

The pixel detector has three layers in the barrel region and three disks in the end-cap region on each side. The innermost layer is also called *b-layer*.

Figure 2.14 (a) and (b) show the barrel stave and the end-cap disk of the Pixel detector, respectively. There are 112 staves in total for the barrel. 13 pixel modules are mounted on each stave For the end-cap region, a total of 48 sectors exists and each disk has eight sectors. Six pixel modules are mounted on each sectors. Totally, there are 144 pixel modules on each side for the end-cap region.

Table 2.4: Parameters of the pixel detector

Barrel	r(mm)	Number of staves	Number of modules	Number of pixels
Layer-0	50.5	22	286	13.2×10^6
Layer-1	88.5	38	494	22.8×10^6
Layer-2	122.5	52	676	31.2×10^6
End-cap ($\times 2$)	$|z|$(mm)	Number of sectors	Number of modules	Number of pixels
Disk 1	495	8×2	48×2	$2.2 \times 10^6 \times 2$
Disk 2	580	8×2	48×2	$2.2 \times 10^6 \times 2$
Disk 3	650	8×2	48×2	$2.2 \times 10^6 \times 2$
Barrel and both end-cap			1744	80.4×10^6

Particle position can be measured with the accuracy of 12μm on the $r - \phi$ plane and the 110 μm on $z-$direction by using Pixel detector.

(a) Barrel module   (b) End-cap module
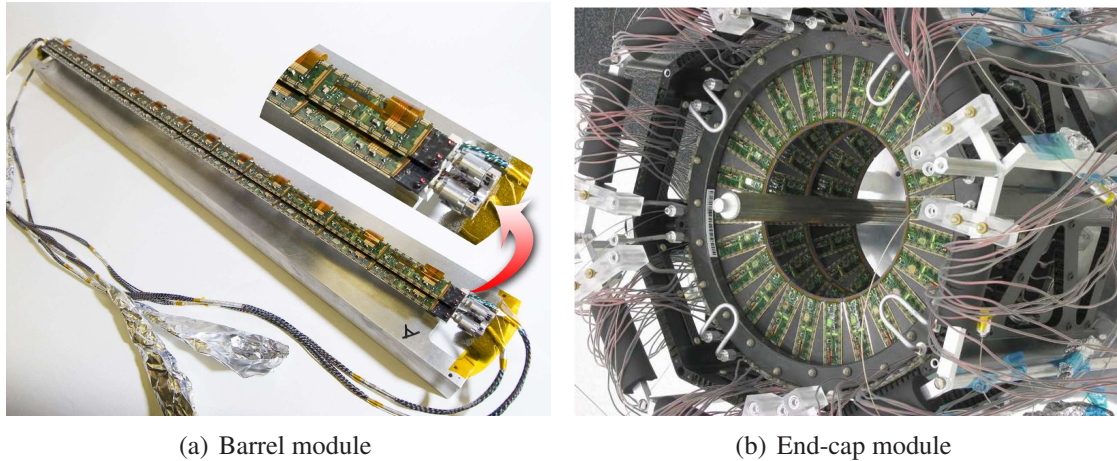
Figure 2.14: Photograph of the pixel detector. (a) and (b) are the barrel module and the end-cap module, respectively.

Semiconductor Tracker

The Semiconductor Tracker (SCT) is the silicon strip detector. Figure 2.15 show the SCT barrel module and the end-cap module. SCT sensors are operated at $\approx$150 V bias voltage. The sensor thickness is $285 \pm 15\ \mu$m. Strip pitch of sensor for the barrel is $80\ \mu$m while that for the end-cap varies from 56.9 to 90.4 μm. SCT module is composed of four sensors. There are two sensors each on the top and bottom side. Two sensor layers of a SCT module are rotated with their hybrid assemblies by ±20 mrad around the geometrical center of the module. The identification of a particle position is enabled by two sensor layers of a SCT module.

Table 2.5 is the summary of the parameters of SCT barrel modules. SCT for the barrel consists of four coaxial cylindrical layers, which are called ID layers 3$\approx$6. The SCT module is arranged on cylindrical layers tilting about 11 degrees. The parameters of the end-cap modules are also summarized in Table 2.6. SCTs for the end-cap consists of each nine disks. There are 2112 barrel module and 1976 end-cap module.

Nominal resolution is $\approx 17\mu$m in lateral plane (r-ϕ) and $\approx 580\mu$m in longitudinal (z or r).

Table 2.5: Parameters of SCT barrel cylinder layer and the numbers of modules per layer.

ID layers	r(mm)	Full length (mm)	Module tilt angle (degrees)	Number of modules
3	299	1498	11.00	384
4	371	1498	11.00	480
5	443	1498	11.25	576
6	514	1498	11.25	672
Total				2112

Transition Radiation Tracker

Transition Radiation Tracker (TRT) [38, 39, 40] consists of many proportional drift tubes. In addition, TRT can perform particle identification by using Transition Radiation (TR). Figure 2.16 (a) and (b) show the photographs of the TRT detector.

(a) Barrel module
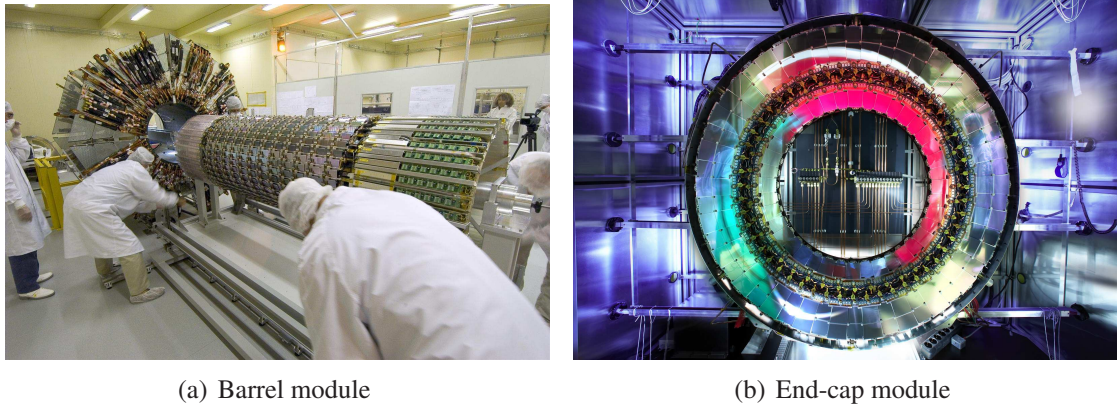
(b) End-cap module

Figure 2.15: Photographs of the SCT. (a) and (b) are the barrel module and the end-cap module, respectively.

Table 2.6: Nominal |z| positions of SCT end-cap disk and the number of SCT modules per disk.

Disk	1	2	3	4	5	6	7	8	9
|z|(mm)	853.8	934.0	1091.5	1299.9	1399.7	1771.4	2115.2	2505.0	2720.2
Outer	52								
Middle	40								None
Inner	None	40							None

(a) Barrel detector
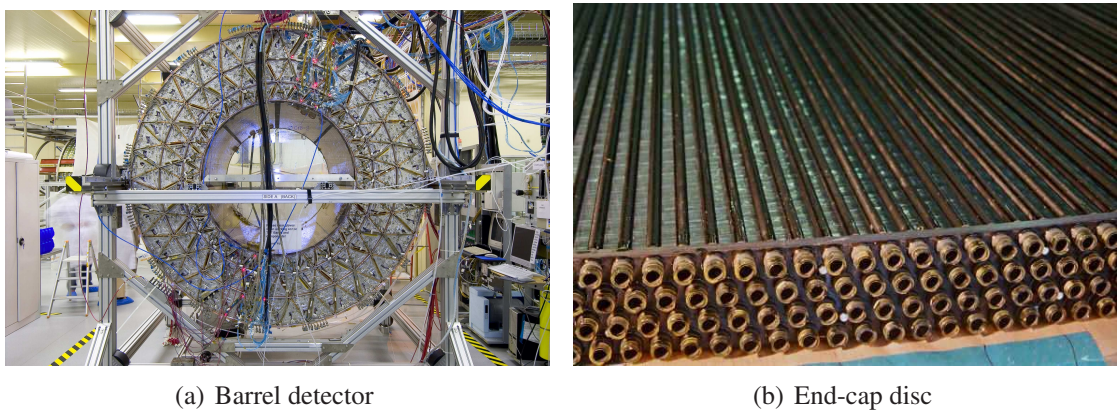
(b) End-cap disc

Figure 2.16: Photographs of the TRT. (a) is the barrel detector of the TRT. (b) shows a end-cap disc of the TRT.

Transition Radiation [41, 42, 43, 44] is a phenomenon that a relativistic particle emits photons when it passes through a boundary of materials whose dielectric constants are different. When a relativistic particle pass through the boundary of vacuum and the medium with a plasma frequency ω_p, it emits the energy W,

$$W_\text{TR} = \frac{1}{3}\alpha\omega_\text{p}\gamma, \tag{2.7}$$

where α is the fine structure constant and γ is the Lorentz factor of the particle. The plasma frequency ω_p is defined as,

$$\omega_\text{p} = \sqrt{\frac{N_\text{e}e^2}{\epsilon_0 m_e}}, \tag{2.8}$$

where, N_e, ϵ_0 and m_e are the electron density of the medium, the dielectric constant and the electron mass, respectively. W_TR is proportional to the Lorentz factor of a charged particle. Transition radiation is made use of the identification of electron which has a large γ. Transition radiation is extremely forward peaked within an angle $\theta_0 \sim 1/\gamma$.

The diameter of a drift tube is 4 mm. Anode wire is tungsten of 30 μm diameter which is gold-plated of about 0.5 μm thickness. Cathode is a tube of approximately 60 μm thickness which is made from carbon, aluminum and Kapton. The straw cathodes is operated at a high voltage of 1530 V with the gas mixture of Xe : CO_2 : O_2 = 70 : 27 : 3. A gas gain is 2.5×10^4. Polypropylene is used for the radiator of TRT. Figure 2.17 shows a layout of a barrel module. In barrel region, the radiator consists of the sheet of 3mm thickness which is made from radiator fiber of approximately 19 μm diameter. The density of the sheet is about 0.06 g/cm^3. These sheets are made holes in accordance with the geometry of TRT drift tubes and drift tubes penetrates these sheets. On the other hand, the radiator in the end-cap region is made by piling up foils made by polypropylene of 17 μm thickness.
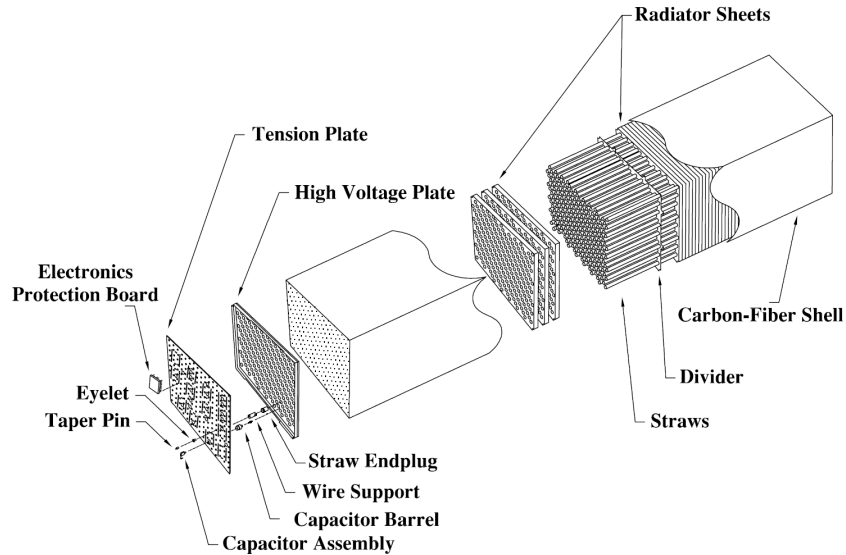
Figure 2.17: Layout of a barrel module.

Table 2.7 shows the main parameters of the TRT detector. In the barrel region, drift tubes are arranged along with z-axis. 1441mm drift tube is divided at its center in order to reduce

an occupancy. Figure 2.18 shows the cross-section of the TRT barrel detector. There are three types of modules which are called Type-1, Type-2 and Type-3. They are consists of 19, 24, 30 drift tube layers, respectively. Moreover, they are divided into 32 modules in ϕ-direction. The innermost nine layers are not active in $|z| < 400$ mm of the Type-1 module in order to reduce an occupancy.

In this analysis, Type-1, Type-2 and Type-3 are referred as *inner module*, *middle module* and *outer module*, respectively.
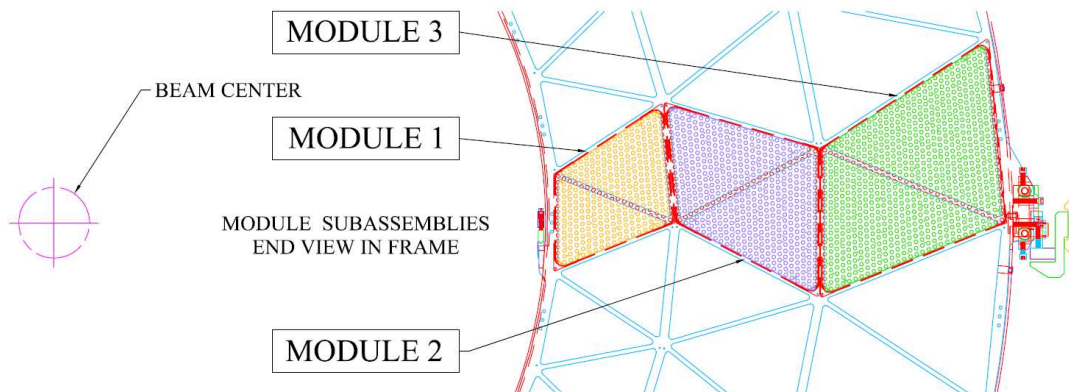
Figure 2.18: The cross-section of the barrel detector.

TRT in the end-cap region consists of disks in which drift tubes are arranged along with r-direction. There are two types for the end-cap detector. They are called Type-A and Type-B. They differ in the z spacing of these plates. In both modules each of these layers contains 768 straws of approximately 37 cm length. Both Type-A and Type-B module consists of eight disks layers.

Table 2.7: Parameters of TRT detector. The innermost nine layers of Type-1 is inactive in the region $|z| < 400$ mm.

	$|z|_{min}$ (mm)	$|z|_{max}$ (mm)	r_{min} (mm)	r_{max} (mm)	Number of modules	Number of layers	straws per module
Barrel	0	780	554	1082	96	73	52544
Type-1(inner)	400	712.1	563	624	32	9	329
Type-1(outer)	7.5	712.1	625	694		10	
Type-2	7.5	712.1	697	860	32	24	520
Type-3	7.5	712.1	863	1066	32	30	793
End-cap	827	2744	615	1106	20	160	122880
Type-A	848	1705	644	1004	12	8	6144
Type-B	1740	2710	644	1004	8	8	6144

Figure 2.19 (a) and (b) show the pulse height of the drift tubes for 20 GeVpions and electrons, respectively. There is a bump around 7 keVfor electrons. It corresponds to the X-ray due to the transition radiation. There are two threshold in TRT for particle identification. The first is for discriminating a energy loss of a particle ionization. The value of the threshold is
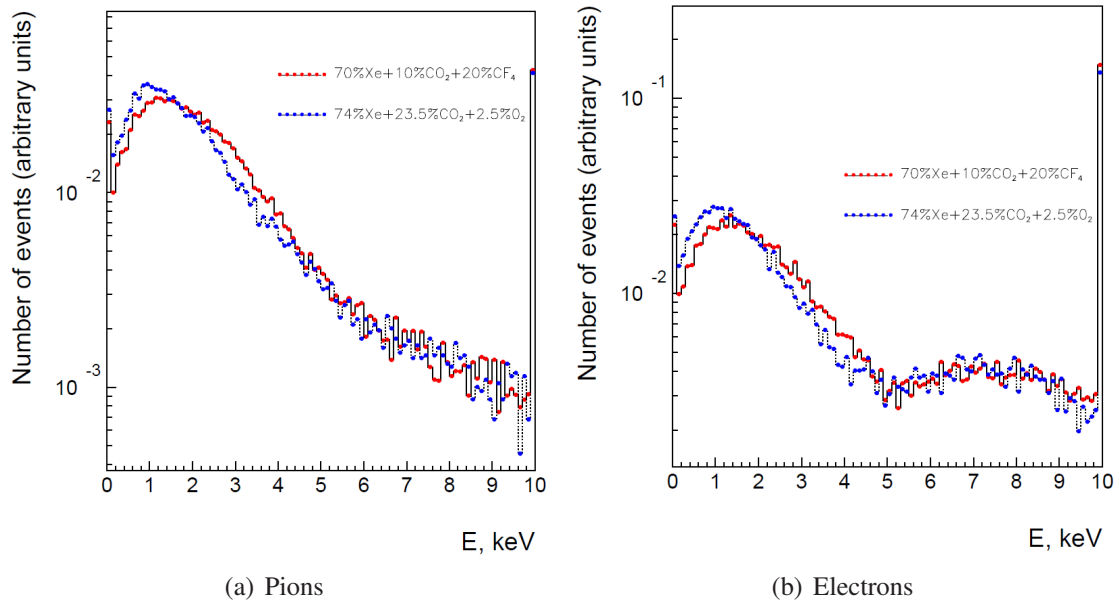
(a) Pions

(b) Electrons

Figure 2.19: The pulse height of the TRT drift tube. (a) shows the pulse height of the 20 GeVpions while (b) shows that of the 20 GeVelectrons.

about 0.2 keV. The second is for identifying electrons which emits TR photons. The value of the threshold is set at about 6 keV.

The studies for the TRT performance using cosmic data is mentioned in Chapter 3.

2.2.4 Calorimetry

Figure 2.20 shows the cutaway view of the calorimeter system of the ATLAS detector. Calorimeters are surrounding the Inner Detector and these system covers the range $|\eta| < 4.9$. Calorimeter system of the ATLAS has three calorimeters, that is, electromagnetic (EM) calorimeter, hadronic calorimeter and forward calorimeter.

Electromagnetic Calorimeter

The electromagnetic(EM) calorimeter are divided into three parts, a barrel part ($|\eta| < 1.475$) and two end-cap parts ($1.375 < |\eta| < 3.2$). The total thickness of the EM calorimeter is more than 22 radiation length (X_0) in the barrel regions and more than $24X_0$ in the end-cap region.

The geometry of the electromagnetic calorimeter for absorber and electrode is a particular geometry. The electromagnetic calorimeter has an accordion geometry for both the barrel and end-cap electromagnetic calorimeter as shown in Figure 2.21. This geometry enables to achieve full coverage in ϕ direction. In the barrel, the accordion waves are axial and run in ϕ-direction, on the other hand, in the end-cap the accordion waves are parallel to the radial direction and run axially. The barrel electromagnetic calorimeter separates to two half-barrels.

The main parameters of EM calorimeter is summarized in the Table 2.8. One half-barrel covers a region $z > 0, 0 < \eta < 1.475$ and the other half-barrel covers a region $z < 0, -1.475 < \eta < 0$. The length of a half-barrel is 3.2m and the inner and outer diameters are 2.8m and 4m,
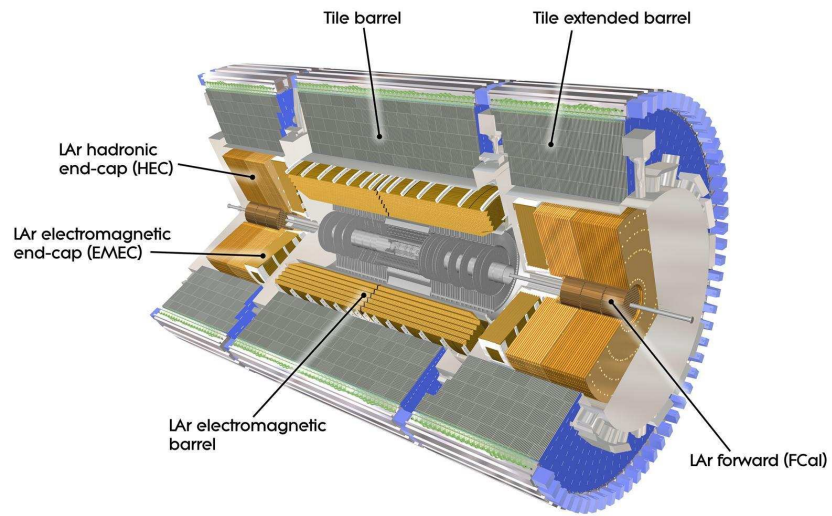
Figure 2.20: The overview of calorimeter.

Figure 2.21: A cross section of LAr electromagnetic calorimeter.
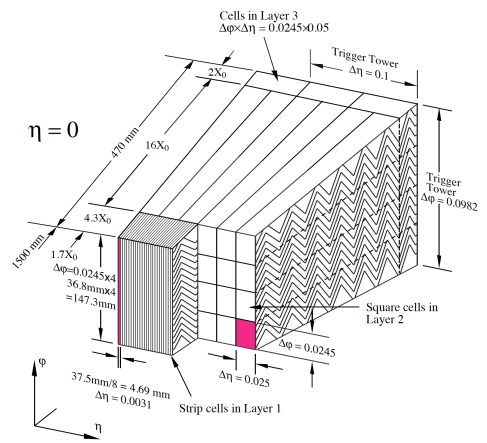
Figure 2.22: The geometry of LAr electromagnetic calorimeter at η=0. The accordion geometry is chosen for the electromagnetic calorimeter of ATLAS.

Table 2.8: The main parameters of EM calorimeter of the ATLAS.

	Barrel		End-cap	
	η coverage			
Presampler	$\|\eta\| < 1.52$		$1.5 < \|\eta\| < 1.8$	
Calorimeter 1st layer	$\|\eta\| < 1.475$		$1.375 < \|\eta\| < 3.2$	
Calorimeter 2nd layer	$\|\eta\| < 1.475$		$1.375 < \|\eta\| < 3.2$	
Calorimeter 3rd layer	$\|\eta\| < 1.35$		$1.5 < \|\eta\| < 2.5$	
	Granularity $\Delta\eta \times \Delta\phi$ versus η			
Presampler	0.025×0.1	$\|\eta\| < 1.52$	0.025×0.1	$1.5 < \|\eta\| < 1.8$
Calorimeter 1st layer	0.025/8×0.1	$\|\eta\| < 1.40$	0.050×0.1	$1.375 < \|\eta\| < 1.425$
	0.025×0.025	$1.40 < \|\eta\| < 1.475$	0.025×0.1	$1.425 < \|\eta\| < 1.5$
			0.025/8×0.1	$1.5 < \|\eta\| < 1.8$
			0.025/6×0.1	$1.8 < \|\eta\| < 2.0$
			0.025/4×0.1	$2.0 < \|\eta\| < 2.4$
			0.025 ×0.1	$2.4 < \|\eta\| < 2.5$
			0.1 ×0.1	$2.5 < \|\eta\| < 3.2$
Calorimeter 2nd layer	0.025×0.025	$\|\eta\| < 1.40$	0.050×0.025	$1.375 < \|\eta\| < 1.425$
	0.075×0.025	$1.40 < \|\eta\| < 1.475$	0.025×0.025	$1.425 < \|\eta\| < 2.5$
			0.1×0.1	$2.5 < \|\eta\| < 3.2$
Calorimeter 3rd layer	0.050×0.025	$\|\eta\| < 1.35$	0.050×0.025	$1.5 < \|\eta\| < 2.5$

respectively. The accordion-shape absorber are made of lead plates. A half-barrel consists of 1024 absorbers and readout electrodes. The electrode is placed in the middle of gap with the honeycomb spacers. Each half-barrel is divided into 16 modules for ϕ and covers a $\Delta\phi = 22.5°$. The total-thickness is of a module is at least $22X_0$. For $0 < |\eta| < 0.8$ the total thickness is from $22X_0$ to $33X_0$ and for $0.8 < |\eta| < 1.3$ from $24X_0$ to $33X_0$. A module has three layers in depth (front, middle and back) as shown in Figure 2.22.

Presampler is s separated thin liquid-argon layer. It is 11m in depth. It provides shower sampling in front of the electromagnetic calorimeter. This is made of 64 azimuthal sectors (32sectors per half-barrel). Each sector is 3.1m long and provides a covering $\Delta\eta \times \Delta\phi$ of 1.52×0.2.

The EM end-cap calorimeters consist of two wheels. Each wheel is 63 cm thick and the inner and outer radii are 330 m and 2098 mm. It covers the region $1.375 < |\eta| < 3.2$. Each end-cap is made of two co-axial wheels. Furthermore, this end-cap is divided into eight wedge-shaped modules. Each end-cap in the outer wheel has 768 absorbers with the electrodes interleaved and each end-cap in the inner wheel has 256 absorbers. The total thickness is greater than $24 X_0$ except for the region $|\eta| < 1.475$. The total thickness is from $24 X_0$ to $38 X_0$ for $1.475 < |\eta| < 2.5$ and from $26X_0$ to $36X_0$ for $2.5 < |eta| < 3.8$. Each end-cap presampler consists of 32 identical sectors. The granularity of the presampler is $\Delta\eta \times \Delta\phi = 0.025 \times 0.1$. This presampler is made of two, 2mm thick, active liquid-argon layers.

Hadronic Calorimeter

Hadronic calorimeter has two calorimeter systems; tile calorimeter and LAr hadronic end-cap calorimeter. Hadronic calorimeter system is placed at the outer region of the electromagnetic calorimeter in order to measure the energy of hadrons.

The tile calorimeter consists of three parts; one central barrel and two extended barrels. The tile calorimeter covers the range $0 < |\eta| < 1.7$. For the range $1.7 < |\eta|$, the LAr hadronic end-cap calorimeter is arranged.

Tile Calorimeter   The tile calorimeter is placed outside the EM calorimeter. Figure 2.24 shows the tile calorimeter. The tile barrel calorimeter covers the range $|\eta| < 0.8$ and the tile
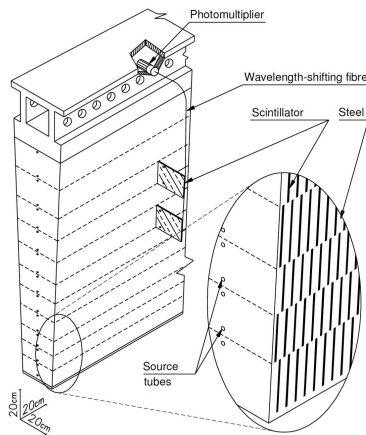
Figure 2.23: Schematic showing of the tile calorimeter.

Figure 2.24: Tile calorimeter of the ATLAS.

extended barrel covers the range $0.8 < |\eta| < 1.7$. The tile calorimeter consists of steel and scintillating tile. Steel is used as the absorber and scintillating tile is used as the active material.

The inner radius is 2.28m and the outer radius is 4.25m. This calorimeter is divided into three parts in layers in depth. These layers of tile barrel are roughly 1.5λ, 4.1λ and 1.8λ thick and these of tile extended barrel are roughly 1.5λ, 2.6λ and 3.3λ thick. The total thickness of tile calorimeter at $\eta = 0$ is 9.7λ.

The geometry of the assembled module is sketched in the Figure 2.23. The tile scintillator is oriented radially and normal to the beam axis. This scintillator is combined with a wavelength-shifting tube on the edge of tile. The scintillating tile is read out from two sides with wavelength shifting fiber and into two photomultiplier tubes.

This calorimeter is a sampling calorimeter.

LAr Hadronic End-cap Calorimeter   The hadronic end-cap calorimeter is shown in Figure 2.25. This calorimeter consists of two parts of detector. It uses copper as the absorber and liquid argon as the active material. The hadronic end-cap calorimeter (HEC) is a copper and LAr sampling calorimeter. It covers the range $1.5 < |\eta| < 3.2$.

51

Table 2.9: The main parameters of scintillator tile calorimeter of the ATLAS.

	Barrel	Extended barrel
η coverage	$|\eta| < 1.0$	$0.8 < |\eta| < 1.7$
Number of layers	3	3
Granularity $\Delta\eta \times \Delta\phi$	0.1×0.1	0.1×0.1
Last layer	0.2×0.1	0.2×0.1

The HEC consists of two wheels in each end-cap: a front wheel (HEC1) and a rear wheel (HEC2). The wheels are cylindrical with an outer radius of 2030 mm. Each of four HEC wheels consists of 32 identical modules. Figure 2.26 shows the schematic view of a module of the LAr hadronic end-cap calorimeter. The modules of the front wheels are made of 24 copper plates of 25 mm thick. In the rear wheels, module consists of 16 copper plates of 50 mm thick. The gap between the the plates is 8.5 mm thickness. The size of the readout cells is $\Delta\eta \times \Delta\phi = 0.1 \times 0.1$

Figure 2.25: Photograph of the assembled LAr hadronic end-cap calorimeter.
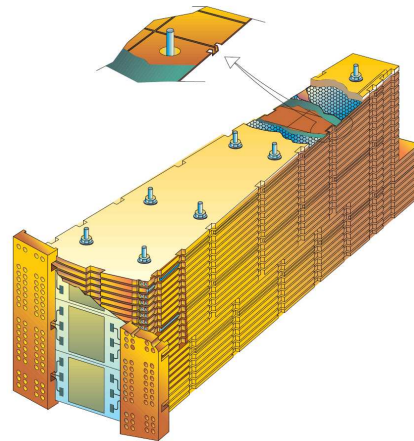
Figure 2.26: Schematic view of the LAr hadronic end-cap calorimeter. A cutaway shows the readout and active pad.

for $|\eta| < 2.5$ and $\Delta\eta \times \Delta\phi = 0.2 \times 0.2$ for $|\eta| \geq 2.5$. The main parameters of HEC is summarized in the Table 2.10.

Table 2.10: The main parameters of LAr hadronic calorimeter of the ATLAS.

	LAr hadronic end-cap calorimeter	
η coverage	$1.5 < |\eta| < 3.2$	
Number of layers	4	
Granularity $\Delta\eta \times \Delta\phi$	0.1×0.1	$1.5 < |\eta| < 2.5$
	0.2×0.2	$2.5 < |\eta| < 3.2$

Forward Calorimeter

The forward calorimeter (FCal) covers over $3.1 < |\eta| < 4.9$. The forward calorimeter consists of three modules. One is the electromagnetic module (FCal1) and the other modules are the hadronic modules (FCal2 and FCal3). Figure 2.27 shows the schematic view of the forward calorimeter.

It has a design with very small liquid-argon gaps, which have been obtained by employing an electrode structure of small-diameter rods. These rods are centered in tubes which are oriented parallel to the beam. The liquid-argon gaps are smaller than 2 mm. The FCal1 layer consists of copper plates stacked one behind the other. An electrode consists of a co-axial copper rod and the copper tube separated by a precision, radiation-hard plastic fiber wound around the rod. Figure 2.28 shows the arrangement of electrodes and the effective Moliére radius for the modules.

The hadronic modules FCal2 and FCal3 is employing tungsten as a absorption material. The modules consists of two copper end-plates, each 2.35 cm thick, which are spanned by electrode structures. The main parameter is shown in the Table 2.11.
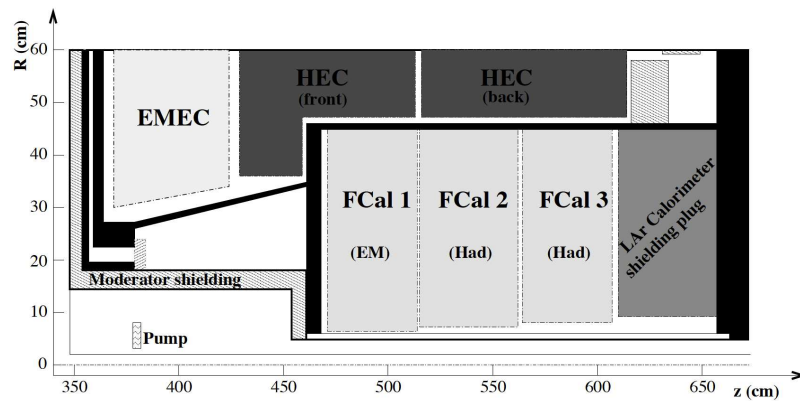
Figure 2.27: Schematic view of the LAr hadronic end-cap calorimeter. A cutaway shows the readout and active pad.
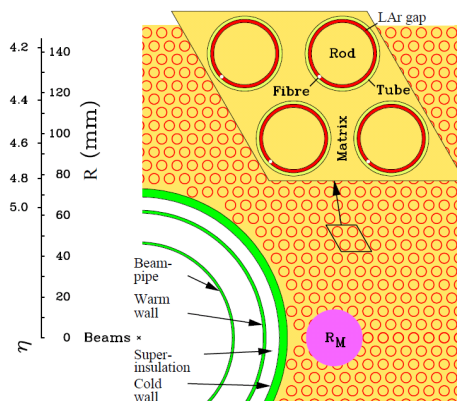
Figure 2.28: The structure of the electrode of FCal1. The Moliére radius which is represented R_M is shown with magenta disk.

Table 2.11: The main parameters of forward calorimeter of the ATLAS.

		LAr forward calorimeter	
η coverage		$3.1 < |\eta| < 4.9$	
Number of layers		3	
Granularity $\Delta x(cm) \times \Delta y(cm)$	FCal1	0.1×0.1	$3.15 < |\eta| < 4.30$
		~ four times finer	$3.10 < |\eta| < 3.15,$ $4.30 < |\eta| < 4.83$
	FCal2	3.3×4.2	$3.24 < |\eta| < 4.50$
		~ four times finer	$3.20 < |\eta| < 3.24,$ $4.50 < |\eta| < 4.81$
	FCal3	5.4×4.7	$3.32 < |\eta| < 4.60$
		~ four times finer	$3.29 < |\eta| < 3.32,$ $4.60 < |\eta| < 4.75$

2.2.5 Muon Spectrometer

Muon spectrometer is the outermost part of the ATLAS detector. Muon spectrometer is designed to detect the charged particle which penetrates calorimeter of the ATLAS, especially muon. Figure 2.29 shows the whole Muon Spectrometer of ATLAS. It consists of four parts
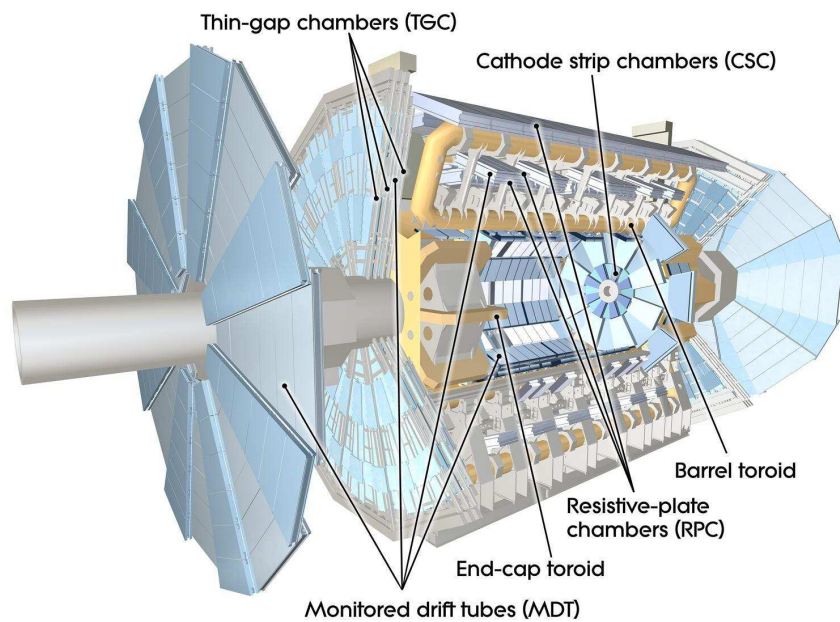
Figure 2.29: The overview of Muon Spectrometer of ATLAS.

of sub-detector which are Resistive Plate Chamber(RPC), Monitored Drift Tube(MDT), Thin Gap Chamber(TGC) and Cathode Strip Chamber(CSC). It plays a roll to trigger on the outgoing charged particle and to give precise position and momentum of that. This system covers the pseudorapidity range $|\eta| < 2.7$ to measure the momentum of particle and covers the range, $|\eta| < 2.4$ to measure the position Tracking chambers are located between and on the eight-coil

superconducting toroid magnet for barrel and in front of and behind the end-cap toroid magnet for end-cap.

For end-cap region, there are three types of wheels. The inner wheel is refereed as *the small wheel*. TGC and CSC are mounted on the small wheel. The middle wheel is called *the big wheel* or *EM-wheel* . TGC and MDT are mounted on it. The outer wheel is refereed as *EO*. Only MDT is mounted on EO.
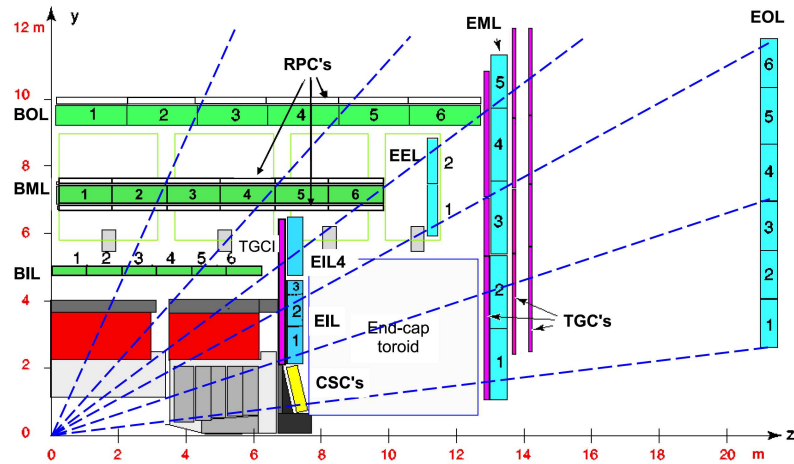
Figure 2.30: The cross section of Muon Spectrometer on r-z plane.

Table 2.12: Parameters of the four sub-detector of muon spectrometer.

Detector	Main Function	Resolution (RMS) in			Hits per track		Numbers of	
		z or r	ϕ	t	barrel	end-cap	chambers	channels
RPC	Trigger	10mm (z)	10mm	1.5ns	6	—	544	359000
MDT	Tracking	35μm (z)	—	—	20	20	1088	339000
TGC	Trigger	2-6mm (r)	3-7mm	4ns	—	9	3588	318000
CSC	Tracking	40μm (r)	5mm	7ns	—	4	32	30700

Resistive Plate Chamber

Resistive Plate Chamber (RPC) is the muon trigger system in the barrel. Figure 2.31 shows a photograph of RPC.

RPC has good space resolution and time resolution.

RPC is a no wire chamber and a gaseous parallel electrode-plate detector. There are two resistive plates which are kept 2mm apart with insulating spacer. The electric field between the plates is about 4.9 kV/mm. Due to the electric field, the avalanche occurs along the track of particle towards anode.

There is gas in the gap of plates. The gas mixture is $C_2H_2F_4/Iso - C_4H_{10}/SF_6(94.7/5/0.3)$.

A chamber of RPC consists of two rectangle detector which are called units. Each unit consists of two detector layer and these are called gas volume. Gas volume has two type of strips and signals are read out from these strips. The two types of strips are the ϕ-strips and the

η-strips. As these name suggest, The ϕ-strips and the η-strips measure the ϕ-coordinate and the η-coordinate, respectively.

Figure 2.31: Photograph of the RPC.
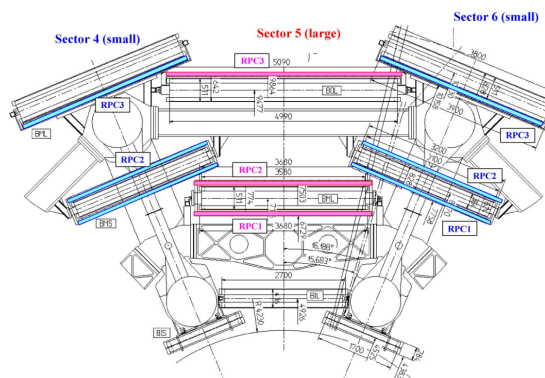
Figure 2.32: Cut-away view of the barrel muon system. RPC is marked with color.

Monitored Drift Tube

Monitored Drift Tube (MDT) consists of many layers of drift tubes and serves as a muon tracker. MDT covers $|\eta| < 2.7$ except for the inner most layer. MDT is replaced for Cathode Strip Chamber in $2 < |\eta| < 2.7$.

A diameter of a drift tube constituting MDT is 29.970 mm. Tube is made from aluminum. Wall thickness is 0.4 mm. Wire diameter is 50 μm. Material of wire is gold-plated tungsten and rhenium. Gas mixture is $Ar/CO_2/H_2O(93/7/\leq1000pm)$. Gas pressure is 3 bar and gas gain is 2×10^4. Wire potential is 3080 V. Maximum drift time is about 700 ns and average resolution per tube is about 80 μm.

Chamber is rectangular for the barrel and is trapezoidal for the end-cap. The length of tube in the barrel chamber is identical while the length in the end-cap varies radially.MDT chambers consists of two collections of drift tubes. This collection is called multi-layer. Two multi-layers are separated by mechanical spacers.

Alignment of tubes is needed to maintain a good precision in order to achieve its inherent resolution. For that, drift tubes are mounted on the support frame made from aluminum. Additionally, internal chamber alignment is also monitored with four alignment rays. Two alignment rays are parallel to tubes. The other two rays are diagonal. By using this, deformation of a few μm can be measured. This system works in production, installation and operation of ATLAS.

Thin Gap Chamber

Thin Gap Chamber (TGC) is a multi wire proportional chamber. The photograph of TGC mounted on the big wheel of the muon spectrometer is shown in Figure 2.34. TGC serves two functionality in the end-cap muon detector. One is working as a detector for muon trigger and the other one is giving the information of ϕ-direction in order to complement the information of muon position obtained from MDT.
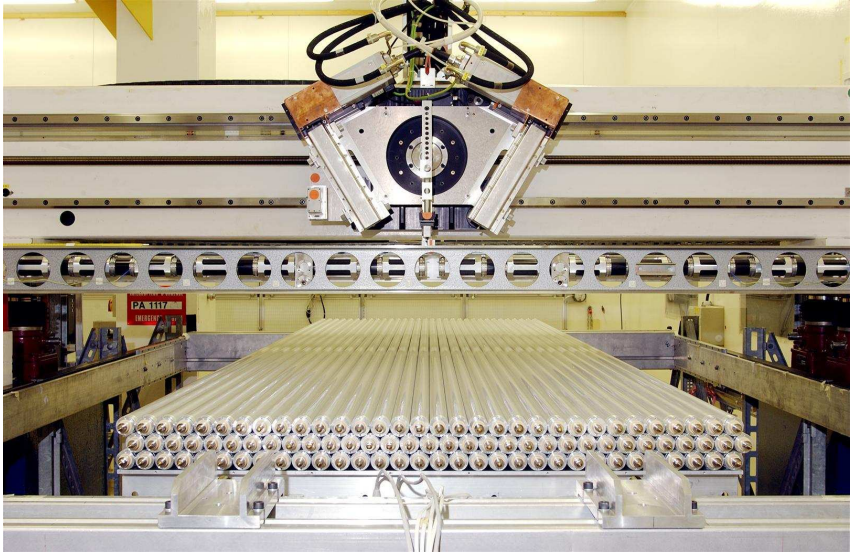
Figure 2.33: The photograph of drift tubes of MDT.
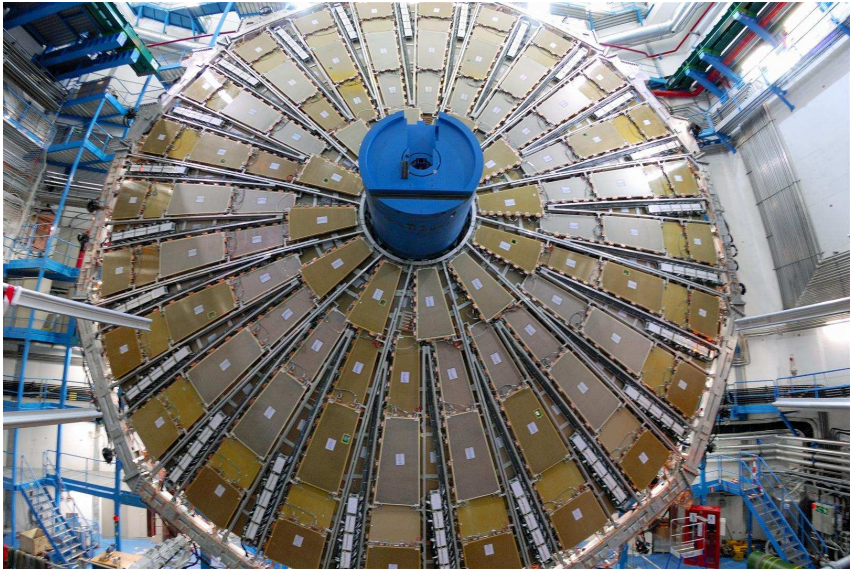
Figure 2.34: The photograph of the big wheels of the muon spectrometer.

The character of TGC structure is that the distance from wire to cathode is smaller than that from wire to wire. The distance from wire to cathode is 1.4 mm while the distance from wire to wire is 1.8 mm.

The gas mixture is CO_2/n-C_5H_{12} (n-pentane). CO_2 is 55% and n-pentane is 45%. A gas gain is about 3×10^5.

TGC has good time resolution for most of muons because electric field around wire is high and the distance from wire to wire is small. However, for muons incidenting normally to detectors and passing halfway between wires, the drift time becomes longer due to vanishing a drift fields.

TGC is mounted on two concentric discs. Outer disc (end-cap one, the big wheel) covers $1.05 \le |\eta| \le 2.4$. TGC consists of seven layers in the big wheels, that is, one triplet and two doublets. On the other hand, inner disc (forward one, the small wheel) covers $1.92 \le |\eta| \le 2.4$. On the small wheel, there are two TGC layers.

The structure of TGC detector is shown in Figure 2.35. The TGC consists of wire plane, cathode plane, strip plane, shields and honeycomb support structures. The cathode plane is 1.6mm thick plate. It is coated with graphite and facing to wire and copper cladding is outside.

The gas volume including wire plane and two cathode is called chamber. A collection of Two (three) chamber for doublet (triplet) is called a unit. TGC on the Big Wheel is divided into twelve sectors for ϕ-direction. Furthermore, a sector in the outer ring is separated into four module. A sector in the inner ring is separated into two module. They are referred as EI (end-cap region) and FI (forward region).
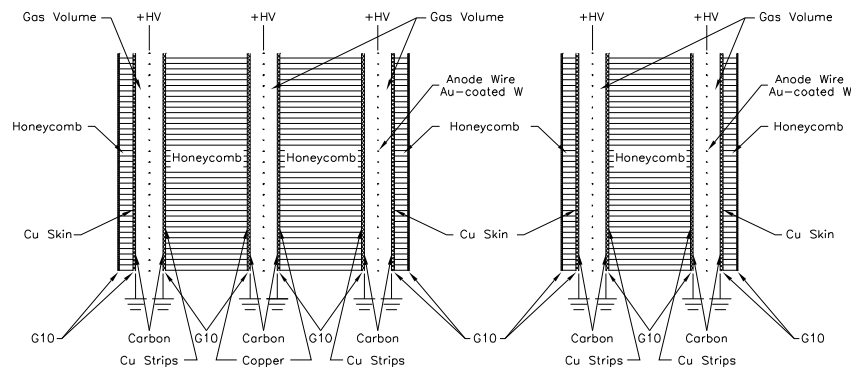
Figure 2.35: The structure of TGC.

Cathode Strip Chamber

Cathode Strip Camber(CSC) is multi wire proportional chamber.

The limitation of the safe operation for MDT is 150 Hz/cm^2. MDT is replaced for CSC in $|\eta| > 2$ for this reason. The distance from interaction point to CSC is about 7 m. Inner radius is 881 mm and outer radius is 2081 mm. This corresponds to the coverage of rapidity, $2 < |\eta| < 2.7$. CSC has high spacial and time resolution. CSC has also high-rate capability which is up to 1000 Hz/cm^2.

CSC system is divided into large and small chambers in ϕ-direction. CSC consists of two discs. One is made of eight large chambers while the other one is made of eight small chambers.

A chamber consists of four plane. Therefore, four dependent measurements in η and ϕ can be obtained.

Wires are along radial direction. Two cathodes are segmented to strips. Direction of one cathode strips is orthogonal to wires and direction of the other one is parallel to the wire. Operating voltage is 1900V. Anode wire diameter is 30 μm. Gas gain is 6×10^4. Gas mixture is Ar/CO$_2$(80/20). Total ionization for nominal track is 90 ion pairs. A distance from anode to wire is 2.5mm. Anode wire pitch is 2.5mm. The position of a track is determined by interpolating the induced charge of neighboring strips. Position resolution is about 60 μm/plane.
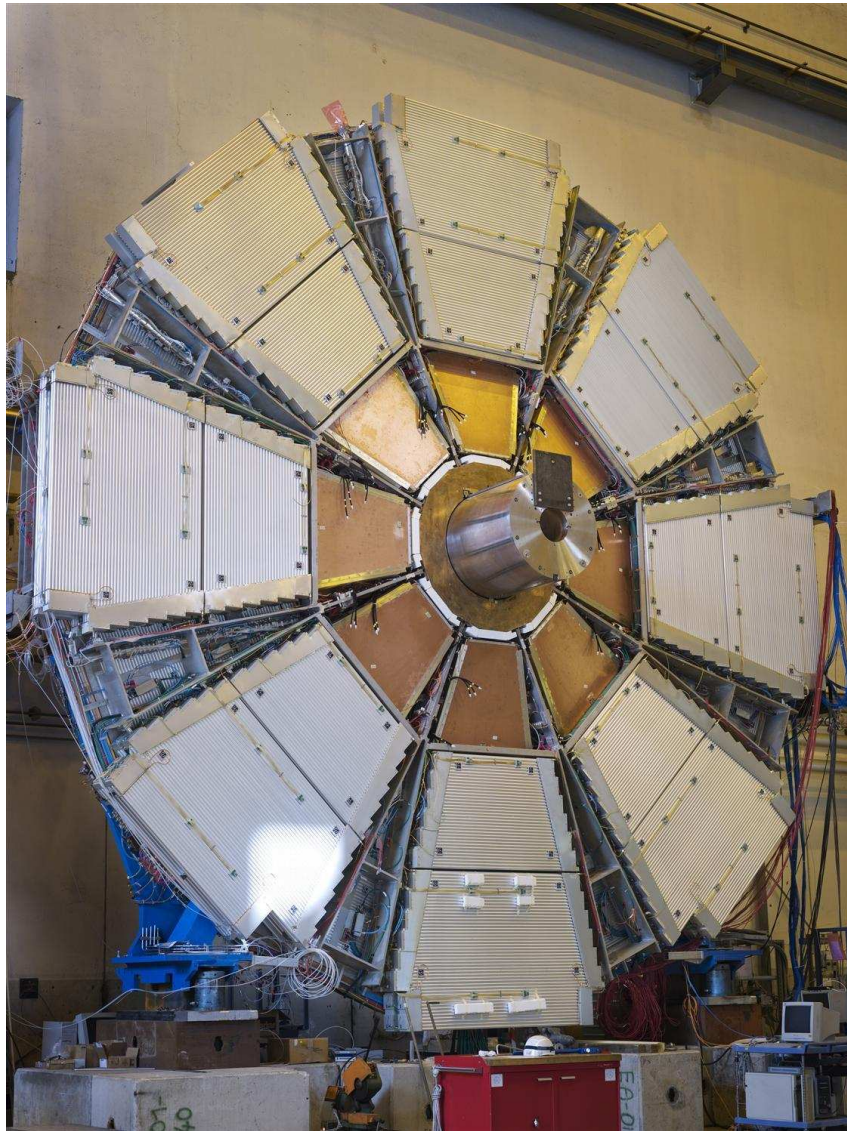
Figure 2.36: A small wheel of the muon spectrometer. The inner and outer detector mounted on the small wheel are the CSC and the MDT, respectively.

2.2.6   Forward Detector

Three sub-detectors are located in the very forward region in addition to the main ATLAS detector. These are LUCID, ZDC and ALFA. These detectors are located for providing good coverage.

LUCID (Luminosity measurement using Čerenkov Integrating Detector) is the main relative luminosity monitor. It is located at a distance of 17 m from the interaction point.

ZDC (Zero-Degree Calorimeter) is 140 m away from the interaction point. This location is the point where the LHC beam-pipe separates to two pipes. The main purpose of ZDC is for detecting forward neutron in heavy-ion collision.

ALFA (Absolute Luminosity For ATLAS) consists of scintillating-fiber trackers in Roman pots. The distance between ALFA and the interaction point is 240 m. ALFA is the absolute luminosity detector.

The LUCID detector

LUCID (Luminosity measurement using Čerenkov Integrating Detector) is used for online luminosity monitoring. This detector serves as a relative luminosity detector. LUCID measures inelastic pp scattering in forward region and monitors instantaneous luminosity and beam conditions.

Multiple pp interactions occur in bunch-crossing at LHC design luminosity. In order to measure luminosity, the number of interaction per bunch-crossing must be known. LUCID is based on that the number of interaction in bunch-crossing is proportional to the number of charged particle. LUCID is required for good-acceptance for minimum-bias, sufficient time resolution to measure individual bunch-crossing, tolerance for very-high radiation and ability to measure each charged particle from the interaction point. There are two LUCID detector for each end-cap. These are located at ±17 m from the interaction point. The radial distance is about 10 cm from beam-pipe and it corresponds to $|\eta| \approx 5.8$. LUCID consists of twenty aluminum tubes surrounding beam-pipe. These tubes are 1.5 m long. The diameter of the tube is 15 mm. These tubes are in gas vessel. C_4F_{10} gas is filled in the vessel with 1.2-1.4 bar.

Čerenkov light is emitted when charged particles traverse the tube. Čerencov light is detected with photomultiplier tubes. The signal amplitude from photomultiplier tubes is used for identification for the number of charged particles per tube.

Furthermore, for the studies for upgrade the detector after several years of LHC operation, a different readout scheme is used. A winstone cone, which is parabolic shape and designed to maximize incoming rays, is attached to the end of Čerenkov tube and the light is collected to a bundle of 37 fused silica fibers with 0.8 mm diameter. In this manner, four of twenty tube is readout with fibers.

The Zero-Degree Calorimeter

The main purpose of Zero-Degree Calorimeter(ZDC) is to measure the forward neutron in heavy-ion collision. It locates at ±140 m from the interaction point. There are four modules per arm; one module is the electromagnetic module and the other modules are the hadronic module. The electromagnetic module has 29 radiation length. The hadronic modules has 1.14 interaction length per module.

There are eleven tungsten plates in the electromagnetic module. These plates are perpendicular to beam. These tungsten plates are extended with steel plates of 290mm long. 95 quartz rods of 1.0 mm diameter penetrate the tungsten plates parallel to beam. These rods are bent upward and viewed by the multi-anode phototube's. Čerenkov light emitted from the shower of incident particles are measured. The position of the rod corresponds the position of the incident particle. The intensity of the light reflects the energy of the incident particle.

There are quartz strips between plates. These strips are viewed by photomultiplier tubes from above via air light-guide. These strips are actually rows of quartz rods. In order to distinguish from rods for position-measurement, they are called strips. The purpose of strips is for the improved measurement of the energy of the incidenting particle.

The structure of hadronic module is similar to that of electromagnetic module. But there are several differences. The electromagnetic module maps each position-measuring rods onto one pixel of the multi-anode phototube. On the other hand, the hadronic module maps a group of four rods onto the individual phototube. Furthermore, not all hadronic module have position-sensing rods. There are one module having position-sensing rods per arm.

The ALFA Detector

ALFA (Absolute Luminosity For ATLAS) is a detector for measuring the absolute luminosity. The absolute luminosity at hadron collider has been measured by using elastic scattering at small angles. ALFA is also based on this method. Optical theorem says that the total cross-section is obtained from the amplitude of inelastic scattering in the forward region. The absolute luminosity can be obtained by using this theorem.

A detector must be placed far from the interaction point and as nearest to beam as possible for that. The Roman pots techniques are used in the past experiments. Also ATLAS experiment adopt this method. Roman pots are located ±240 m away from the interaction point. There are two Roman pots on each side separated by 4 m. There is a scintillating-fiber tracker in the Roman pot.

2.2.7　Trigger and Data Acquisition

Overview of Trigger System

The ATLAS trigger consists of three level triggers; Level-1 (L1), Level-2 (L2) and Event Filter (EF).Level-2 trigger and event filter is also called the high level trigger (HLT). Level-1 trigger is implemented in the detector and works with the hard-ware. The high level trigger is using computer and network hardware.

Event rate is extremely high at the bunch-crossing with designed parameter of LHC. In order to trigger event to see, multi-stage triggers are used. Figure 2.37 show the diagram of data acquisition of the ATLAS.

The L1 trigger is required to make a decision in less than 2.2 μs and to lessen the trigger rate to about 75 kHz. Then, the L2 trigger uses the L1 seed, which is defined as Region of Interest (RoI) defined by the L1 trigger. The L2 trigger is required to reduce the trigger rate to 3.5 kHz. Finally, the information is passed to EF trigger. The EF uses the whole detector information and is required to reduce the rate up to 200 Hz.
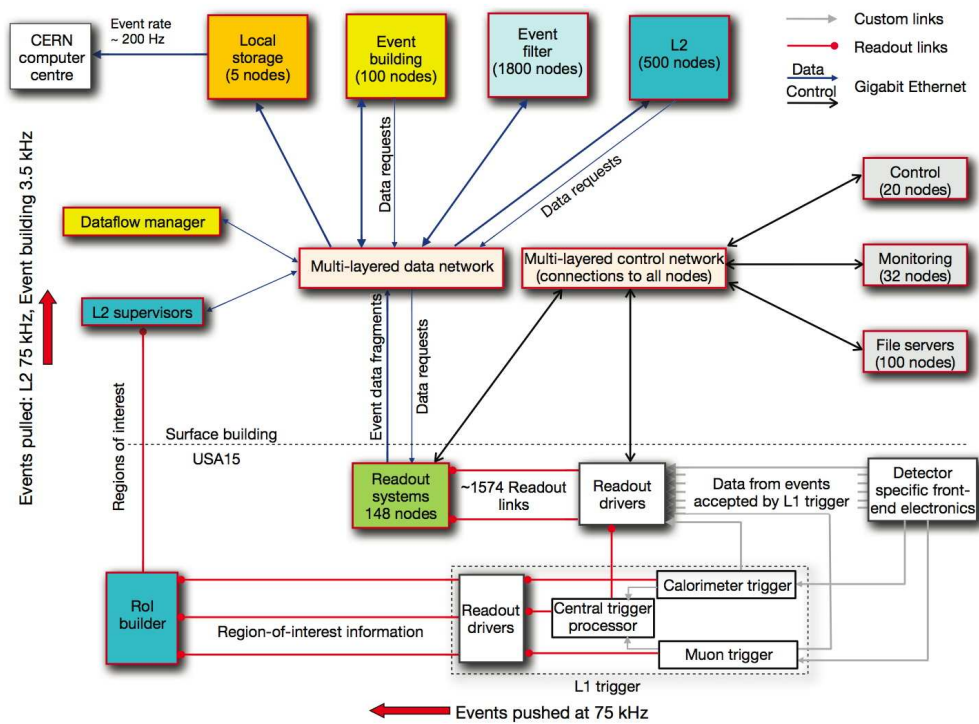
Figure 2.37: The diagram of data acquisition system.

Level-1 Trigger

The L1 trigger looks for high transverse-momentum (p_T) muons, photons, electrons, jets, taus decaying into hadrons, large missing transverse energy (E_T^{miss}) and large total transverse energy. The diagram of L1 trigger scheme is shown in the Figure 2.38. L1 trigger selects events initially and this is performed by using the information from the detectors. For the trigger decision, calorimeter and muon chamber are used. All L1 trigger is made a decision at Central Trigger Processor(CTP). When a event is passed in L1 trigger, the information for the positions of trigger objects are sent to L2 trigger as RoI. An important role of L1 is to identify a bunch-crossing of interest.
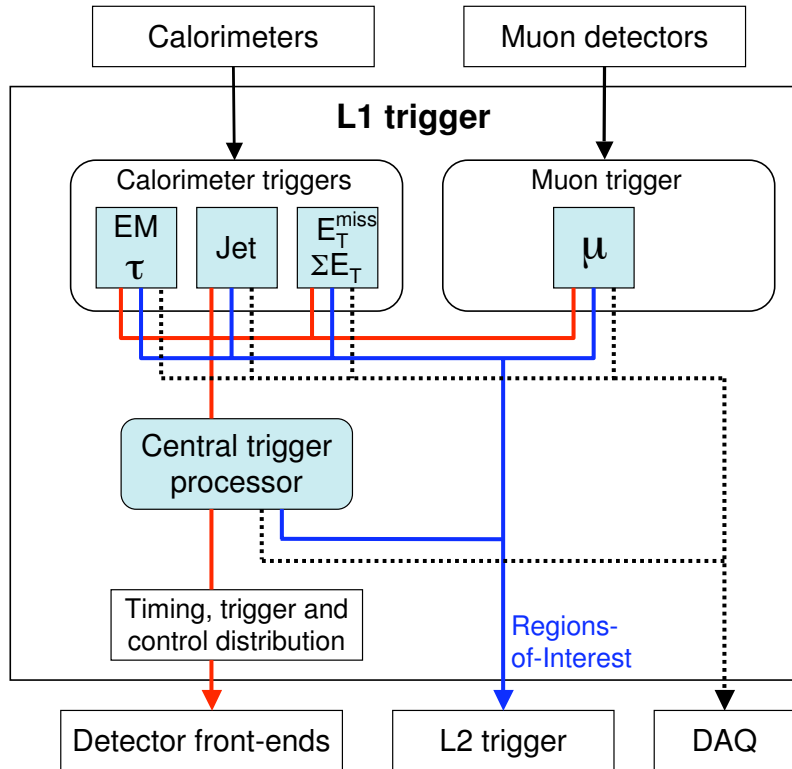
Figure 2.38: The diagram of L1 trigger flow.

The interval of bunch-crossing is very short and it makes challenging to make a L1 decision. For calorimeter triggers, the signals of calorimeter are long and over times for some bunch-crossing. For muon triggers, time of flight of muons exceeds the time for the interval of bunch-crossing due to the location of the muon spectrometer. Therefore, the L1 latency, which is the time between pp-collision and L1 trigger decision, needs to be short as possible. The L1 latency is designed to be less than 2.5μs.

The L1 calorimeter trigger The L1 calorimeter trigger is called L1Calo. L1Calo is based on the information from the all calorimeters. This trigger is used to identify high-E_T objects such as jets, photons, electrons, taus and large E_T^{miss} and large E_T events. Furthermore, the triggers on the events with large sum-E_T of jets is available.

The L1Calo uses the information of 7000 analogue trigger tower. The granularity of this is 0.1×0.1 in $\Delta\phi \times \Delta\eta$ in most region and larger in the other higher $|\eta|$ region. In order to make a L1 trigger decision, both electromagnetic calorimeter and hadron calorimeter are used. These information are sent to CTP within 1.5 μs after an event occurred. The total latency is about 2.1 μs.

The L1Calo system is located at off-detector. The Pre Processor digitizes analogue signal and associate to bunch-crossing of interest. The trigger algorithm uses the look-up table for calculation of calorimeter E_T. Data are sent to the Cluster Processor and the Jet/Energy-sum Processor in parallel. The Cluster Processor identifies electron, γ and τ by requiring certain E_T threshold and isolation criteria.The Jet/Energy-sum Processor uses jet trigger elements, whose granularity is 0.2×0.2 in $\Delta\phi\times\Delta\eta$ and identifies jets. It also calculates the sum of E_T and missing transverse energy. Once L1 Accept (L1A) decision is made, data are sent to the data acquisition system. These data, calculation and trigger results are also used for monitoring or verification of trigger. The information of Jets, τ, and EM cluster is sent to RoI builder.

The L1 muon trigger   The L1 muon trigger is performed with the information from muon chambers. RPC is used for muon in the barrel region, while TGC is used for end-cap region. The timing accuracy is required for muon detector to identify a bunch-crossing which has muons. The principle for finding muons is performed by requiring coincident hits in different trigger station in the road, that is,searching for tracks originating from the interaction point penetrates a detector.

RPC is used for the muon barrel trigger. RPC covers the range of $|\eta| < 1.05$. If there are hits in the second RPC doublet (the pivot plane), the trigger algorithm searches for the hits in the first RPC doublet by requiring that there are hits in the road made by drawing a line from the interaction point to the hit in the pivot plane. The center of the road is the hit in the pivot plane and the width depends on the transverse momentum of muon. The higher the p_T of muon is, the narrower the width of road become. A 3-out-of-4 coincidence hits are required for trigger decision. This suppresses the fake tracks which is made from noise hits. For high-p_T muons, RPC3 is also used with the trigger information of RPC1 and RPC2. The algorithm works as well as low-p_T muons and the center of the road is determined. After that, a 1-out-of-2 coincident hits in RPC3 is required in addition to trigger pattern for low-p_T muons. The latency is about 2.1 μs.

TGC is used for the muon end-cap trigger. The coverage is $1.05 < |\eta| < 2.4$ except for the innermost layer on the small wheel, which covers the range $1.05 < |\eta| < 1.92$. Each trigger chamber plane consists of a wheel of eight octets of chambers symmetric in ϕ. Each octant is divided radially into 'end-cap region' and 'forward region'. The algorithm works by extrapolating hits in the pivot plane to the interaction point. The road is made by a track of infinite momentum muon. Coincidence signals are generated separately in R and ϕ. A 3-out-of-4 coincidence hit is required for the two doublet planes on the big wheel for both wires and strips. A 2-out-of-3 coincidence hit is required for triplet wire plane and 1-out-of-2 coincidence hit is required for triplet strip plane. In order to make final decision R and ϕ coincidence signals are merged and the information of EI/FI chambers are also used. The latency is 2.1μs.

Level-2 Trigger

Events passed for L1 trigger is transferred to the Level-2 (L2) trigger. The RoI builder receive the RoI information from the different sources within the L1 trigger and merges them into the single data structure. It is at the boundary between the L1 and the L2 trigger systems and operated at the L1 trigger rate.

The principle component of the L2 trigger is the L2 processing farm. The L2 processing farm executes event selection. This system is designed to perform to execute event selection with an average throughput per farm node of about 200 Hz. The HLT starts from the RoIs delivered by the L1 trigger and applies trigger decisions. A list of physics signatures which is called *trigger chains*, implemented event reconstruction (*feature extraction*) and selection algorithms are used to build signature for all HLT steps. Feature extraction uses detector data of RoI in order to identify the features of events such as tracks, calorimeter cluster, and so on. Then, this feature is checked to meet the criteria e.g. shower shape, E_T threshold, et cetra. Whether the event is rejected or not is decided by the validity of signature considering pre-scale and pass-through factor. The full data set and RoI information are kept if the event fulfill the L2 trigger selection.

Event Filter

Event filter (EF) reconstructs and analyzes events of ATLAS unlike the L2 trigger. The EF has the processing farm. The processing farm is a collection of processing nodes which receive tasks and process events. The steering of the event selection is the same as the L2. For those events passing the selection criteria, a subset of the data generated during the event analysis is added to the event data structure. An integral part of the selection process is the classification of the events according to the ATLAS physics streams. Finally, the tags are append to events which fulfill the selection criteria of EF trigger. These tags enables to classify physics streams.

The main functionality of the EF output nodes, which is called *SFO's*, is to receive events which have passed the selection criteria of the EF. The SFO maintains a set of files into which the SFO records events at a peak event rate of up to 400 Hz. In the case of a prolonged failure in the transmission of data to the CERN's central data storage, there is sufficient local storage capacity to buffer all events locally for up to one day. The set of files maps to the ATLAS-defined data steams: electrons, muons, jets, photons, E_T^{miss}, τ and B-physics. Each event is recorded in one or more files according to the stream classification made by the EF processing task. In the addition to the streams mentioned above, a subset of the events is also written to the calibration and express stream. The calibration stream provides the minimum amount of information needed for detector calibration. The express stream is a subset of the events selected by the event filter and fulfill additional criteria for monitoring the quality of the data and the detector.

Chapter 3

Performance of TRT Detector

3.1   Performance of TRT with Cosmic Data

The performance of TRT detector with cosmic runs in 2008 is summarized. Figure 3.1 shows the event displays of a cosmic event in the commissioning runs. Green disk shows the TRT detector region and red or white points on the disk represent the high or low threshold hits in the TRT detector. The yellow strips in the inner region correspond to the SCT hits. The orange line shows a cosmic muons traversing the Inner Detector.
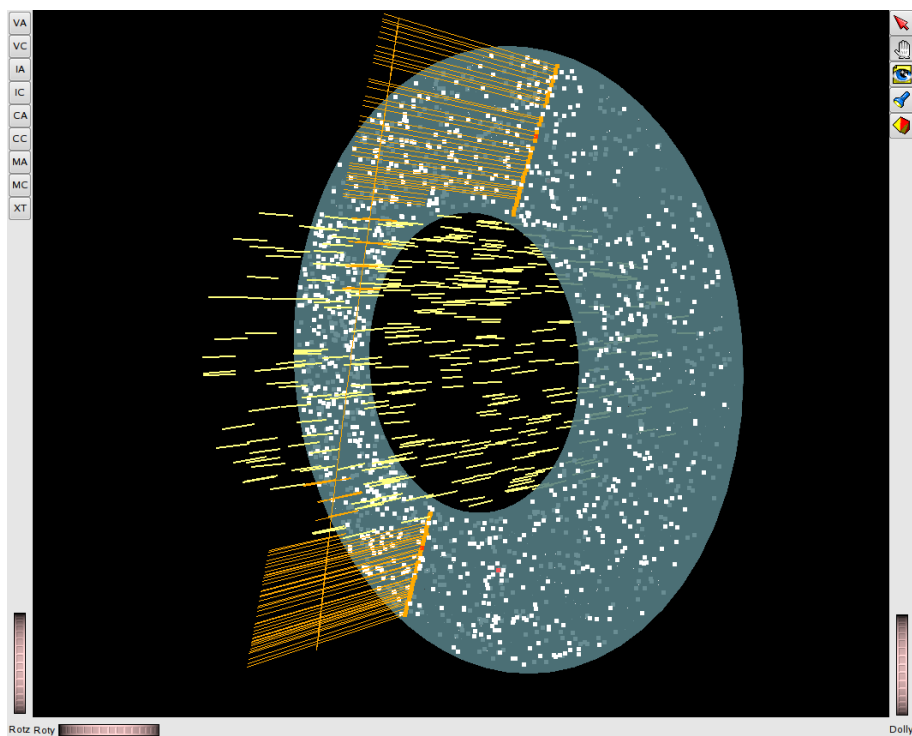
Figure 3.1: Event display of the cosmic ray obtained in the commissioning runs.

3.1.1 Occupancy Study

Some of occupancy studies are performed using cosmic data. The studies of occupancy is done by using the TRT barrel modules. The occupancy for each drift tube in this study is defined as,

$$\text{Occupancy} \equiv \frac{\text{The number of hits in a tube.}}{\text{The number of all events.}} \tag{3.1}$$

Figure 3.2 shows the occupancy distributions in different runs. Occupancy of most of drift tube is around 2%. Figure 3.3 the average occupancy of whole drift tubes. The average occupancy is about 2.2%.
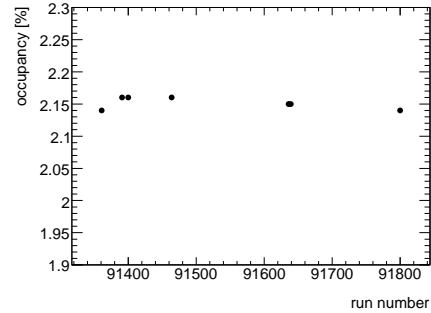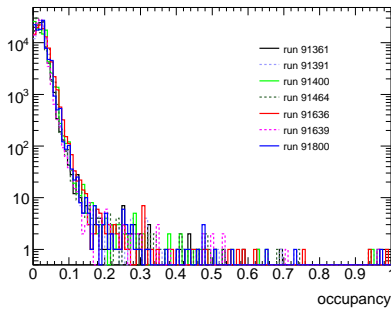
Figure 3.2: Occupancy distributions in cosmic runs.

Figure 3.3: The average occupancy of the barrel module in cosmic runs.

The average occupancies for different phi-module on both side are shown in Figure 3.4. The TRT barrel module can be divided into 32 modules in ϕ direction. There are totally 96 phi-modules in each side. The average occupancy in most of phi-module results in about 2.2%. The average occupancy of TRT barrel detector is nearly 2.2%. The noise level of TRT detector
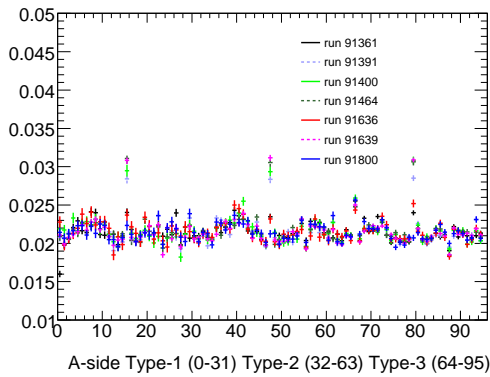
(a) A-side
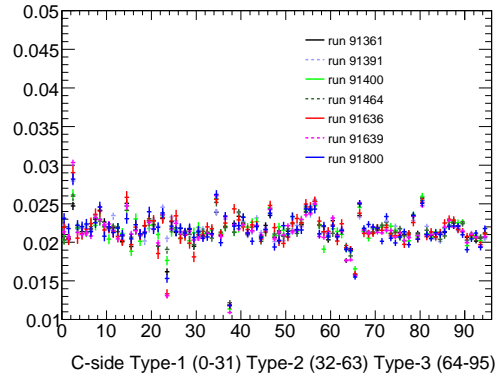
(b) C-side

Figure 3.4: The average occupancy in each straw layers. (a) and (b) shows the average numbers of the module of A-side and C-side, respectively.

is stable at cosmic runs.

3.1.2 Efficiency Study

Efficiency studies are also performed with cosmic data. Similarly to the occupancy study, this studies done for the barrel module. The reconstructed tracks are employed in order to estimate the efficiency of the TRT drift tubes. Using the reconstructed tracks of cosmic rays, hit efficiency as a function of the distance from track to drift wire is defined as,

$$\varepsilon(d) \equiv \frac{N_{\text{hits}}}{N_{\text{tubes}}}, \tag{3.2}$$

where d is the track distance to the drift wire, N_{hits} is the number of hits in tube whose track distance is d and N_{tubes} is the number of tubes whose track distance is d.

For the efficiency study, these track selection criteria are required:

- $p_{\text{T}} > 1$ GeV.

- $N_{\text{pixel}} \geq 1$.

- $N_{\text{SCT}} \geq 6$.

- Quality selection for the SCT only track. Using the SCT information of the cosmic track, the SCT only track is reconstructed. Good quality for the SCT only track is required.

$$\chi^2/n.d.o.f < 5 \tag{3.3}$$

- The residual cut for the last TRT hit. The selection requirements for the last hit of the track of cosmic ray traversing the whole of the Inner Detector. Using a drift radius and a track distance as shown in Figure 3.5, the residual is defined as

$$\text{residual} \equiv \text{drift radius} - \text{track distance.} \tag{3.4}$$

As a selection criterion, |residual| < 0.3mm is required. This selection removes the effect of multiple scattering. Figure 3.6 shows the efficiency distributions of the TRT drift tubes. The black line shows the efficiency without the residual selection. On the other hand, the red line shows the efficiency with the residual selection. The efficiency with residual selection falls steeply around $d \sim 2$mm which is corresponding to the radius of the drift tubes due to the removal of the multiple scattering effects.

Figure 3.7 shows the efficiency for different types of modules as a function of a track distance. The efficiency in the plateau region that the track distance is less than 2mm is above 90%. The efficiency for the type-2 module is given by about 93%. The method of the estimation for the efficiency is affected by the precision of tracking or the alignment of the detectors. The efficiency of the TRT detector in this study results in above 90%.

3.2 Performance of TRT with pp Collision data of $\sqrt{s} = 7$ TeV

The performance of TRT detector in 2011 runs [45] is summarized here.
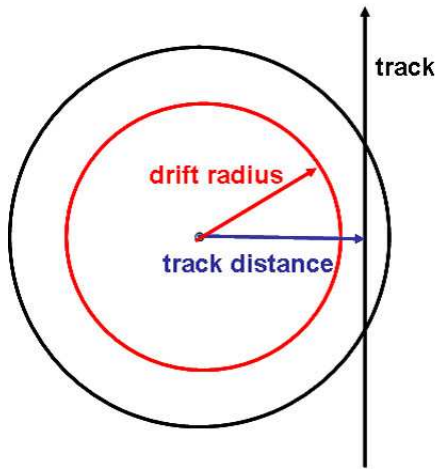
Figure 3.5: The residual of the track position.
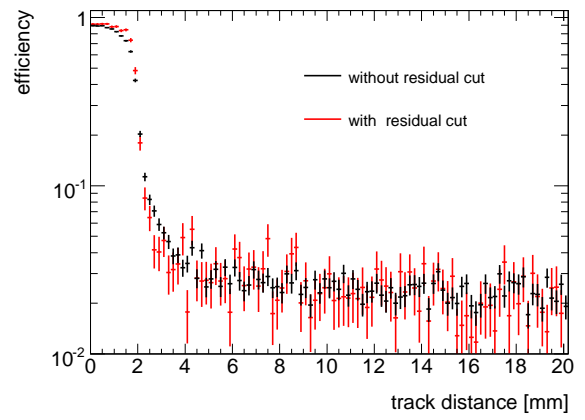
Figure 3.6: TRT hits efficiency with or without residual selections.
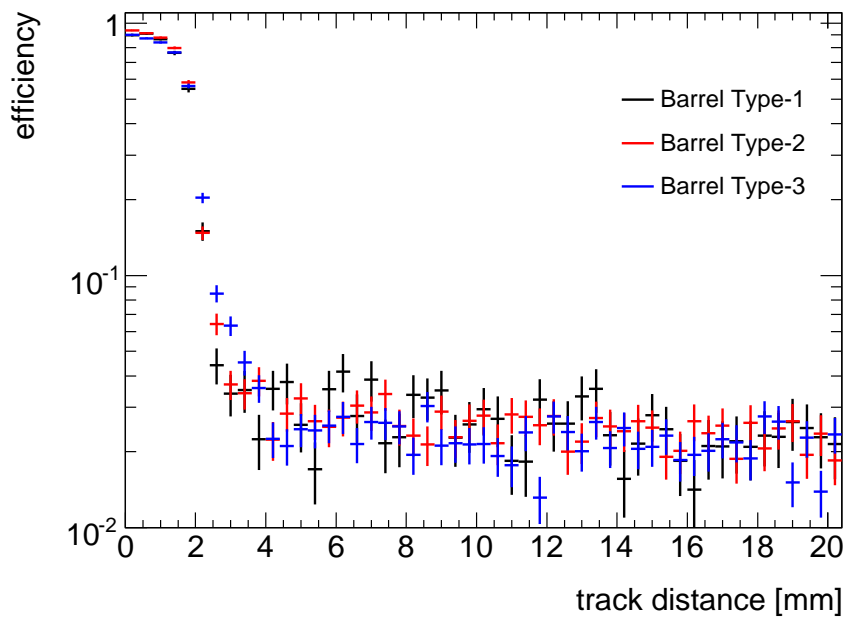
Figure 3.7: TRT hits efficiency for different barrel modules.

69

3.2.1 Occupancy Study

Figure 3.8 shows average number of hit occupancy as a function of straw layer in the barrel module. Occupancies are shown for different number of the reconstructed vertices. The first nine layers are the innermost layers. They are shorten in order to keep the occupancy low as described in Section 2.2.3.
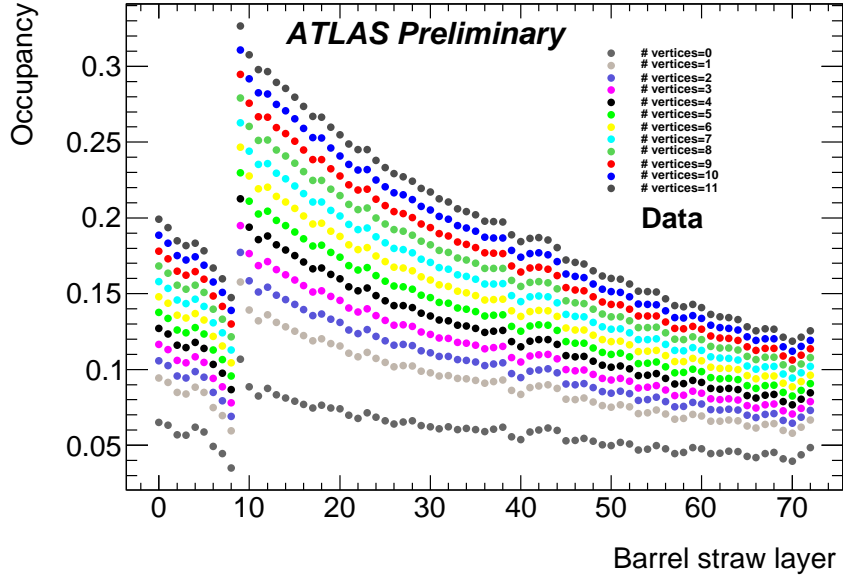
Figure 3.8: Average number of hit occupancy in each straw layer of the barrel module.

3.2.2 Efficiency Study

Figure 3.9 shows the TRT hit efficiency as a function of the distance from track to the straw center. Only straws between the first and the last layers with a hit on the track is considered for the estimation of the efficiency. The corresponding the first and the last layer is removed for the calculation. The tracks are required to have at least one pixel hit and six SCT hit and fifteen TRT hits. Furthermore, $p_{\mathrm{T}} > 1$ GeV, $|d_0| < 10$mm and $|z_0| < 300$mm are also required. The efficiency for data and MC are about 94% and 95% respectively in the plateau region which is defined by the solid lines. The threshold simulated in the Monte Calro is tuned to the data with the center-of-mass energy $\sqrt{s} = 900$ GeV.
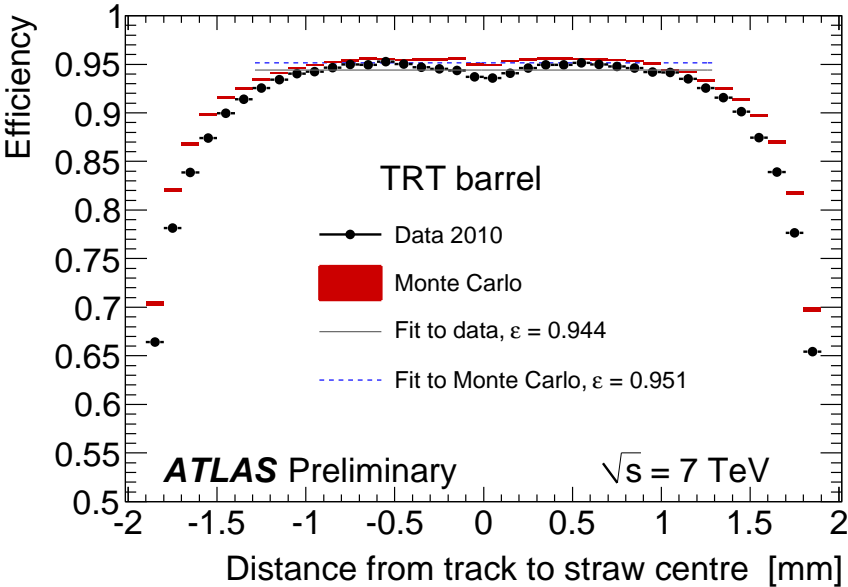
Figure 3.9: TRT efficiency as a function of a distance from track to the wire.

Chapter 4

Analysis Overview

4.1 Event Topologies of the AMSB Model

4.1.1 Production Processes

Two types of production processes of the AMSB models could occur in pp collisions at the LHC.

- Pair production of colored sparticles via strong interaction.
  A pair of colored sparticles such as gluinos are produced via strong interactions. Colored sparticles have heavier masses than those of gauginos, therefore, the cross section of this process is small. However, the high momentum jets are emitted from the cascade decay of these colored sparticles and the signal events in pp collisions are effectively triggered.

- Pair production of gauginos via electroweak interactions.
  Charginos could be directly produced via electroweak interactions. The $\tilde{\chi}_1^\pm$ has a lighter mass than that of colored sparticle, which leads to a larger production cross section. While this process has larger cross section, triggering signal events with this process is challenging because objects such as jets in this events are soft or absent.

This analysis is dedicated to the colored sparticle pair production process. The colored sparticles produced in pp collision decay to lighter sparticles, leading to the final state with multiple jets. Furthermore, these jets become energetic due to the heavy mass of the colored sparticle.

The lightest chargino could be emitted in the cascade decay of the colored sparticles. When lifetime of the long-lived chargino is long enough to decay inside the tracking volume of the ATLAS detector, a signal of the chargino is expected to be fully detected. Characteristics of chargino signals in the ATLAS experiment is summarized in the following section. The lightest neutralino (as the LSP) from chargino is energetic and escapes detection, therefore, large missing transverse momentum is expected to be observed when the signal is produced.

4.1.2 Characteristics of the Chargino Signal in the ATLAS Experiment

Expected signatures of the chargino signals depend on the lifetime, namely the position where $\tilde{\chi}_1^\pm$ decays in the ATLAS detector.

- Decaying before entering the inner tracking volumes. (Decay length is $\sim O(1)$ mm)
  In the case that $\tilde{\chi}_1^\pm$ decays promptly, the $\tilde{\chi}_1^\pm$ does not leave any hits in the detector. The large missing transverse momentum is expected but the detection of the chargino is impossible.

- Decaying in the silicon detectors.(Decay length is $O(1) \sim O(10)$ mm)
  If the lightest chargino decays in the silicon detectors, an associated short track is expected be detected. This short track has large $\mathrm{d}E/\mathrm{d}x$ hits due to its heavy mass. However, the large number of hits from underlying low momentum particles such as pions makes it hard to reconstruct the short track.

- Decaying in the TRT detector.(Decay length is $O(10) \sim O(100)$ mm)
  The $\tilde{\chi}_1^\pm$ decaying in the TRT detector is fully reconstructed with the standard track reconstruction employed in the ATLAS experiment, as stated in Section 5.2.1. The TRT detector consists of a large number of drift tubes, then charged particle makes numerous hits in the detector, which results in a visible trajectory along the path of charged track. Such a signal is observed as a track breaking up in the TRT detector.

In the AMSB models, the decay length of the lightest charginos are preferred to be $O(1) \sim O(10)$ cm and a fraction of the charginos could decay inside the tracking volume.

Figure 4.1 shows the track reconstruction efficiency for the decaying charginos as a function of the transverse distance R of the decay point. The reconstruction efficiency reaches nearly 100% for the charginos decaying after the fourth SCT layer which is located at $R = 514$ mm.
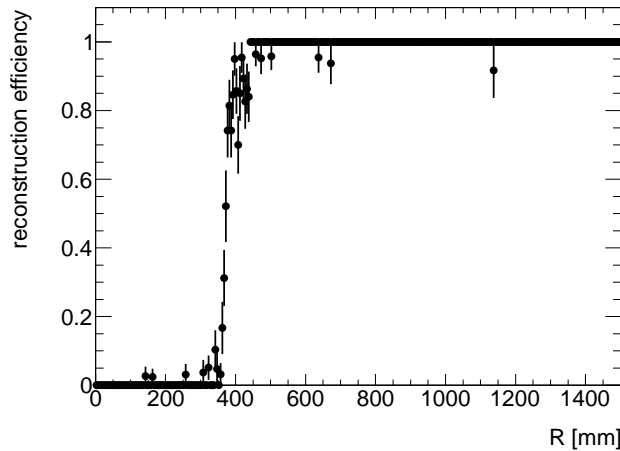
Figure 4.1: The track reconstruction efficiency for the decaying charginos as a function of the radial distance of the decay point.

The chargino track has high p_T and is well isolated from the other tracks. Figures 4.2 (a) and (b) show distributions of the chargino track p_T and the minimum distance in the η-ϕ space ΔR between the chargino track and other tracks in various AMSB models. The parameters of these AMSB models used in these figures are described in Section 5.3.2. The difference between colored sparticles and chargino masses is so large that produced charginos have large momentum.

The number of TRT hits along the chargino track is employed in order to identify decaying chargino. A Chargino decays to a neutralino, which escapes from detection, and a soft charged

(a) p_T of chargino tracks

(b) Minimum ΔR between chargino track and other track
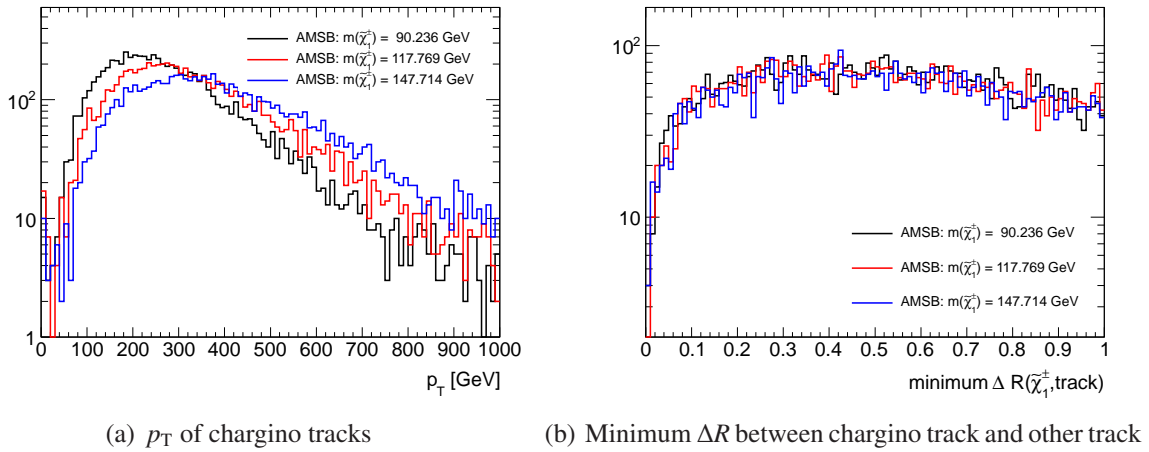
Figure 4.2: Distribution of the chargino track p_T and the minimum ΔR between the chargino and other tracks in various AMSB models. The normalization of AMSB signals is not taken into account.

particle which is hard to be reconstructed. Chargino makes many hits in the TRT before its decay. The track break up at decay point and there is expected to be few hits arising from noise or other particles on the trajectory of reconstructed track of chargino, as illustrated in Figure 4.3. Therefore, chargino is expected to be determined by counting the number of TRT hits on the track. The distribution of the number of TRT hits on chargino track is shown in Figure 4.4. It is proportional to the decay radius of chargino and provide discrimination from background tracks originating from stable charged particles. TRT consists of three modules in depth as described in Section 2.2.3. The inner, middle, and outer is called Type-1, Type-2, and Type-3, respectively. When a chargino decays in the TRT Type-1 or Type-2, nearly zero hit is expected in the Type-3 while, the average number of hits on a ordinary track is about 34 in the whole TRT detector. In the Type-3 module, the average number of hits is about fifteen. Figure 4.5 shows the number of TRT Type-3 hits distribution of the reconstructed chargino tracks penetrating the TRT barrel module ($|\eta| < 0.63$). $N_{\mathrm{TRT}}^{\mathrm{outer}}$ is expected to give nearly zero when chargino decays before the TRT Type-3 module. On the other hand, $N_{\mathrm{TRT}}^{\mathrm{outer}}$ is expected to be about fifteen if a track penetrates the TRT detector.
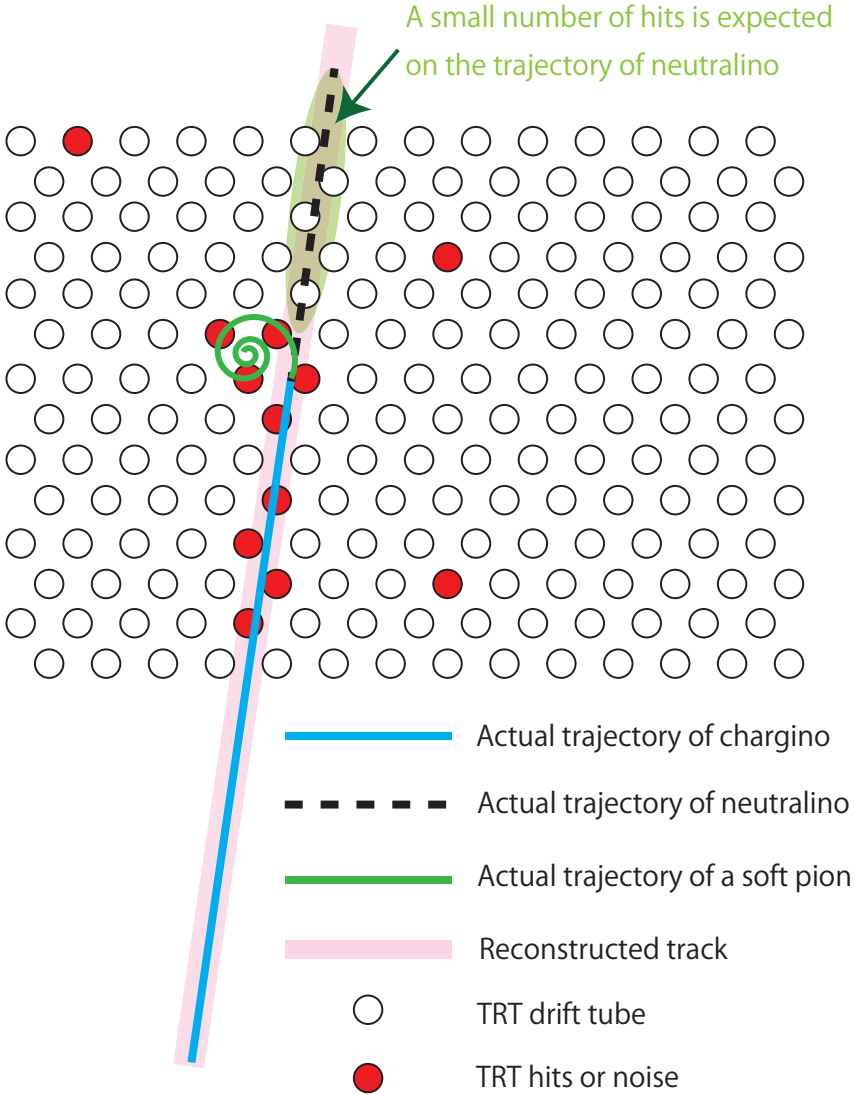
Figure 4.3: Decaying chargino in the TRT detector.
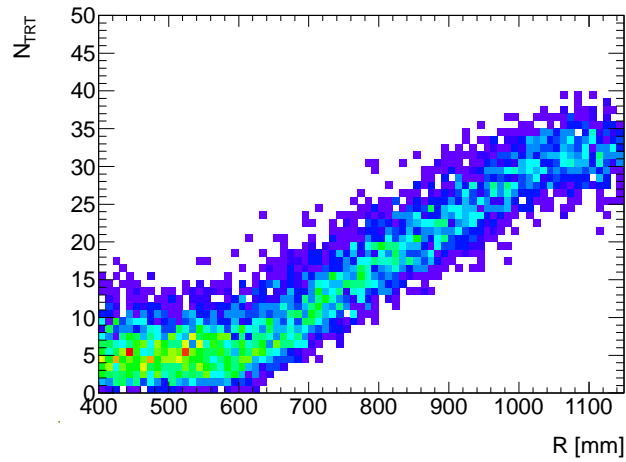
Figure 4.4: The number of TRT hits of reconstructed chargino tracks with $|\eta| < 0.63$ as a function of its decay R. TRT is instrumented between $R = 563$ mm and 1066 mm.
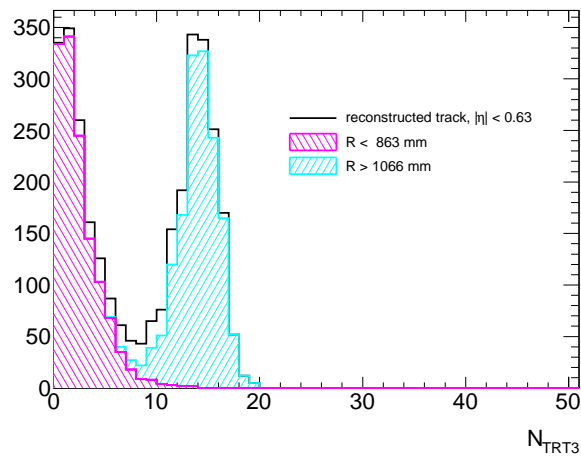
Figure 4.5: The $N_{\text{TRT}}^{\text{outer}}$ distribution of reconstructed chargino tracks with $|\eta| < 0.63$. Black line shows all the reconstructed chargino track.Magenta shaded and blue shaded histograms are the tracks which decay before the TRT Type-3 module and the tracks which penetrates the whole TRT detector, respectively.When charginos decay before reaching (after penetrating) the TRT type-3 module, $N_{\text{TRT}}^{\text{outer}}$ gives nearly zero (fifteen).

Chapter 5

Dataset and Monte Carlo Simulation

5.1 Data Preparation

5.1.1 Analysis Framework

Most of studies on performance or physics are performed via a common analysis framework, which is called ATHENA [46]. ATHENA software framework is an enhanced version of the C++ based software framework GAUDI [47] which is initially developed by the LHC-b collaboration. ATHENA enables a user to implement an algorithms easily for studies using data or Monte Carlo simulation of ATLAS. In order to run ATHENA, scripts written in Python are used. Detector description, software setup, etc are specified in these scripts.

5.1.2 Software Chain in the Data Preparation

Simulated and experimental data are prepared through a series of software chain.

Event Generation

This is the first step of generation of Monte Carlo simulations. Simulation of event generation is also performed via ATHENA. ATHENA uses external softwares like PYTHIA, MC@NLO, and so on. Event of proton-proton collision is simulated by these softwares. Decays of particles before incidenting to the detector are also simulated in this step.

Simulation

This step is the simulations of particle in the detector materials. ATHENA uses the GEANT4 [48] for the simulation. GEANT4 provides physics models in the detector. The geometry description of the ATLAS detector is written in the GEANT4 format. This description is provided by ATHENA. The deposited energy of particles in the active volume of the detector is calculated in GEANT4. Furthermore, decays of particles including the late-decay particle such as long-lived chargino in the detector are also calculated by GEANT4. After this step, the files containing data of energies deposited in the detector are generated.

Digitization

In this stage, the hits information generated by simulation is converted into detector responses. Detector responses are called "digits". A digit is produced if the voltage or current exceed a threshold of a readout channel within a time-window. The features of charge collection such as cross-talk and electric noise in each detector are also simulated in this step. In addition to the hard scattering, other proton-proton interaction must be considered. The response of these interactions in the detector are also simulated. Many inelastic proton-proton interaction may appear at bunch crossing. The effects of beam gas and beam halo are also incorporated in this step. Furthermore, the detector response to long-lived particles is also calculated. After the digitization step, the files containing the digits of each sub-detector. This data format is called Raw Data Object, or RDO for short.

Reconstruction

This is the last step of ATLAS software chain. In this stage, the event reconstruction is performed using experimental or simulated data of the detector. Reconstruction algorithms for physics object such as track, jet, muon, electron and $E_\mathrm{T}^\mathrm{miss}$ are deployed from detector data. After this step, two types of data format are provided. One is Analysis Object Data (AOD), which contains physics object data for analysis. The other is Event Summary Data (ESD), which holds not only physics objects but also the detector information.

Data Formats for Analysis

In the series of software chain, many of data formats are produced such as RDO, AOD and ESD. However, the access of this data is restricted due to the problem of the huge amount of the file size. There are some of data formats for physics analysis or performance study. The data formats mentioned below has small size of data for easy access.

Derived ESD (DESD)   DESD is small ESD by removing unnecessary data. ESD contains full detector information and its file size is huge. Therefore, it is necessary to lessen file size for study using ESD data. There are some operations for data reduction: Skimming, Slimming and Thinning. Skimming is removing uninteresting events. Slimming is removing details of objects. Thinning is removing unnecessary objects.

Derived Physics Data (DPD)   DPD is also data whose file size is reduced. There are different kinds of DPD. The different kinds are D1PD, D2PD and D3PD. D1PD has the same format as AOD. D1PD is provided by the GRID production system. D1PD is not very specific to analysis. D2PD also has the same format as AOD. D2PD is more analysis-specific than D1PD. D1PD and D2PD can be read with ATHENA. D3PD is different from the other DPD and it contains flat ntuples. Many analyzers in ATLAS use D3PD data.

5.2 Object Reconstruction

At the reconstruction stage of the software chain, many of physics objects are reconstructed. These objects are used for physics analysis or the performance study. The detail of reconstruction algorithm for each object is explained here.

5.2.1 Track Reconstruction

The reconstruction algorithm of the inner track [49, 50] employs the data of the Inner Detector. The tracking algorithm of ATLAS is called *New Tracking* or *NEWT* for short. The NEWT covers two reconstruction algorithm: the main algorithm is *inside-out* track reconstruction and the consecutive algorithm is *outside-in* tracking.

Track Parametrization

Track is described with the parameters at *Perigee*, which is the closest point to the beam-pipe (z-axis). Parameters at perigee, $P(x_P, y_P, z_P)$ for track with momentum $\boldsymbol{p} = (p_x, p_y, p_z)$ and charge Q is summarized in the Table 5.1.

Table 5.1: Track parameters at perigee

d_0	: Transverse impact parameter	$d_0 = \pm \sqrt{x_P^2 + y_P^2}$
z_0	: Longitudinal impact parameter	$z_0 = z_P$
ϕ_0	: Azimuthal angle at perigee	$\phi_0 = \arctan(\frac{p_y}{p_x})$
θ	: Polar angle at perigee	$\theta = \text{arccot}(\frac{p_z}{\sqrt{p_x^2 + p_y^2}})$
$\frac{q}{p}$	: Q over P	$\frac{q}{p} = \frac{Q}{|\boldsymbol{p}|}$

The convention of the sign of d_0 is following: May ϕ denote the azimuthal angle of the perigee, i.e. $\phi = \arctan(\frac{y_P}{x_P})$. The sign of d_0 is defined as positive if $\phi = \phi_0 + \frac{\pi}{2} + 2n\pi$ where n is an integer.

Inside-Out Track Reconstruction

The first step of the inside-out track reconstruction is the formation of the three-dimensional information using the silicon detector measurements, which is called `SpacePoint`. The formation of the `SpacePoint` objects with the pixel detector is performed by the simple way. The measurements on the pixel module has two-dimensional information and the three-dimensional representation is obtained by using the constraint of the information for detector element which is called the `Surface`. On the other hand, the `SpacePoint` objects cannot be formed from the single SCT measurements because the SCT is the strip sensor detector. However, a module of the SCT detector is built with two sensor rotated with each other. Therefore, three-dimensional information is obtained by using two strip measurements. The pixel detector can give directly the `SpacePoint` but the formation of `SpacePoint` with the SCT detector needs two measurements. That leads an intrinsic noise suppression in the SCT `SpacePoint` formation at the very first pattern recognition.

The `SpacePoint` objects formed with the silicon detector are collected for seeding the track candidate. This procedure has two different tasks which are the track seed finding and the track candidate creation.. There are two different seed finding algorithm:

- Seed search with z vertex constraint: `SpacePoint` pairs of the pixel detector are employed and z vertices are created. The vertices are filled in histograms and the seeds are selected if they are in the tolerance region for predicted vertices.

- Unconstrained seed search: The seed search without z vertex constraint is also prepared. This procedure leads to be more time consuming but the more efficient to find tracks in events.

After the `SpacePoint` seeds are obtained, the "road " building process is started. The seeds provide directional information to build roads and enables to associate hits in the detector to a track candidate. In this stage, a Kalman fitter-smoother formalism is employed to follow the trajectory and include successive hits in the track fit simultaneously. The Kalman filter progressively updates the track information and predicts precisely the track representation on the next detector measurement.

The seeded track finding leads to a large numbers of track candidates. Many of these track candidates share hits with other candidates. These candidates are incomplete tracks or fake tracks whose hits are not originate from a single particle. Therefore these track candidates are ordered by the likelihood to describe the real trajectories of particles. This procedure is called *Ambiguity Solving*. The first step is refitting the track using the refined reconstruction geometry. Nevertheless, the track fit only gives reduced chi-square and this parameter does not discriminates a good track from a fake track. Then, the *track scoring* strategy is developed for the classification of tracks. This strategy uses the different characteristics of tracks which is represented by a beneficial or penalty score. For the scoring, the associating hits on the track is employed. The measurements of different sub-detectors are weighted and the precision measurements such as the pixel detector has preferred.

Table 5.2: Track characteristics in the track scoring.

Track characteristics	Detector	Track scoring
B-layer hole	pixel	strong penalty
Layer hole	pixel	penalty
Overlap hit	pixel,SCT	strong benefit
Sensor hole	SCT	weak penalty
Layer hole (module)	pixel	strong penalty

The silicon track obtained from these procedures are extended into the TRT detector. The tracks determined by the silicon seeds are used as an input for finding TRT measurements corresponding to the tracks. These TRT measurements are further processed for extension of tracks. After the association of TRT hits to the track, comparisons of the refitted combined track and the silicon seeded track are performed based on the track scoring. In case that the track score of the silicon seeded track is higher than the combined track, the silicon track is kept and the TRT measurements are categorized as outlier on the track.
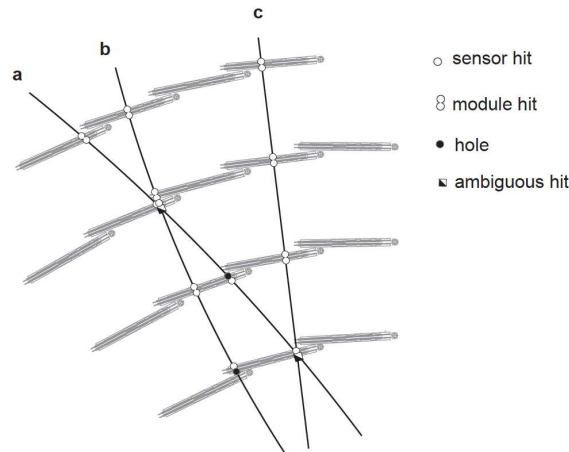
Figure 5.1: Illustration of the ambiguity solving in the SCT module. Tracks a,b and c are found by the seeded track finding. Module hit of the SCT detector is scored relatively higher. Hits in a overlap region for track b are high scored. On the other hand, holes where hits are expected results in a penalty.

Outside-In Track Reconstruction

In the inside-out track reconstruction process, some of initial track may not be found. For example, tracks originating from secondary decay vertices such as K_s decays inside the Inner Detector or tracks from photon conversions may not make sufficient hits in the silicon detector. Accordingly, the outside-in track reconstruction algorithm is developed.

The fist stage of the outside-in reconstruction is TRT segment finding. This algorithm follows the two-step procedure, which is starting with global pattern recognition and a subsequent local pattern recognition. The TRT measurements can not provide the information about the coordinate along to the straw direction. The `SpacePoint` objects are not formed by the TRT measurements. Therefore, the global pattern recognition is performed in the projective plane: r-ϕ plane is adopted for the TRT in the barrel region and r-z plane is employed for the TRT in the end-cap region. The Hough transform technique, which is a very common technique in high energy physics, is adopted for The global pattern recognition. After the TRT track segments are obtained by the global pattern recognition, these segments are further processed in a second step of the TRT segment finding. The local pattern recognition algorithm uses the information of drift time while the global pattern recognition employs only the straw center. Eventually, the track segments are obtained via a Kalman filter-smoothing formalism. In the second stage, the track segments are extended towards the silicon detector. If the track extension towards the silicon detector is failed, this track is categorized as the *TRT-standalone tracks*.

Common Tools Using Tracking Software

- `ATLAS Extrapolator`[51]
  The estimation of track parameters on a given detector surface and their associated covariances is a important process in track reconstruction. Track fitting techniques such as the

Kalman Filter formalism relies on the prediction of the track information on successive surface.

The `ATLAS extrapolator` mainly consists of three different tasks: propagation, navigation and integration of material effects. In the task of propagation, track parameters on a destination surface are estimated by the initial parameters and the traversed magnetic field. The various techniques are implemented for propagation of tracks. The propagation with a straight line model or a helical track model is assuming no magnetic field or a homogeneous magnetic field. These method are employed for the runs using cosmic rays or test beam. The propagation with the Runge-Kutta-Nyström integration technique is mainly used in a inhomogeneous magnetic field. In the navigation task, the information about the traversed detectors are gathered. In the task of material effects integration, the material effects for a particle is estimated. A particle traversing material is affected the energy loss and scattering. Multiple scattering is a stochastic process with zero mean deflection. This effect is regarded as Gaussian or multi-Gaussian process noise addition to the track covariance. Energy loss effects changes the trajectory of a particle and the uncertainties on the track of the particle because of the loss of the momentum. These effects are taken into account by a deterministic mean value.

The `ATLAS Extrapolator` is employed for the TRT association to the track for this chargino track search.

- `TrackToCalo` tool
  `TrackToCalo` is the tool for track extrapolation in the calorimeters. `TrackToCalo` tool employs the `ATLAS Extrapolator`. When the track information and the depth of the calorimeter are fed into the tool, `TrackToCalo` tool calculates the track position in the calorimeter. For propagation, Runge-Kutta technique is used similarly to the `ATLAS Extrapolator`. This tool is also used in this analysis in order to associate calorimeter clusters to track.

5.2.2 Vertex Reconstruction

The iterative vertex finding approach is used for vertex reconstruction [52, 53]. Reconstructed tracks originating from the interaction region are employed for vertex reconstruction. The procedures of primary vertices reconstruction have two steps. The first step is the primary vertex finding algorithm, which is dedicated for the association the reconstructed tracks to the vertex candidates. The second step is the vertex fitting algorithm, which is dedicated for the reconstruction of vertex position and the error matrix of it.

The seed of the vertex is obtained by looking for the global maximum of z-coordination of the tracks at the point of the closest approach to the beam spot. The vertex position is determined by the *adaptive vertex fitting* [54] algorithm, which makes use of the seed position and the tracks. The adaptive vertex fitter is a robust χ^2 based fitting algorithm which deals with outlying tracks by down-weighting their contribution to the overall. The weight w_i depends on the compatibility of the i-th track with the vertex, which is measured as χ^2,

$$w_i(\chi_i) = \frac{\exp(-\chi_i^2/2T)}{\exp(-\chi_i^2/2T) + \exp(-\chi_c^2/2T)} \tag{5.1}$$

where χ_c^2 defines the threshold that the weight is equal to $\frac{1}{2}$ and the temperature T is a parameter which defines the functional shape of weights. The shape of the weight results in the step function when T approaches to zero.

Tracks displaced by more than 7σ are removed from the vertex and used to make a new vertex candidate. A vertex is required that more than two tracks must be associating to the vertex. The compatibility of the track to the vertex is expressed by χ^2. The default selection is $\chi^2 > 49$. This procedure of the vertex finding algorithm is repeated until new additional vertices are no longer found.

5.2.3 Calorimeter Cluster Reconstruction

Calorimeter cluster is reconstructed as inputs for jet-finding in ATLAS. There are various algorithms for clustering the calorimeter energy.

- Tower algorithm
  The calorimeter cells segmented into bins of a $\Delta\eta \times \Delta\phi = 0.1 \times 0.1$ grid. The towers are formed by collecting the cells and summing up their signals. When the information of the cells are summed up, all calorimeter cells are merged. Towers with negative energy is dominated by noise; therefore, these towers are not used when jet-finding algorithms are applied.

- Topological clustering algorithm
  Topological clustering algorithm attempts to reconstruct three-dimensional energy depositions using the calorimeter cells. At first, the nearest neighboring cells which absolute energy exceeds the major seed threshold, i.e. $|E_{\text{cell}}| > 4\sigma_{\text{cell}}$ where the total noise is represented as σ_{cell} are collected and the seed of the calorimeter cluster is formed. Then, if the neighboring cells whose absolute energy is above a secondary seed threshold, typically $2\sigma_{\text{cell}}$, these cells are merged to the primary seeds. Finally, all the surrounding cells are added when the energy of the cell exceeds the $0\sigma_{\text{cell}}$.

  Topological clustering algorithm suppress the actual noise contrary to the tower algorithm. In this algorithm, the cells with no signal are not likely to be include in the cluster.

- Sliding window algorithm
  The sliding window algorithm also makes use of cells segmented into $\Delta\eta \times \Delta\phi = 0.1 \times 0.1$. This algorithm uses the sliding window with programmable size.

5.2.4 Jet Reconstruction

The jet reconstruction employs "anti-k_t"algorithm [55]. This algorithm makes use of the reconstructed cluster of calorimeter. In this algorithm, d_{ij} is defined as,

$$d_{ij} \equiv \min(p_{Ti}^{-2}, p_{Tj}^{-2})\frac{\Delta_{ij}^2}{R^2} \ (i \neq j, \ R = 0.4 \, or \, 0.6), \tag{5.2}$$

$$d_{ii} \equiv p_{Ti}^{-2}, \tag{5.3}$$

where $\Delta_{ij}^2 = (y_i - y_j)^2 + (\phi_i - \phi_j)^2$ and p_{Ti}, y_i and ϕ_i are transverse momentum, rapidity and azimuthal angle of the cluster i. All of the clusters are ordered by p_T^{-1} and d_{min} for the i-th cluster is defined as

$$d_{min} \equiv \min(d_{ii}, d_{ij}). \tag{5.4}$$

The cluster i is considered as a jet when d_{min} is equal to d_{ii}. If d_{min} is not d_{ii}, the i-th cluster is merged with the j-th cluster by calculating vector sum of four-momenta of clusters. Then d_{min} of the new cluster object is evaluate for all the remaining clusters. This procedure is repeated until the all of the jet candidates are not remained.

5.2.5 Electron Reconstruction

Electron reconstruction [56, 57] in the region of $|\eta| < 2.47$ starts from searching for clusters in the EM calorimeter which are then associating to a reconstructed track in the Inner Detector. In order to reconstruct the EM clusters, seeds of cluster which transverse energy $E_T > 2.5$ GeVare searched for by sliding window algorithm. The window size is 3×5 in units of 0.025×0.025 in $\eta \times \phi$ space. Reconstructed tracks in the tracking volume of $|\eta| < 2.5$ are extrapolated to the middle layer of the calorimeter and loosely matched to seeds. The distance between the track position at the middle layer and the cluster position is required to satisfy $\Delta\eta < 0.05$. In order to take into account for bremsstrahlung losses, $\Delta\phi < 0.1$ is required on the side where the track bends in the solenoid field and $\Delta\phi < 0.05$ on the other side. An electron is reconstructed if at least one track is matched to the seed. In the case that more than one tracks are matched to the seed, a track with the silicon hits is preferred and the one with the smallest ΔR is to the seed is selected. The electron cluster is rebuild by using 3×7 (5×5) longitudinal tower of calorimeter cells in the barrel (end-caps). The cluster energy is determined employing four different contributions: the estimated energy deposit in the materials in front of EM calorimeter, the measured energy deposition in the cluster, the estimated external energy deposition outside the cluster (lateral leakage) and the estimated external energy deposition beyond the EM cluster (longitudinal leakage). The four-momentum of electron is calculated using information of both the track and the calorimeter cluster. The electron energy is given by the calorimeter cluster. The η and ϕ directions are determined by using the track information.

In the forward region of $2.5 < |\eta| < 4.9$, where there are no trackers, electrons are reconstructed by employing only deposited energy in the calorimeters. The topological clustering algorithm is used for reconstruction of forward electrons. The direction of the electron is determined by the barycenter of the cells associating to the cluster. The energy of the electron is calculated by summing up the energies in the cluster of the cells and is corrected for energy loss in the passive material before calorimeter. The candidate of electron is required that it has a small hadronic energy component and a transverse energy $E_T > 5$ GeV.

5.2.6 Muon Reconstruction

Two independent muon reconstruction algorithms are implemented in the ATLAS:*STACO (Statistical Combined)* [58, 59] and *MUID (Muon Identification)* [60, 61]. In order to identify muons, the tracks which are reconstructed in the Inner Detector and the Muon Spectrometer are combined. STACO is based on the statistical combination of two independent measurements of

track parameters and the covariance matrices. On the other hand, MUID is based on the fitting the global muon track using hits in the Inner Detector and the Muon Spectrometer.

STACO

In the STACO algorithm, the standalone muon tracking package is called *Muonboy*. The strategy of the muon tracking in Muonboy consists of the main four steps:

1. Identification of Regions of Activity (ROA) in the muon system with trigger chambers.

2. Reconstruction of local straight track segments in each muon station of these ROA.

3. Combination of track segments in different muon station.

4. Global track fit of the muon track.

Furthermore, the back-tracking of the muon candidates to the beam region is performed to obtain the track parameters at the perigee. When the back-tracking is performed, the energy loss and the scattering in the calorimeter are also taken into account.

The match chi-square is used in order to combine the standalone muon track and the track reconstructed in the Inner Detector,

$$\chi^2_{\text{match}} = (\boldsymbol{\xi}_{\text{MS}} - \boldsymbol{\xi}_{\text{ID}})^{\text{T}}(\boldsymbol{\Sigma}_{\text{MS}} + \boldsymbol{\Sigma}_{\text{ID}})^{-1}(\boldsymbol{\xi}_{\text{MS}} - \boldsymbol{\xi}_{\text{ID}}), \tag{5.5}$$

where ξ are the track parameters and Σ are the covariance matrix of the track parameters. After matching the tracks reconstructed in the Inner Detector and the Muon Spectrometer, the parameters of the combined track is obtained as,

$$\boldsymbol{\xi}^{\text{STACO}}_{\text{match}} = (\boldsymbol{\Sigma}^{-1}_{\text{MS}} + \boldsymbol{\Sigma}^{-1}_{\text{ID}})^{-1}(\boldsymbol{\Sigma}^{-1}_{\text{MS}}\boldsymbol{\xi}_{\text{MS}} + \boldsymbol{\Sigma}^{-1}_{\text{ID}}\boldsymbol{\xi}_{\text{ID}}). \tag{5.6}$$

MUID

MUID also has the standalone muon tracking package which is called *MOORE (Muon Object Oriented Reconstruction)*. The strategy of tracking in the muon spectrometer in the MOORE is,

1. A global pattern recognition with Hough transformation using hits in the Muon Spectrometer.

2. Straight MDT segments and straight CSC segments are formed with hits obtained by the pattern recognition.

3. The track segment are refitted and the track are built.

After building tracks, the refitted muon tracks are extrapolated to the beam region. Then tracks are matched by forming a χ^2. A combined fit requires that χ^2 probability is above 0.001. If this criterion is not satisfied, the fitting attempts for the best match using the measurements within a road of a muon track. Eventually, all matches to the Inner Detector which fulfill the requirements of the combined fit are identified as combined muons.

5.2.7 Missing Transverse Energy Reconstruction

The missing transverse energy E_T^{miss} includes contributions from energy deposits in calorimeters and muons reconstructed in the muon spectrometer [62]. The missing energy in $x(y)$-direction is defined as,

$$E_{x(y)}^{\text{miss}} = -\sum E_{x(y)}^{\text{calorimeter}} - \sum E_{x(y)}^{\text{muon}}. \tag{5.7}$$

where $E_{x(y)}^{\text{calorimeter}}$ and $E_{x(y)}^{\text{muon}}$ are each component of deposited energies in calorimeter and reconstructed muons. The values of E_T^{miss} and its azimuthal angle (ϕ^{miss}) is calculated as,

$$E_T^{\text{miss}} = \sqrt{(E_x^{\text{miss}})^2 + (E_y^{\text{miss}})^2}, \tag{5.8}$$

$$\phi^{\text{miss}} = \arctan(\frac{E_y^{\text{miss}}}{E_x^{\text{miss}}}). \tag{5.9}$$

E_T^{miss} definition depends on what term is employed in calculation. The various term is described in the following:

- $E_{x(y)}^{\text{miss},e}$, $E_{x(y)}^{\text{miss},\mu}$ and $E_{x(y)}^{\text{miss},\tau}$
  Reconstructed missing energy from cells in clusters associated to electrons, muons, and τ-jets from hadronically decay, respectively.

- $E_{x(y)}^{\text{miss,jets}}$
  Reconstructed from cells in clusters associated to jets with calibrated p_T >20 GeV.

- $E_{x(y)}^{\text{miss,softjets}}$
  Reconstructed from cells in clusters associated to jets with 7 GeV< p_T <20 GeV.

- $E_{x(y)}^{\text{miss,calo},\mu}$
  The contribution to E_T^{miss} originating from the energy lost by muons in the calorimeter.

- $E_{x(y)}^{\text{miss,CellOut}}$
  Calculated from the cells in topoclusters which are not included in the reconstructed objects.

5.3 Collision Data and Monte Carlo Simulation

Collision data and Monte Carlo simulation samples concerning this analysis are described here.

5.3.1 Collision Data

This analysis used the data of pp collisions at $\sqrt{s}$ = 7 TeVwith collected at the ATLAS detector in 2011. Figure 5.2 shows the evolution of cumulative luminosity in 2011. The green filled histogram shows the luminosity delivered by the LHC while the yellow histograms show the luminosity recorded by the ATLAS detector. The delivered luminosity accounts for the luminosity from the start of the stable beams until the LHC requests the ATLAS to be off for a beam dump or beam studies. In the AMSB model with colored sparticle pair production process,
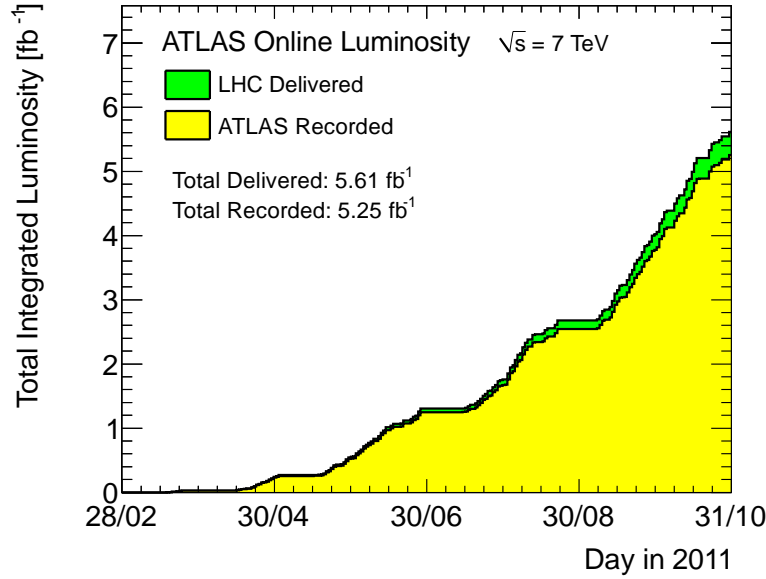
Figure 5.2: Cumulative luminosity delivered from the LHC (green) and recorded by the ATLAS detector (yellow) during stable beam.

gluinos and squarks are expected to be produced via the strong interaction in pp collisions. As mentioned in Section 4.1, the cascade decay of sparticles to the $\tilde{\chi}_1^{\pm}$ and $\tilde{\chi}_1^0$ produces multiple jets with high momentum. The large missing transverse energy of $\tilde{\chi}_1^0$ also expected due to escape from detection. Therefore, events are selected at the trigger level by requiring at least one jet with a transverse momentum, measured at the electromagnetic scale, above 75 GeV, and a missing transverse momentum above at 55 GeV. The total integrated luminosity after the application of the beam, detector and data quality requirements is estimated to be 4.71fb^{-1}.

In addition to the data for the search for charginos, the data obtained with the pre-scaled jet trigger is employed for the studies of the tracking or the control samples for the background estimation.

5.3.2 Signal Simulation

Three benchmark points of AMSB models are used for this analysis. The mass spectrum of sparticles, the branching ratios and decay width are calculated using the ISASUSY ver.7.78. The MC signal samples are produced using HERWIG++[63] with MRST2007 LO*[64] parton distribution functions. The proper lifetime of chargino is set to 1 ns and its decay is simulated by GEANT4. The chargino lifetime follows the exponential decay with 1 ns in the rest frame. The samples with different lifetimes are also obtained by applying event weights so that the distribution of the proper lifetime follows that for a given lifetime value. All the parameters of these signal samples are summarized in Table 5.3. Parameters of these points are chosen by taking account of values of chargino masses excluded by LEP2 search. The cross sections are calculated at next-to-leading order (NLO) including next-to-leading-logarithmic (NLL) soft-gluon re-summation by using NLL-FAST[65, 66, 67, 68, 69]. Mass spectrum of sparticles for each signal point is also summarized in Table 5.4. Furthermore, the signal samples generated by

87

Table 5.3: Parameters of signal Monte Carlo samples.The NLO+NLL cross sections include only $\tilde{g}\tilde{g}$, $\tilde{q}\tilde{g}$ and $\tilde{q}\tilde{q}$ production process.

Sample	m_0[GeV]	$m_{3/2}$[TeV]	$\tan\beta$	$sgn(\mu)$	$\tau_{\tilde{\chi}_1^\pm}$[ns]	$m_{\tilde{\chi}_1^\pm}$[GeV]	Cross section[pb]
LL01	1500	32	5.0	+1	1	90.2	6.79×10^{-2}
LL02	1800	41	5.0	+1	1	117.8	8.66×10^{-3}
LL03	2000	51	5.0	+1	1	147.6	1.16×10^{-3}

Table 5.4: Mass spectrum for each benchmark point of AMSB signal. The values are in the unit of GeV.

	LL01	LL02	LL03
$\tilde{g}$	801.32	997.87	1026.39
$\tilde{u}_L$	1620.68	1961.31	2221.59
$\tilde{u}_R$	1628.73	1970.59	2232.28
$\tilde{d}_L$	1622.54	1962.84	2222.95
$\tilde{d}_R$	1632.26	1974.94	2237.44
$\tilde{b}_1$	1341.76	1627.44	1850.43
$\tilde{b}_2$	1624.37	1965.61	2226.43
$\tilde{t}_1$	991.24	1206.88	1386.47
$\tilde{t}_2$	1354.36	1640.07	1863.78
$\tilde{\chi}_1^0$	90.036	117.585	147.536
$\tilde{\chi}_2^0$	291.385	375.181	468.173
$\tilde{\chi}_3^0$	658.077	806.529	958.832
$\tilde{\chi}_4^0$	666.196	813.295	964.627
$\tilde{\chi}_1^\pm$	90.236	117.769	147.714
$\tilde{\chi}_2^\pm$	665.803	813.248	964.871
$\tilde{\nu}_e$	1489.70	1787.58	1984.52
$\tilde{e}_L$	1491.42	1788.87	1985.63
$\tilde{e}_R$	1492.21	1789.37	1985.56
$\tilde{\nu}_\tau$	1488.03	1785.59	1982.32
$\tilde{\tau}_1$	1487.22	1783.86	1979.69
$\tilde{\tau}_2$	1491.03	1787.98	1984.42
h	108.45	109.87	110.72
H	1662.69	2002.52	2251.00
A	1651.38	1989.06	2235.96
$H^\pm$	1664.15	2003.73	2252.07

`ATLFAST II` are employed in addition to these samples. Figure 5.3 show the various parameters of the minimal AMSB on the m_0-$m_{\frac{3}{2}}$ plane. Figure 5.3 (a) shows $m_{\tilde{\chi}_1^\pm}$. The chargino mass is mostly defined by the $m_{\frac{3}{2}}$, therefore, the chargino mass is mostly constant for m_0. The constraint obtained by the LEP2 experiments ($m_{\tilde{\chi}_1^\pm} > 92$ GeV) is corresponding to $m_{\frac{3}{2}} \sim 32$ TeV. Figure 5.3 (b) shows $\Delta m \equiv m_{\tilde{\chi}_1^\pm} - m_{\tilde{\chi}_1^0}$. The mass difference Δm used in this study is more than pion mass, therefore, $\tilde{\chi}_1^\pm$ decays to a soft pion and $\tilde{\chi}_1^0$ in the signal samples. Figure 5.3 (c) shows cross-section at $\sqrt{s} = 7$ TeV. The region where m_0 is too small is prohibited theoretically due to the generation of tachyonic particles. Furthermore, the region where m_0 is small ($600 < m_0 < 1000$ GeV) has slightly larger cross-section because the masses of squarks become small and squarks are generated by the pp collisions.

5.3.3 Background simulation

The signal and background events are generated at $\sqrt{s} = 7$ TeV. The background events are generated with PYTHIA [70], ALPGEN [71] and MC@NLO [72, 73]. For the events generated with ALPGEN and MC@NLO, parton showers and hadronization are simulated with HERWIG [74], and the underlying activity with JIMMY [75]. These simulated events are finally reconstructed with the same algorithms used for the data.

Following processes are backgrounds for the long-lived chargino search and considered in this analysis.

QCD Jet production: Even though the analysis requires the events to have large E_T^{miss}, due to the large cross sections of the inclusive two or multi-jet processes, this is still an important background. The events are generated with PYTHIA. The samples are generated separately for different slices of the hard process momentum, to ensure enough statistics in the large jet p_T region.

$t\bar{t}$ production: Due to the large missing transverse energy and the hard jets in the final state, this process can survive the event selection. The MC@NLO generator has been used to simulate the process. The CTEQ6.6 [76] next-to-leading-order (NLO) PDFs are used.

Boson+Jets production: The production of $W^\pm$ and Z bosons in association with jets are also considered as the backgrounds. Since the event selection requires multiple jets in the final state, ALPGEN generator is used. The generator is interfaced to HERWIG for parton shower and fragmentation, and also to JIMMY for the underlying event. The CTEQ6L1 [77] PDFs are used. The decay channels, $W \to \ell\nu$, $Z \to \ell^+\ell^-$, $Z \to \nu\nu$ ($\ell = e, \mu, \tau$), are all used in this analysis. The processes including the genuine E_T^{miss}, $W \to \ell\nu$, $Z \to \nu\nu$ are especially expected to remain after the event selection. The background samples are summarized in Table 5.5.
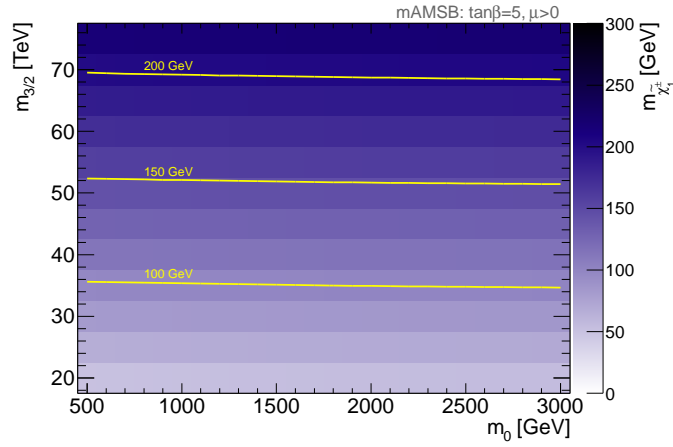
(a) $m_{\tilde{\chi}_1^\pm}$
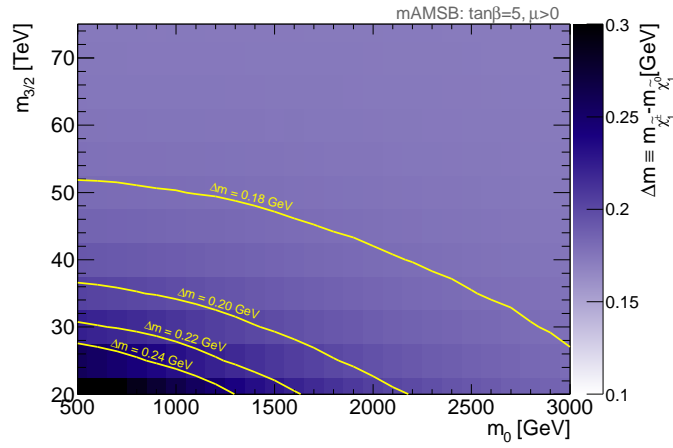
(b) $m_{\tilde{\chi}_1^\pm} - m_{\tilde{\chi}_1^0}$
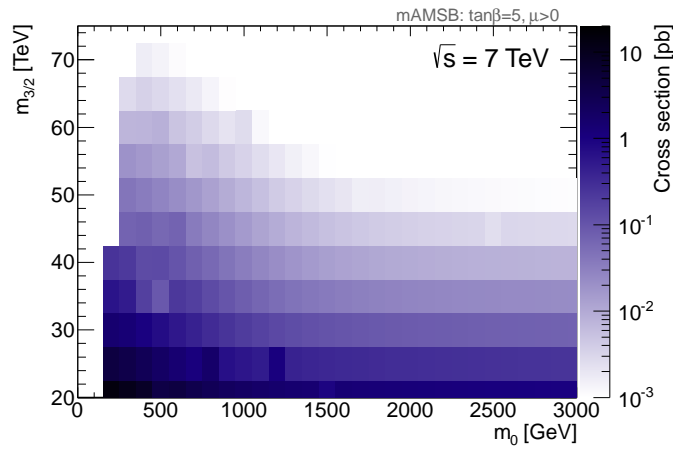
(c) cross-section

Figure 5.3: Various parameters of the AMSB models on the m_0-$m_{\frac{3}{2}}$ plane. (a), (b) and (c) show the $m_{\tilde{\chi}_1^\pm}$, $m_{\tilde{\chi}_1^\pm} - m_{\tilde{\chi}_1^0}$ and cross-section at $\sqrt{s} = 7$ TeV, respectively.

Table 5.5: Standard Model background Monte Carlo samples. The cross sections of LO values are shown for QCD jets, while NLO with NLL and NNLO values are given for $t\bar{t}$ and boson production processes respectively. $\hat{p}_T$ represents the transverse momentum of the two partons in the hard scattering process used in PYTHIA.

Physics process	Cross section $\times$ BR [pb]	MC generator
QCD Jets $8 \le \hat{p}_T < 17$ GeV	9.75×10^9	PYTHIA
QCD Jets $17 \le \hat{p}_T < 35$ GeV	6.73×10^8	PYTHIA
QCD Jets $35 \le \hat{p}_T < 70$ GeV	4.12×10^7	PYTHIA
QCD Jets $70 \le \hat{p}_T < 140$ GeV	2.19×10^6	PYTHIA
QCD Jets $140 \le \hat{p}_T < 280$ GeV	8.78×10^4	PYTHIA
QCD Jets $280 \le \hat{p}_T < 560$ GeV	2.33×10^3	PYTHIA
QCD Jets $560 \le \hat{p}_T < 1120$ GeV	33.8	PYTHIA
QCD Jets $1120 \le \hat{p}_T < 2240$ GeV	0.137	PYTHIA
QCD Jets $2240 \le \hat{p}_T$ GeV	6.28×10^{-6}	PYTHIA
$t\bar{t}$	160.8	MC@NLO
$W \to e\nu + N$ jets ($N = 0 - 5$)	1.04×10^4	ALPGEN
$W \to \mu\nu + N$ jets ($N = 0 - 5$)	1.04×10^4	ALPGEN
$W \to \tau\nu + N$ jets ($N = 0 - 5$)	1.04×10^4	ALPGEN
$Z \to \nu\nu + N$ jets ($N = 0 - 5$)	5.82×10^3	ALPGEN
$Z \to ee + N$ jets ($N = 0 - 5$)	1.07×10^3	ALPGEN
$Z \to \mu\mu + N$ jets ($N = 0 - 5$)	1.07×10^3	ALPGEN
$Z \to \tau\tau + N$ jets ($N = 0 - 5$)	1.07×10^3	ALPGEN

Chapter 6

Event Selection

6.1 Object Definition

The objects used in this analysis are defined as below:

- Track
  The tracks reconstructed in the inner detector used in this analysis are required to fulfill the following criteria:

  - $p_T^{track} > 0.4$ GeV,
  - $|d_0| < 1.5$mm,
  - $|z_0 \sin(\theta)| < 1.5$mm,
  - Number of pixel hits (N_{Pixel}) ≥ 1,
  - Number of SCT hits (N_{SCT}) ≥ 6.

  The definition of track parameters are described in Section 5.2.1. Figure 6.1 shows the distributions of track parameters after the application of these requirements. The chargino search relies on the reconstructed tracks in the inner detector; therefore, the reproducibility of the track qualities in the MC simulation is of importance to this analysis. The b-layer referred in Figure 6.1 is the innermost layer of the pixel detector. The details are mentioned in Section 2.2.3. The dataset obtained with jet triggers is compared to the QCD MC samples. They show the reasonable agreements.

- Jet
  Jets are reconstructed using anti-k_t algorithm with the distance parameter of $R = 0.4$ in Equation 5.2. The measurement of jet transverse momentum at the electromagnetic scale ($p_T^{\text{jet,EM}}$) underestimates that of hadron-level jets due to the nature of the non compensating calorimeters and the dead material. Thus, an average correction is applied to obtain the correct transverse momentum depending on η and $p_T^{\text{jet,EM}}$. The details of the jet calibration procedure is given in Ref. [78]. The acceptance cuts of $p_T > 20$ GeVand $|\eta| < 2.8$ are applied in this analysis.

- Electron
  Electrons are identified with *medium* selection criteria as described in Ref. [57]. The

(a) d_0

(b) $z_0 \sin \theta$

(c) $N_{\text{b-layer}}$

(d) N_{Pixel}

(e) N_{SCT}
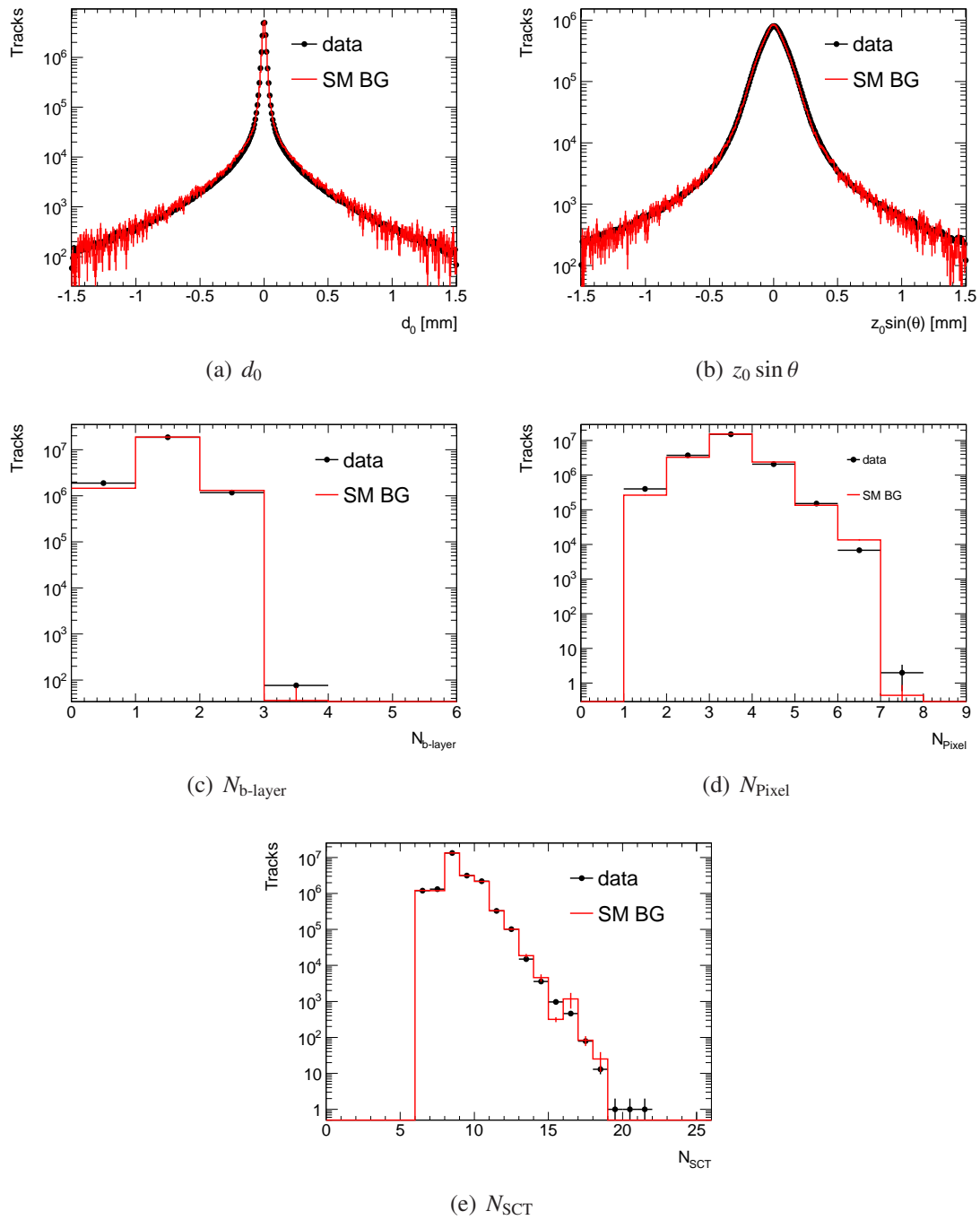
Figure 6.1: The distributions of track parameters. The black point show the data obtained with jet triggers while the red lines show the MC expectation with PYTHIA QCD samples.

variables used for the identification are summarized in Table 6.1. Electrons are required to fulfill the requirements of $E_T > 10$ GeV and $|\eta| < 2.47$.

Table 6.1: The definition of variables used in *medium* selection for electrons.

Acceptance	$|\eta| < 2.47$
Hadronic leakage	Ratio of E_T in the first layer of the hadronic calorimeter to E_T of the EM cluster
	Ratio of E_T in the hadronic calorimeter to E_T of the EM cluster
Middle layer of EM calorimeter	Ratio of the energy in 3×7 cells over the energy in 7×7 cells centered at the electron cluster position
	Lateral shower width, $\sqrt{(\sum E_i \eta_i^2)/(\sum E_i) - ((\sum E_i \eta)/(\sum E_i))^2}$, where E_i is the energy and η_i is the pseudorapidity of cell i and the sum is calculated within a window 3×5 cells.
Strip layer of EM calorimeter	Shower width is defined as $\sqrt{(\sum E_i(i - i_{max}))(\sum E_i)}$, where i runs over all strips in a window of $\Delta\eta \times \Delta\phi \sim 0.0625 \times 0.2$, corresponding typically to twenty strips in η, and i_{max} is the index of the highest-energy strip.
	Ratio of the energy difference between the largest and the second largest energy deposits in the cluster over the sum of these energies
Track quality	Number of hits in the pixel detector (≥ 1)
	Number of hits in the pixel and SCT detectors (≥ 7)
	Transverse impact parameter ($|d_0| < 5\text{mm}$)
Track-cluster matching	$\Delta\eta$ between the cluster position in the strip layer and the extrapolated track ($|\Delta\eta| < 0.01$)

- Muon
  Muons reconstructed with STACO algorithm are used in this analysis. Muons are required to be *Combined muons* or *Segment tagged muons*:*Combined muons* are muon candidates with a full track in the muon spectrometer and *Segment tagged muons* are reconstructed with a specific algorithm in order to recover efficiency in poorly covered regions and at low-transverse momenta. In addition, the selections requirements on the qualities of the ID tracks are also applied.

  - Number of b-layer hits > 0 if b-layer hits are expected.

  - Number of pixel hits plus number of crossed dead pixel sensors > 1.

  - Number of SCT hits plus number of crossed dead SCT sensors ≥ 6.

  - Number of pixel holes plus number of SCT holes < 3.

  - A successful TRT extension where expected (i.e. in the eta acceptance of the TRT). An unsuccessful extension corresponds to either no TRT hit associated, or a set of TRT hits associated as outliers:

    1. Require $N_{TRT}^{hits} + N_{TRT}^{outliers} > 5$ and $N_{TRT}^{outliers} < 0.9(N_{TRT}^{hits} + N_{TRT}^{outliers})$ for $|\eta| < 1.9$
    2. If $N_{TRT}^{hits} + N_{TRT}^{outliers} > 5$, then require $N_{TRT}^{outliers} < 0.9(N_{TRT}^{hits} + N_{TRT}^{outliers})$ for $|\eta| \geq 1.9$.

, where $N_{\text{TRT}}^{\text{hits}}$ and $N_{\text{TRT}}^{\text{outliers}}$ denote the number of TRT hits and the number of TRT outliers on the muon track, respectively.

Finally, the selection requirements of $p_{\text{T}} > 10$ GeV and $|\eta| < 2.4$ are applied.

- Missing transverse energy
  The missing transverse energy is calculated based on the transverse momenta of selected jets and lepton candidates described above, and all calorimeter clusters not associated to such objects.

6.1.1 Criteria for Resolving Object Overlapping

The defined physics objects overlap with each other, one o the overlapping objects is removed based on the following order:

1. If an electron and a jet are found within $\Delta R < 0.2$, both are classified as one electron and the jet is ignored.

2. If a muon and a jet are found within $\Delta R < 0.4$, both are classified as one jet and the muon is ignored.

3. If an electron and a jet are found within $0.2 \leq \Delta R < 0.4$, both are classified as one jet and the electron is ignored.

6.2 TRT Hits Association to a Track

As described in Section 4.1.2, the number of TRT hits in the outer modules ($N_{\text{TRT}}^{\text{outer}}$) in barrel region is used in order to identify charginos decaying in the TRT detector. The `ATLAS Extrapolator` tool is employed for the association of $N_{\text{TRT}}^{\text{outer}}$ to the track. The procedure of this association is visually explained in Figure 6.2.

The information of a track and the TRT hits are fed into the `ATLAS extrapolator`. The detector information is expressed as a `Surface`, which is each TRT layer. If the extrapolation succeeds, the `ATLAS Extrapolator` returns an expected track position on the `Surface`. Using the expected position , the distance between the track and the center of the drift tube ($d_{\text{track,tube}}$) is calculated. If $d_{\text{track,tube}}$ is less than the radius of drift tube (r_{tube}), the hits of the TRT drift tube is associated to the track.

6.3 Kinematic Selection Criteria

A small fraction of jets are reconstructed from the calorimeter noise or cosmic rays. All jets are required to pass the loose criteria of jet quality described in Ref.[78]. After the trigger decision and the jet cleaning, the selection requirements are applied on the event kinematics in order to suppress the SM background events. Selection criteria for the event kinematics are as follows:

1. Non-collision background rejection,
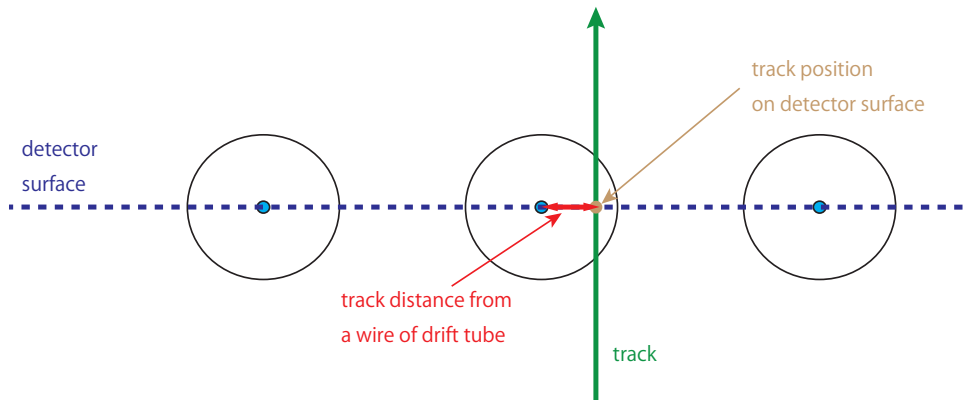
Figure 6.2: A sketch of the TRT hits association to track. The track position on a detector surface is calculated by the `ATLAS extrapolator`. If the track distance from a wire of drift tube is less than the radius of drift tube, the TRT hits is associated to the track.

2. Lepton veto: If there are one or more identified leptons (electrons or muons), the events is rejected,

3. $E_T^{miss} > 130$ GeV,

4. The leading jet p_T is larger than 130 GeV,

5. The second and third jet p_T are larger than 60 GeV.

   Figure 6.3 shows the distributions of E_T^{miss} and p_T of three highest-p_T jets. The distributions of the AMSB signal are also shown, and one can see that these kinematic selection requirements are reasonably suppress the background process and enhance the signal events. The event selection criteria and the data reductions are summarized in Table 6.2. The selection efficiencies of the AMSB signals are also given in the Table.

Table 6.2: Summary of kinematic selection cuts and data reduction. The selection efficiencies for each AMSB signal model are also shown.

Selection cut	Observed events	Signal efficiency [%]		
		LL01	LL02	LL03
Trigger	8855753	94.9	96.8	97.8
Jet cleaning	7141026	87.3	89.1	90.1
Lepton veto	6644394	72.8	72.5	72.6
Missing transverse momentum > 130 GeV	321412	66.5	68.2	69.6
First leading jet p_T > 130 GeV	276311	66.2	68.1	69.6
Second and third leading jet p_T > 60 GeV	73433	64.9	67.4	69.0

6.4   Selection Criteria for Chargino Candidate Track

Chargino tracks are expected to have high-p_T and well-isolated. In addition to the track definition described in Section 6.1, tighter selection requirements are applied on the tracks as follows:

96

(a) $E_{\mathrm{T}}^{\mathrm{miss}}$

(b) First leading p_{T} jet

(c) Second leading p_{T} jet

(d) Third leading p_{T} jet
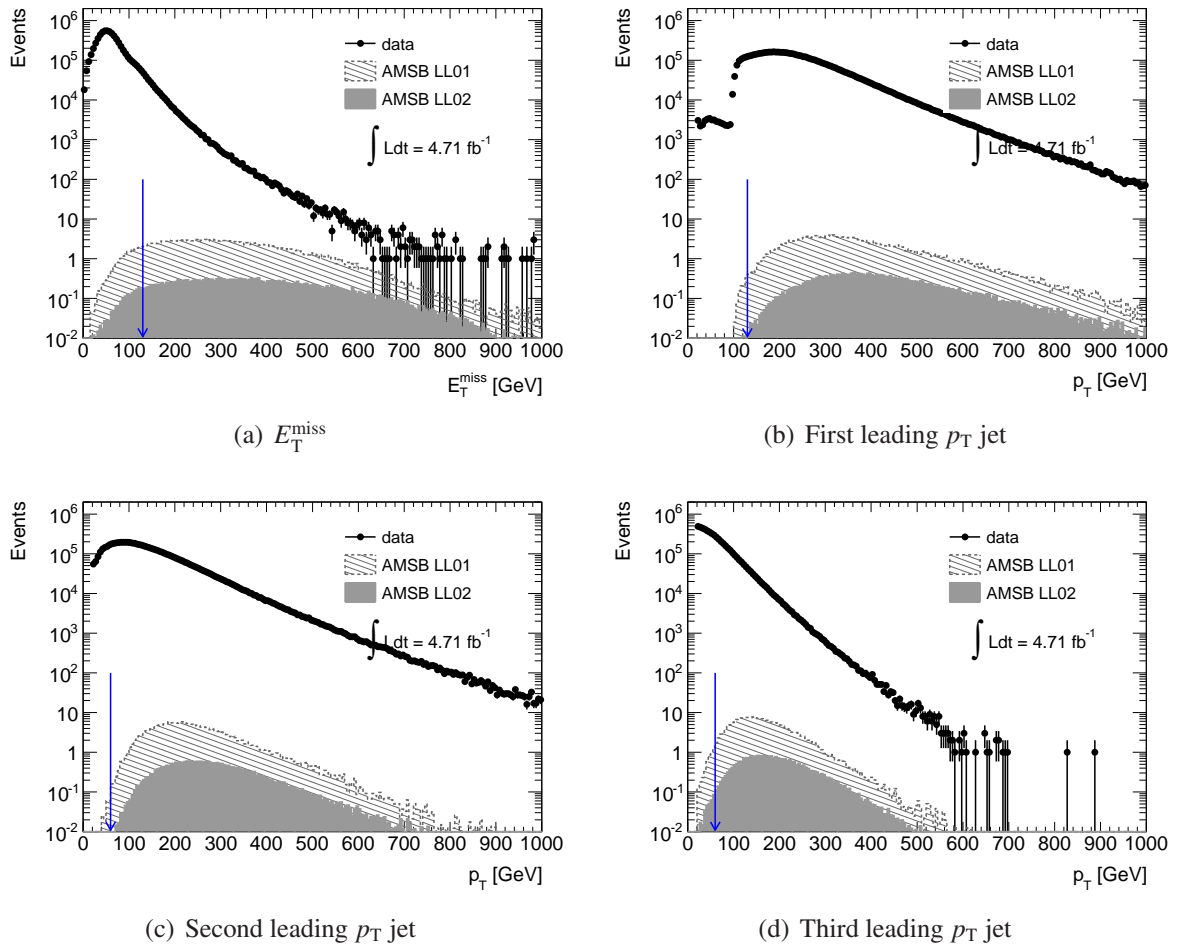
Figure 6.3: The $E_{\mathrm{T}}^{\mathrm{miss}}$ and jet p_{T} distributions after the lepton veto. The selection boundaries are indicated by arrows.

97
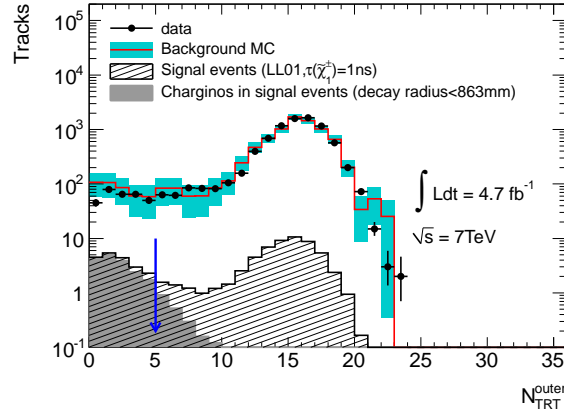
Figure 6.4: The $N_{\text{TRT}}^{\text{outer}}$ distributions for data and signal events (LL01, $\tau_{\tilde{\chi}_1^\pm} = 1$ ns). The signal events are shown by the hatched histogram with the high-p_{T} isolated track selection. In the signal events, the contribution of chargino tracks decayed before the TRT outer module ($r < 863$ mm) is indicated by the filled histogram. For these tracks, $N_{\text{TRT}}^{\text{outer}}$ is expected to have a value near zero. On the other hand, charged particles traversing the TRT typically have $N_{\text{TRT}}^{\text{outer}} \simeq 15$. The selection boundary is indicated by the arrow. The expectation from QCD multi-jet background MC events, normalized to the number of observed events, is also shown.

1. $N_{\text{Pixel}} \geq 1$ and the numbers of the b-layer hits $N_{\text{b-layer}} \geq 1$ if b-layer hits are expected,

2. $N_{\text{SCT}} \geq 6$,

3. There are no tracks as defined in Section 6.1 within $\Delta R < 0.1$,

4. The track is pointing to the TRT barrel layers and expected not to pass the inactive regions around $\eta = 0$,

5. A candidate track should have $p_{\text{T}}^{\text{track}} > 10$ GeV and the highest among isolated tracks in the event,

6. The number of the TRT hits in the outer module $N_{\text{TRT}}^{\text{outer}}$ is less than five.

The first three criteria are applied for ensuring good qualities of the reconstructed tracks. The fourth criterion selects tracks which go through all 73 layers of TRT detector in order to avoid misidentifying a track with a small $N_{\text{TRT}}^{\text{outer}}$ due to not penetrating all active layers. Figure 6.5 shows the sketch of acceptance selection. The red tracks are removed for not penetrating all active layers and the blue track are chosen by this criterion. The sixth criterion is the selection for the decaying track before the TRT outer module. $N_{\text{TRT}}^{\text{outer}}$ of the traversing the TRT gives about fifteen while $N_{\text{TRT}}^{\text{outer}}$ of decay before reaching the TRT outer module is expected to be nearly zero. As indicated in the arrow of Figure 6.4, $N_{\text{TRT}}^{\text{outer}} < 5$ is required.

A summary of track selection and data reduction is given in Table 6.3.
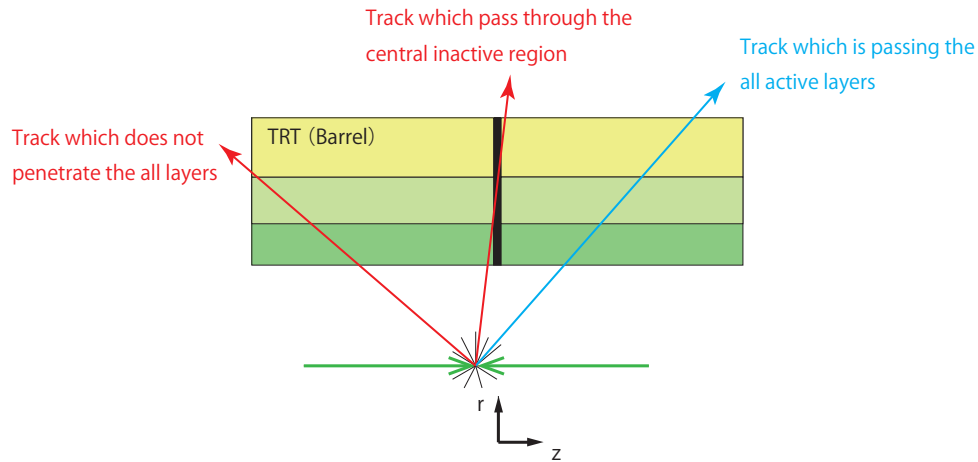
Figure 6.5: Acceptance cut for chargino track candidates. Only the tracks expected to penetrate the all active layers of the TRT detector are selected. Tracks which is passing inactive region at the center of the TRT or is not penetrating the all layers are rejected.

Table 6.3: Summary of selection requirements, the data reduction and the selection efficiencies of the AMSB signals. The purities of chargino tracks are also shown in parentheses.

Requirement	Observed events	Signal efficiency [%]		
		LL01	LL02	LL03
Kinematic selection (Section 6.3)	73433	64.9	67.4	69.0
High-p_T isolated track selection (Section 6.4, 1~5)	8458	24.8 (67.6)	26.2 (66.8)	27.2 (66.7)
Disappearing track selection (Section 6.4, 6)	304	6.1 (94.6)	6.6 (94.5)	7.3 (94.7)

6.5 Monte Calro Expectation

The expected breakdown of the background processes after all the high-p_T selection criteria is in Table 6.4. Most of events originate from high-p_T charged hadrons in jets and tau hadronic decays. Muons and electrons have a negligible contribution by applying the lepton veto and the disappearing track selection. The studies on the charged hadrons in jets or from hadronic decays of tau are investigated in the following section.

Table 6.4: The breakdown of the SM background process after applying the high-p_T isolated track selection criteria.

MC process	fraction (%)
QCD	66.3
W+Njets	10.7
Z+Njets	6.4
$t\bar{t}$	16.6

Chapter 7

Backgrounds

7.1 Category of Background Tracks

The selection criteria described in Section 6.3 are applied for the search for Long-lived charginos. There are two main background sources contributing to the events containing isolated high-p_T tracks after these selection requirements. Figure 7.1 shows origins of disappearing tracks.

1. High-p_T hadrons interacting with the materials of TRT detector.

2. Low-p_T charged particles whose p_T is badly reconstructed as high-p_T tracks due to scattering in the silicon detector.

The former and the latter are categorized as *interacting hadron track* and *badly reconstructed track*, respectively. High-p_T hadrons may cause interactions with the detector materials. The
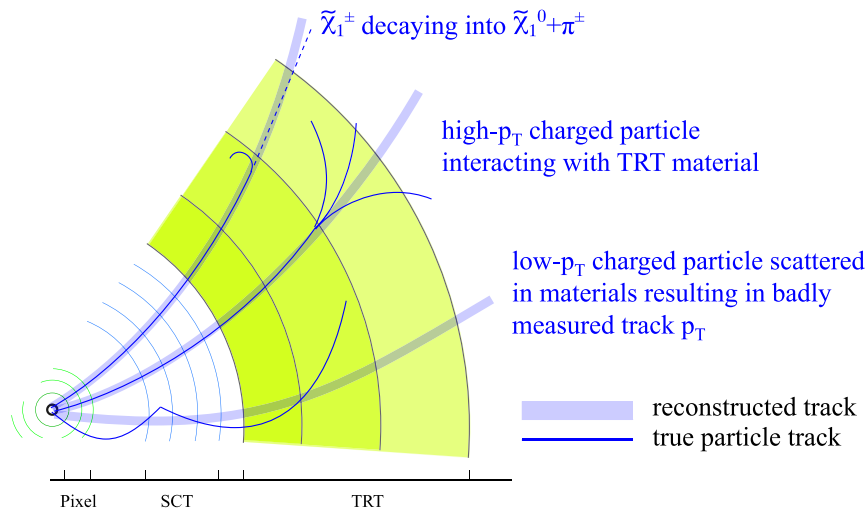
Figure 7.1: Origins of disappearing tracks.

corresponding particle can give a good track qualities but small number of hits in the TRT Type-3 module on the extrapolated track when an hadron interaction takes place in the TRT modules, especially in Type-1 or Type-2 modules.

A small fraction of low-p_T charged particles may be scattered with the detector materials of silicon detector. This particles may be reconstructed as nearly straight tracks which are high-p_T tracks. The badly reconstructed tracks can contribute to the background for disappearing tracks. The detail properties of badly reconstructed tracks are also given in Section 7.1.1.

The rate for the events containing these backgrounds are small, thus the background estimation using the Monte Carlo simulation may have the difficulty for the understandings of the background tracks. Therefore, this analysis adopts a fully data-driven techniques using the track p_T spectra of backgrounds in the control samples for the extraction of signal yield and the background estimation.

This chapter is dedicated for the studies on properties of these backgrounds.

7.1.1 Studies on Background Tracks

The studies on the properties of background tracks in this analysis is performed with Monte Carlo samples and real data of pp collisions.

Properties of Interacting Hadron Track

Figure 7.2 shows the display of a interacting hadron track. Many secondary particle can be seen from the point of the interaction with the TRT detector. In order to investigate the properties of
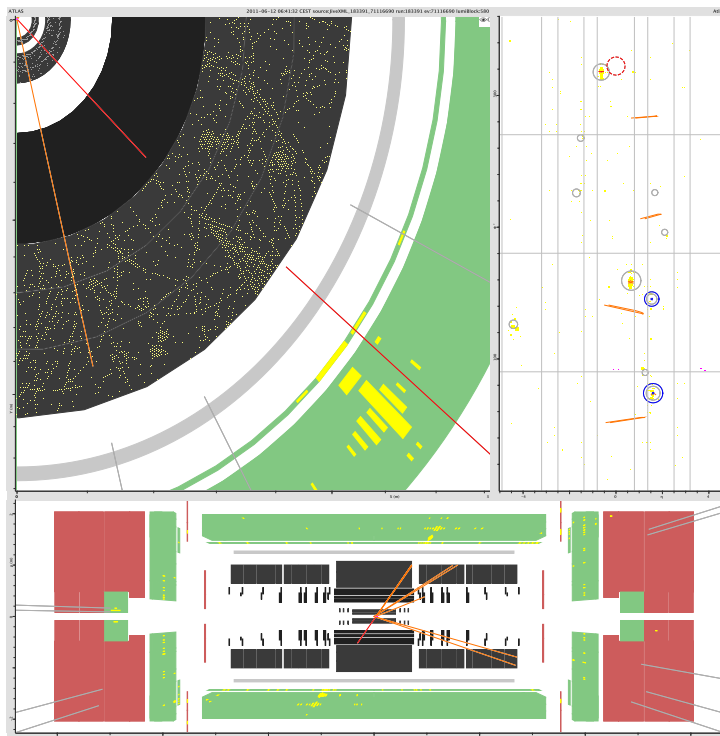
Figure 7.2: Example of a interacting hadron track. A high-p_T momentum track makes interaction with TRT detector material. From the point of the interaction in the detector, many of secondary particles is generated.

interacting hadron tracks, the single pion MC is employed. Figure 7.3 shows the breakdown of

pion tracks. Figure 7.3 (a) and (b) are the truth and the reconstructed p_T distributions, respectively. The inelastic interaction track is dominant and its rate has nearly no p_T-dependence in the p_T range above 10 GeV. The p_T spectrum of interacting hadron tracks is supported to be the same as that of non-interacting hadron tracks in this analysis. The p_T of charged particles are determined by the silicon detectors. Hence, p_T of the reconstructed track is not affected by the position of hadron interaction in the TRT detector. The reconstructed p_T spectrum of interacting hadron tracks is also supported to be the same as that of non-interacting hadron tracks.

(a) Truth p_T (b) Reconstructed p_T
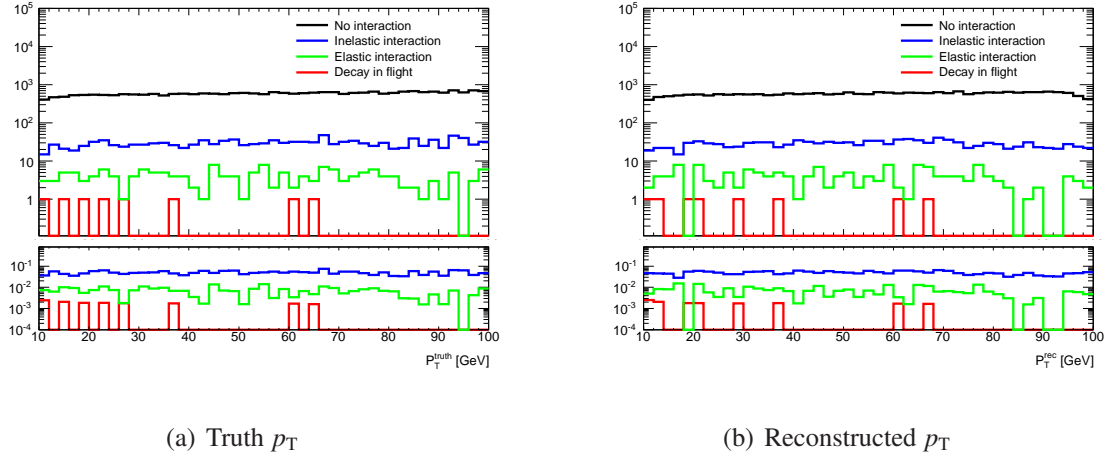
Figure 7.3: The breakdown of the interacting hadron tracks in the TRT detector. (a) and (b) show the truth and the reconstructed p_T distributions, respectively. The top figure shows p_T spectra of non-interacting charged pions, interacting elastically and inelastically, and decaying into $\mu + \nu$ in single charged pion MC events of a flat p_T distribution. The bottom figure shows the ratios with respect to the non-interacting.

Figure 7.4 shows the calorimeter activity $\sum_{\Delta R < 0.1} E_T^{clus}/p_T^{track}$, which is the sum of calorimeter cluster E_T fulfilling within $\Delta R < 0.1$ around the track over the p_T of the track. `TrackToCalo` tool is used for the calculation of ΔR. The interacting hadron track cluster around one, i.e. there are activities on calorimeter originating from actual hadrons. On the other hand, chargino gives values of nearly zero because neutralino from chargino decay does not make the activities on calorimeters and there is no actual particle.

From these studies, selection criteria listed below are required for extraction of the control sample of the interacting hadron tracks.

- Interacting hadron tracks depends on the kinematics, hence, the same kinematic selection criteria need to be required.

- The p_T spectra of interacting hadron tracks expected to be same as that of tracks with no interaction. For the extraction of the p_T spectrum of interacting hadron track, the non-interaction track is chosen by requiring many hits in the TRT Type-3 module.

- There are activities on calorimeter originating from actual hadrons on interacting hadron track; therefore, the calorimeter activities are required for extracting the the control sample of the interacting hadron track.
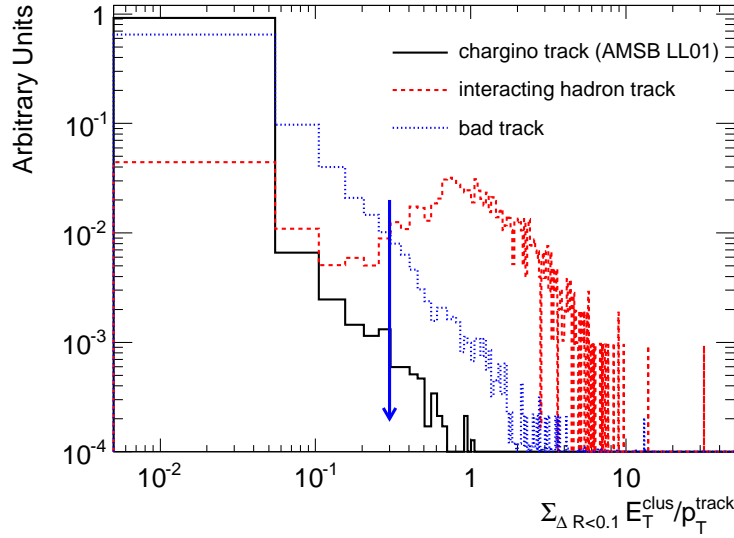
Figure 7.4: The $\sum_{\Delta R<0.1} E_{\mathrm{T}}^{\mathrm{clus}}/p_{\mathrm{T}}^{\mathrm{track}}$ distributions for chargino (solid line), high-p_{T} interacting hadron (dashed line) and bad tracks (dotted line) derived from MC events.

Properties of Badly Reconstructed Track

Figure 7.5 shows the p_{T} distribution of reconstructed tracks as a function of p_{T} of truth particle. Track p_{T} of particle with high momentum is reconstructed properly. However, some of particles with low momentum, typically less than a few GeV, are reconstructed as a high p_{T} track. When a low-p_{T} particle is reconstructed as a high-p_{T} track, the trajectory of the track does not reflects the true particle properly. Figure 7.6 shows the display of the badly reconstructed track. The corresponding track is shown as a red line. However, there are few corresponding TRT hits to the track because its track does not originate from a true particle. Thus, the badly reconstructed tracks could contribute to the background for the chargino search.

Isolated tracks in QCD MC events are used in order to investigate the properties of badly reconstructed track. Figure 7.7 shows the reconstructed momentum distributions for charged pions in the range of $0 < p_{\mathrm{T}}^{\mathrm{true}} < 5$ GeV with a variety of classifications for badly reconstructed track. The badly reconstructed track is here defined as that a track has no corresponding true charged particle, that is, large $\sigma(p_{\mathrm{T}})$, where $\sigma(p_{\mathrm{T}}) \equiv \frac{p_{\mathrm{T}}^{\mathrm{rec}} - p_{\mathrm{T}}^{\mathrm{true}}}{p_{\mathrm{T}}^{\mathrm{true}}}$ and $p_{\mathrm{T}}^{\mathrm{rec(true)}}$ is the reconstructed (true) transverse momentum. Actually, $\sigma(p_{\mathrm{T}}) > 5$ is required for tracks as the definition of badly reconstructed track.

- $\sigma(p_{\mathrm{T}}) > 5$ (No selection).

- $\sigma(p_{\mathrm{T}}) > 5$, $|d_0| < 1.5$mm and $|z_0\sin(\theta)| < 1.5$mm.

- $\sigma(p_{\mathrm{T}}) > 5$ and $|N_{\mathrm{SCT}}| \geq 6$.

- $\sigma(p_{\mathrm{T}}) > 5$ and $|N_{\mathrm{Pixel}}| \geq 1$.

When applying the cuts on the impact parameter, the distributions slightly differ from each other.
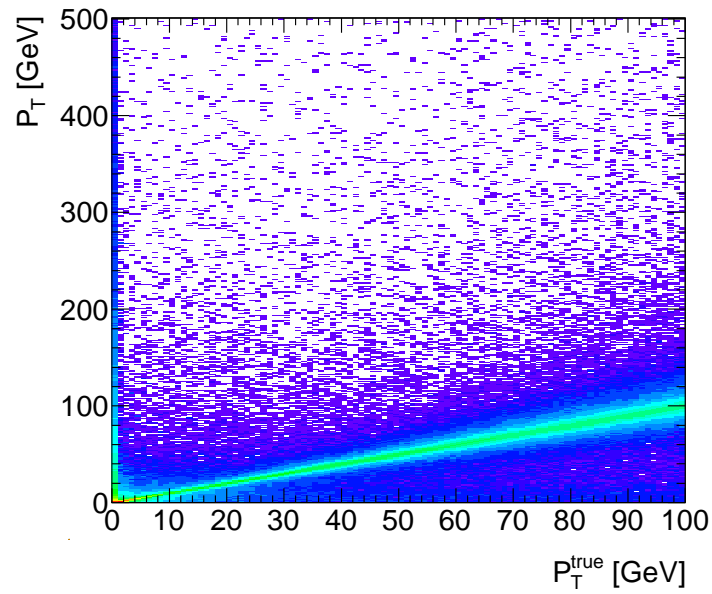
Figure 7.5: the p_T distribution of reconstructed tracks as a function of p_T^{true}.
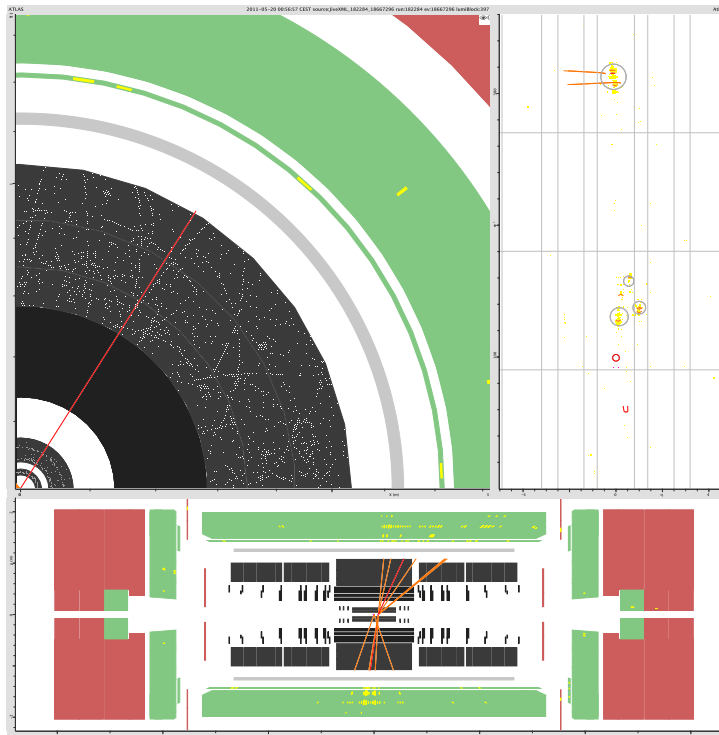
Figure 7.6: Event display of the badly reconstructed track candidate. The corresponding track is shown as a red line. There is continuous TRT hits of a low momentum particle near to the badly reconstructed track.
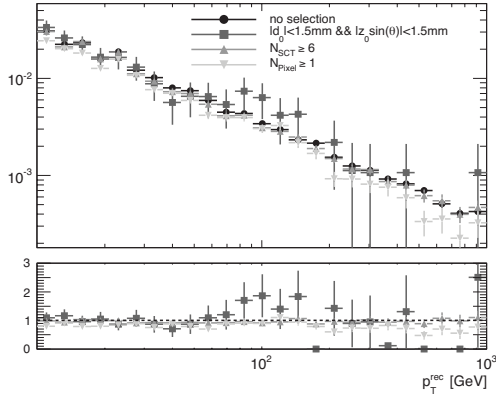
(a) $0 < p_T^{true} < 1$ GeV
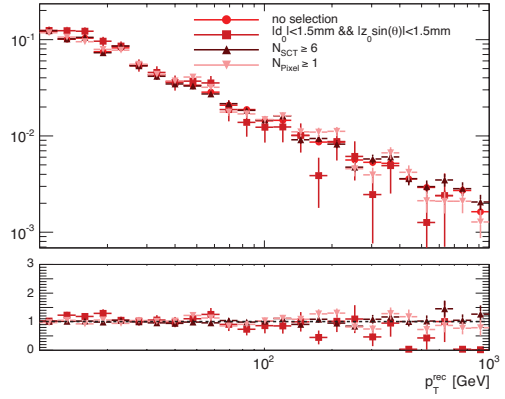
(b) $1 < p_T^{true} < 2$ GeV
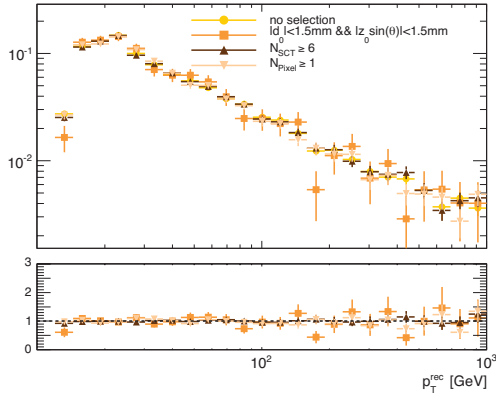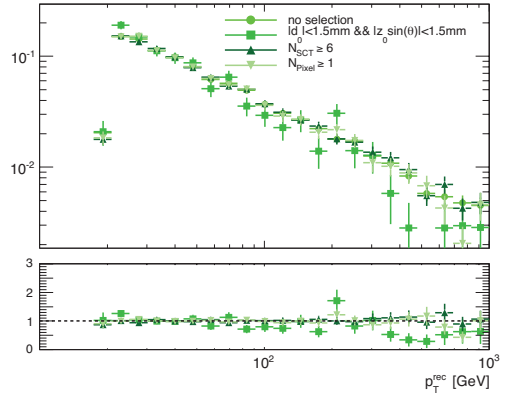
(c) $2 < p_T^{true} < 3$ GeV
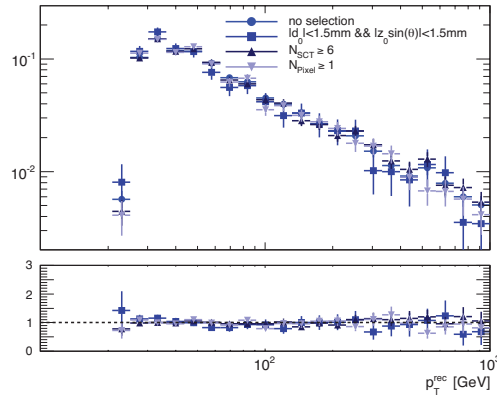
(d) $3 < p_T^{true} < 4$ GeV

(e) $4 < p_T^{true} < 5$ GeV

Figure 7.7: The p_T distribution of badly reconstructed tracks for (a) $0 < p_T^{true} < 1$ GeV , (b) $1 < p_T^{true} < 2$ GeV, (c) $2 < p_T^{true} < 3$ GeV, (d) $3 < p_T^{true} < 4$ GeV and (e) $4 < p_T^{true} < 5$ GeV. Each distribution is normalized to unity. The ratio of the distribution of each selection (see the text) to that of no selection is also shown at the bottom of each figure.

Figure 7.8 show the p_T distributions of badly reconstructed tracks for each p_T^{true} range. They show reasonable agreement in high-p_T region. The distributions of badly reconstructed track does not depend on the momenta of the truth particles. Therefore, the p_T distribution of badly reconstructed track does not depend on the kinematics.
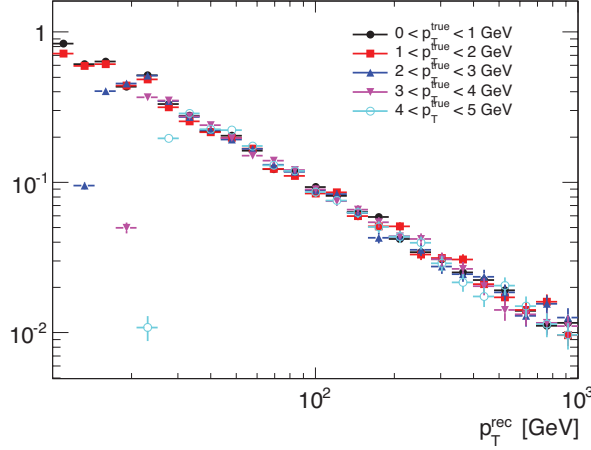
Figure 7.8: The p_T distribution of badly reconstructed tracks. The distributions are normalized by the number of tracks with p_T above 50 GeV.

Furthermore, the number of pixel hits N_{Pixel} of the badly reconstructed track is investigated. Figure 7.9 shows the N_{Pixel} distributions of correctly and badly reconstructed tracks. Correctly reconstructed track is defined as $|\sigma(p_T)| < 0.5$ while badly reconstructed track is defined as $\sigma(p_T) > 5$ or $\sigma(p_T) > 3$. The number of N_{Pixel} gives around three for correctly reconstructed tracks. On the other hand, a number of the badly reconstructed track is enhanced by requiring the small number of the N_{Pixel}. Moreover, the calorimeter activity of the badly reconstructed track is also investigated in Figure 7.4. The calorimeter activity of the badly reconstructed track gives nearly zero similarly to chargino tracks.

From the studies on the badly reconstructed track, the properties of the badly reconstructed tracks are;

- The p_T distribution of the badly reconstructed track does not depend on the kinematics.

- By requiring the small number of Pixel hits, the number of badly reconstructed tracks is enhanced.

- There are no associating calorimeter activity of the badly reconstructed track.

The selection criteria for extraction of two backgrounds from these studies are shown in the following section.

7.2 Control Regions for Background Tracks

The resulting selection criteria for high-p_T interacting hadron track and badly reconstructed track is summarized in Table 7.1.
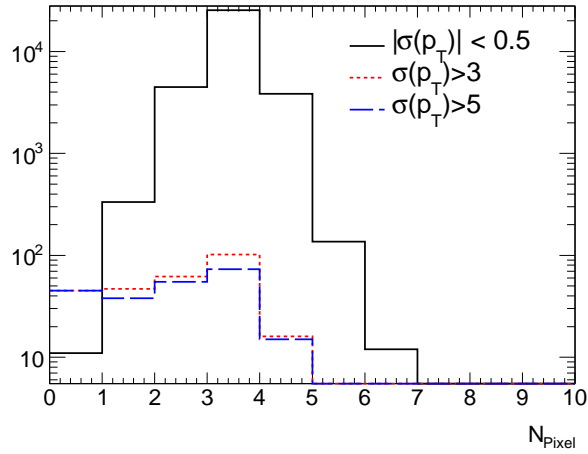
Figure 7.9: The N_{Pixel} distributions of correctly and badly reconstructed tracks in QCD MC events. Correctly reconstructed track is defined as $|\sigma(p_{\text{T}})| < 0.5$ while badly reconstructed track is defined as $\sigma(p_{\text{T}}) > 3$ or $\sigma(p_{\text{T}}) > 5$.

Table 7.1: Selection criteria for the control samples of interacting hadron track and badly reconstructed track.

	Kinematic selection	
	Interacting hadron track	Badly reconstructed track
Trigger	$E_{\text{T}}^{\text{miss}} > 75$ GeV & $p_T^{jet} > 55$ GeV	pre-scaled jet trigger
Leading p_T^{jet}	> 130 GeV	——
Leading second and third p_T^{jet}	> 60 GeV	——
Missing transverse energy	> 130 GeV	< 100 GeV
	Track quality	
Number of pixel hits	$N_{\text{pixel}} \geq 1$	$N_{\text{pixel}} = 0$
Number of Type-3 hits	$N_{\text{TRT}}^{\text{outer}} > 10$	$N_{\text{TRT3}}^{\text{outer}} < 5$
Calorimeter Activity	$\sum_{\Delta R < 0.1} E_T^{\text{clus}} / p_T^{\text{track}} \geq 0.3$	$\sum_{\Delta R < 0.1} E_T^{\text{clus}} / p_T^{\text{track}} < 0.3$

7.3 Extraction of Background Track Shapes

Figure 7.10 shows the p_T distributions in the control samples of interacting hadron tracks and the shape of the function derived by a maximum likelihood fit. The track p_T distribution falls steeply and has a long tail, which is "power low with exponential tail cutoff" like. This track p_T distribution is fitted by using a function,

$$f(x) = \frac{(1 + x)^{a_0}}{x^{a_1 + a_2 \ln(x)}}, \tag{7.1}$$

where x is p_T of tracks in the control samples of interacting hadron and $a_i(i = 0, 1, 2)$ are fit parameters. The fitted results and the covariance matrix results in:

$$a_i = \begin{pmatrix} 27.5 & \pm & 0.314 \\ 26.5 & \pm & 0.274 \\ 0.401 & \pm & 0.0226 \end{pmatrix} \tag{7.2}$$

$$\text{cov}(a_i, a_j) = \begin{pmatrix} & 0 & 1 & 2 \\ 0 & 0.09853 & 0.07422 & 0.003009 \\ 1 & 0.07422 & 0.07498 & -0.0005225 \\ 2 & 0.003009 & -0.0005225 & 0.00051 \end{pmatrix}. \tag{7.3}$$

The values of the correlation coefficient between parameters, ρ_{ij} are also given as

$$\rho_{ij} = \begin{pmatrix} & 0 & 1 & 2 \\ 0 & 1 & 0.864 & 0.424 \\ 1 & 0.864 & 1 & -0.0845 \\ 2 & 0.424 & -0.0845 & 1 \end{pmatrix}. \tag{7.4}$$

ρ_{ij} is defined as $\text{cov}(a_i, a_j)/\sigma_i \sigma_j$, where σ_i is the error on a_i.

The distribution of badly reconstructed tracks are shown in Figure 7.11. For the badly reconstructed tracks, the similar functional form is applied but an constant term is appended to the function in order to reproduce the long high-p_T tail as in Equation 7.5.

$$g(x) = \frac{(1 + x)^{b_0}}{x^{b_1 + b_2 \ln(x)}} + b_3, \tag{7.5}$$

where $x \equiv p_T^{track}$ and $b_i(i = 0, 1, 2, 3)$ are fit parameters. The obtained function by the fitting is also shown in Figure 7.11. The fitted parameters, the covariance matrix and the correlation coefficient are given as:

$$b_i = \begin{pmatrix} 83.2 & \pm & 0.356 \\ 79.5 & \pm & 0.325 \\ 0.487 & \pm & 0.0352 \\ 0.0336 & \pm & 3.21 \end{pmatrix}, \tag{7.6}$$

$$\text{cov}(b_i, b_j) = \begin{pmatrix} & 0 & 1 & 2 & 3 \\ 0 & 0.1267 & 0.08116 & 0.005561 & 0.02414 \\ 1 & 0.08116 & 0.1054 & -0.003554 & -0.008744 \\ 2 & 0.005561 & -0.003554 & 0.001239 & 0.004255 \\ 3 & 0.02414 & -0.008744 & 0.004255 & 10.29 \end{pmatrix}, \tag{7.7}$$
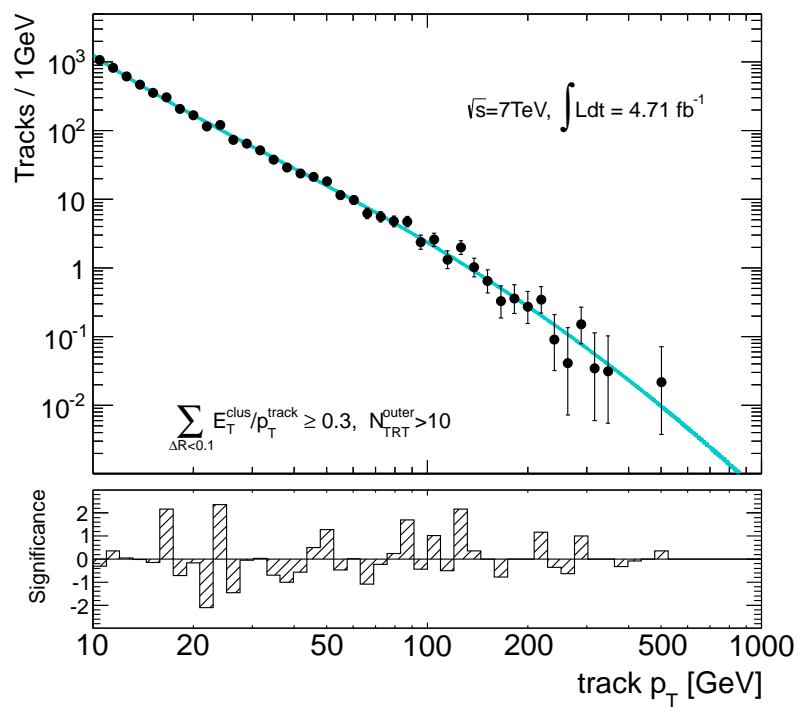
Figure 7.10: The top figure shows p_T distribution of interacting hadron track in the control sample. The data and the fitted line are shown by solid circles and a line, respectively. The bottom figure is the significance of the data-model difference on a bin-by-bin.

$$\rho_{ij} = \begin{pmatrix} & 0 & 1 & 2 & 3 \\ 0 & 1 & 0.702 & 0.444 & 0.0211 \\ 1 & 0.702 & 1 & -0.311 & -0.00840 \\ 2 & 0.444 & -0.311 & 1 & 0.0377 \\ 3 & 0.0211 & -0.00840 & 0.0377 & 1 \end{pmatrix}. \tag{7.8}$$
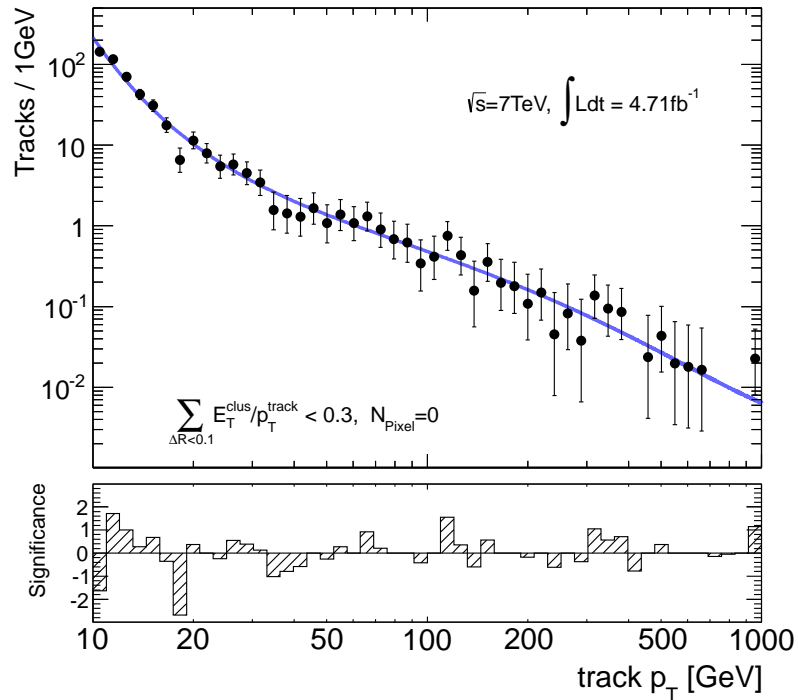
Figure 7.11: The top figure shows p_T distribution of badly reconstructed track control sample. The data and the fitted line are shown by solid circles and a line, respectively. The significance of the data-model difference on a bin-by-bin are also shown in the bottom.

Figure 7.12 shows the p_T distributions of badly reconstructed tracks with different number of the primary vertices N_{PV}. The significant difference cannot be seen with each other.
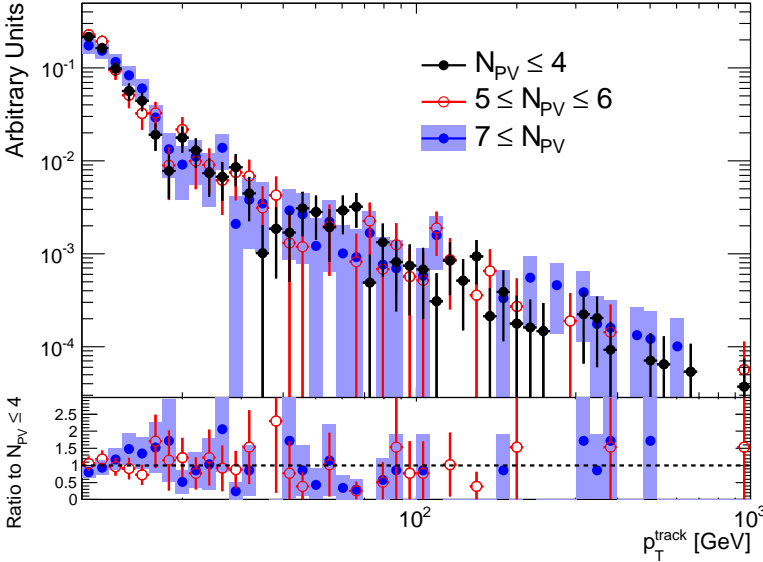
Figure 7.12: The p_T distributions of badly reconstructed tracks in events with various N_{PV}.

Chapter 8

Systematic Uncertainties

8.1 Systematic Uncertainties on Backgrounds

The normalizations for the two background components are free parameter in the fitting for signal extraction. The uncertainties on the background shapes are incorporated as nuisance parameters in the fitting. The covariance matrices in Section 7.3 are incorporated as uncertainties on the background shapes.

8.2 Systematic Uncertainties on Signal Normalization

The following items are the systematic uncertainties on the signal normalization to be considered in the fitting.

8.2.1 Uncertainty on the Theoretical Cross Section

Theoretical uncertainties on the signal cross section are evaluated by computing the changes in the cross section when the renormalization and factorization scales. For the estimation of uncertainty of the signal cross section, the uncertainties listed below are taken into account.

- Choice of parton distribution function (PDF).
  For the calculation, CTEQ6.6 [76] and MSTW2008 NLO [79] PDFs are employed.

- PDF errors.
  The uncertainty originating from PDF is evaluated by error sets of the PDF set.

- Uncertainty on strong coupling constant (α_s).
  The uncertainty of α_s arising from the scale of the strong coupling constant.

- Uncertainty on renormalization/factorization scale.
  The renormalization scale is the the scale which determines the strong coupling constant by the renormalization theory. The factorization scale is the scale which determines the strong coupling constant of short-distance interaction of partons.

The uncertainty on the cross section arising from the renormalization/factorization scale (μ)of the strong coupling constant $\alpha_s(\mu)$ is estimated by varying the scale μ with factors of 0.5 or 2.

A total uncertainty on the cross section for LL01 model results in 27.2% by taking the maximum difference between 68% confidence level upper and lower limits on the cross sections calculated using CTEQ6.6 and MSTW2008 NLO PDFs. The resulting uncertainties on the cross section for the other models are also summarized in the Table 8.2.1. The dominant component of the uncertainty comes from PDF errors. The second component originates from the uncertainty on the renormalization/factorization scale.

Table 8.1: The uncertainties on the theoretical cross section of the AMSB signals.

Signal	LL01	LL02	LL03
Uncertainty	±27.2 %	±36.7 %	±47.1 %

8.2.2   Uncertainty on the Jet Energy Scale

Jets are reconstructed at the electromagnetic scale, which is the basic signal scale for calorimeters. This energy scale is established using test-beam measurements. The jet energy is scaled in order to correct the energy and momentum of the jets measured in the calorimeter to those of the jet at the hadronic scale. this uncertainty is estimated according to Ref.[80]. The contributions to the jet energy scale systematics are following.

- Uncertainty from the jet energy scale calibration method
  There are any deviation in transverse momentum and energy response after calibration of the jet energy scale to the nominal MC. This is due to the assumption that every constituent needs the same average compensation when deriving the calibration constants or the same correction factor used for transverse momentum and energy of jets.

- Uncertainty from the calorimeter response
  The response of single particles interacting in calorimeters is used to derive the uncertainty on jet energy scale. The uncertainty of the calorimeter response to a jet is obtained from the uncertainty of the individual particles constituting the jet.

- Uncertainty from the detector simulation
  The uncertainty is arising from thresholds of calorimeter cell noise or the additional detector material.

- Uncertainty from the the physics model and parameters employed in the MC
  The contributions from the modeling of the fragmentation and underlying event of the MC are obtained by comparison of the several MC.

For each p_T, η bin, the contributions from these uncertainties are added in quadrature. The uncertainty arising from jet energy scale affects the overall normalization. The uncertainty on missing transverse energy due to the jet energy scale is also taken into account. Figure 8.1 shows the distributions of E_T^{miss} and the first leading jet p_T distributions of signal sample after kinematic selections with the nominal value and $\pm\sigma$ variations. The resulting uncertainty is estimated to be 2.8%.

(a) $E_{\mathrm{T}}^{\mathrm{miss}}$

(b) the first leading jet p_{T}
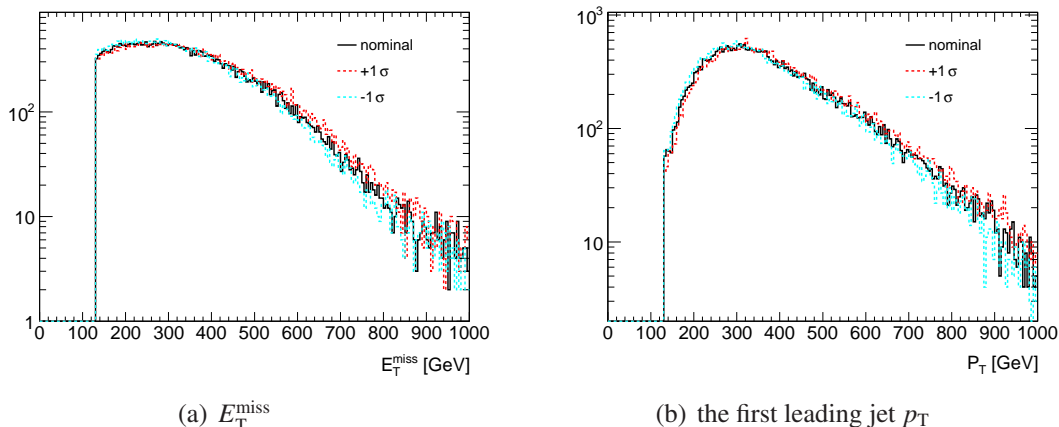
Figure 8.1: The distributions of $E_{\mathrm{T}}^{\mathrm{miss}}$ and the first leading jet p_{T} distributions of signal sample after kinematic selections with the nominal value and $\pm\sigma$ variations. The black, red and blue shows the nominal value, $+1\sigma$ and -1σ variations, respectively.

8.2.3 Uncertainty on the Track Reconstruction Efficiency

The modeling of the Inner Detector materials changes reconstruction efficiency of tracks. The uncertainty on reconstruction efficiency is arising from the modeling of materials. The uncertainty is estimated in the Ref.[81, 82].

The overwhelming majority of particles used for the estimation is hadrons. A good description of the materials in the detector is needed for determining the reconstruction efficiency. In order to estimate the uncertainty of the reconstruction efficiency, two different data-driven methods are used. The first method reconstructs the invariant mass of K_S^0 mesons decaying into two charged pions. The second method compares the track lengths in the data and simulation. The first method studies the mass as a function of the decay radius of the K_S^0 meson. This method has sensitivity to small radii. The second method probes the material description in the simulation in terms of the interaction length in the SCT. The combination of both methods provides good sensitivity throughout the silicon detectors. The uncertainty on the reconstruction efficiency in the barrel region is estimated to be 2.0% in the barrel region.

8.2.4 Uncertainty on the Integrated Luminosity

The uncertainty on the integrated luminosity is investigated in Ref.[83, 84]. There are some of uncertainties on the integrated luminosity.

- *vdM* Scan Calibration
  As mentioned in Appendix A, the *vdM* scan is employed for the luminosity determination. The uncertainty of the *vdM* Scan is the dominant uncertainty in the luminosity calibration.

- Afterglow Correction
  The luminosity detectors observe some small activities in the BCISs immediately following a collision. With a 2011 bunch spacing of 50ns and a relatively large number of bunches, this afterglow tends to reach a stable equilibrium after the first few bunches in

115

a train, and is observed to scale the instantaneous luminosity. The effect of the afterglow is taken into account for the luminosity determination. The uncertainty of the afterglow correction is also considered.

- Long-term Stability
  One source of potential uncertainty is the assumption that σ_{vis} determined by the *vdM* scans is stable in the entire 2011 runs. Several effects could degrade the long-term stability of a detector.

- μ Dependence
  The dependency of the average numbers of interactions per bunch crossing μ is also assessed.

The uncertainty on the integrated luminosity is estimated by employing the data with low μ. The uncertainty is larger for the last part of the 2011 data due to the increasing pile-up. The resulting uncertainty is estimated to be $\pm 3.9\%$.

8.2.5 Uncertainty on the Pile-up Modeling

The uncertainty arising from the pile-up modeling in the simulation is evaluated by comparing the difference of acceptance of the signal sample with the nominal value of average number of pile-up interaction $\langle \mu \rangle$ to one with the different value of $\langle \mu \rangle$. The sample with a different $\langle \mu \rangle$ are obtained by re-weighting a factor of 0.9 on $\langle \mu \rangle$.

8.2.6 Uncertainty on the Trigger Efficiency

The measured trigger efficiencies for data and MC events as a function of $E_{\mathrm{T}}^{\mathrm{miss}}$ are shown in Figure 8.2. Their turn-on curves are parametrized by the fit with a function,

$$\varepsilon(E_{\mathrm{T}}^{\mathrm{miss}}) = \frac{1}{2}\left(1 + \mathrm{erf}\left(\frac{E_{\mathrm{T}}^{\mathrm{miss}} - t}{\sqrt{2}\sigma}\right)\right), \tag{8.1}$$

where t and σ are the threshold and resolution parameters. By varying t and σ within their fit uncertainties and taking the difference between data and MC events, the uncertainty on the trigger efficiency is evaluated. The resulting uncertainty is quoted as $\pm 2.3\%$.

Summary

Contributions of each systematic uncertainty in signal expectations are summarized in Table 8.2.6. In total, an uncertainty of $\pm 27.8\%$ is quoted on the signal normalization.
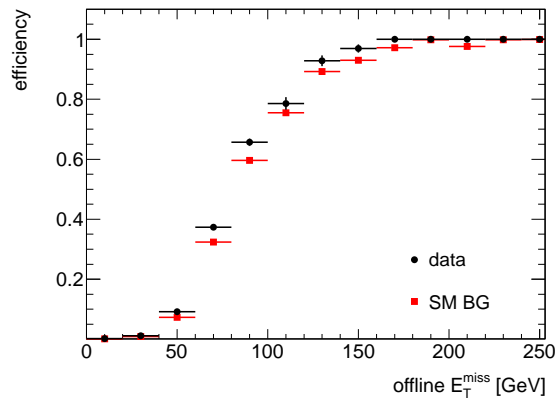
Figure 8.2: Trigger efficiencies for data and MC events as a function of $E_{\mathrm{T}}^{\mathrm{miss}}$

Table 8.2: Summary of systematic uncertainties in the signal normalization.

Source	Uncertainty
Theoretical cross section	±27.2 %
Jet energy scale	±2.8 %
Track reconstruction efficiency	±2.0 %
Luminosity	±3.9 %
Pile-up modeling	±0.5 %
Trigger efficiency	±2.3 %
Total	±27.8 %

Chapter 9

Background Estimation and Signal Extraction

9.1 Estimation of Background and Signal Yields

For the estimation of background and the extraction of signal yield, a simultaneous fit on the track p_T is performed. The p_T shapes of the two background components derived using their control samples, as described in Section 7.1 are used in the fit. The p_T shape of the signal is fully based on the MC prediction with the application of all the selection requirements. The following sections describe the details of the fit procedure.

9.1.1 Unbinned Maximum Likelihood Fit

A statistical test is performed in order to evaluate how well the observed data agree with a given signal model. A likelihood function is employed as the estimator for the statistical test and the unbinned maximum likelihood is performed. In this analysis, p_T spectra of the signal and the background tracks are used; they give a discrimination of signal events to the background, as shown in Figure 9.1. The effects of systematic uncertainties are incorporated via constraint terns on nuisance parameters; the overall normalization of the signal and the parameters describing the background track p_T shapes are set as nuisance parameters.

Using track p_T spectra, the resulting likelihood function, $\mathcal{L}$, is given as

$$\mathcal{L} = \prod^{n_{obs}} \mathcal{L}(p_T; \mu, n_b, \alpha, \vec{\beta}), \tag{9.1}$$

$$\mathcal{L}(p_T; \mu, n_b, \alpha, \vec{\beta}) = \frac{\mu n_s^{exp}}{n_b + \mu n_s^{exp}} \mathcal{L}_s(p_T; \mu, \alpha) + \frac{n_b}{n_b + \mu n_s^{exp}} \mathcal{L}_b(p_T; \vec{\beta}_{bad}, \vec{\beta}_{had}), \tag{9.2}$$

$$n_s^{exp} = L\sigma_s\varepsilon_s(1 + \alpha), \tag{9.3}$$

$$\mathcal{L}_b(p_T; \vec{\beta}_{bad}, \vec{\beta}_{had}) = f_{bad}\mathcal{L}_{bad}(p_T; \vec{\beta}_{bad}) + (1 - f_{bad})\mathcal{L}_{had}(p_T; \vec{\beta}_{had}), \tag{9.4}$$

where

$$
\begin{array}{rcl}
\mu & : & \text{signal strength,} \\
n_{\text{obs}} & : & \text{the observed number of events,} \\
n_{\text{s}}^{\text{exp}} & : & \text{the expected number of signal events for a given signal model,} \\
n_{\text{b}} & : & \text{the number of background events,} \\
L & : & \text{the integrated luminosity,} \\
\sigma_{\text{s}} & : & \text{the signal cross section,} \\
\epsilon_{\text{s}} & : & \text{the signal selection efficiency,} \\
f_{\text{bad}} & : & \text{the fraction of badly reconstructed tracks in the background,} \\
\alpha & : & \text{the nuisance parameter representing the overall normalization of} \\
& & \text{the signal yield,} \\
\vec{\beta}_{\text{bad}} & : & \text{the nuisance parameters representing the } p_{\text{T}} \text{ spectrum of the badly} \\
& & \text{reconstructed tracks,} \\
\vec{\beta}_{\text{had}} & : & \text{the nuisance parameters representing the } p_{\text{T}} \text{ spectrum of the in-} \\
& & \text{teracted hadron tracks.}
\end{array}
$$

The likelihood functions of $\mathcal{L}_s$, $\mathcal{L}_{bad}$ and $\mathcal{L}_{had}$ in Equations 9.1 and 9.4 are given by incorporating the effects of the systematic uncertainties as

$$
\mathcal{L}_s(p_{\text{T}}; \alpha) = \mathcal{F}_s(p_{\text{T}})\mathcal{N}(\alpha; \Delta_{norm}), \tag{9.5}
$$

$$
\mathcal{L}_{bad}(p_{\text{T}}; \vec{\beta}_{bad}) = \mathcal{F}_{bad}(p_{\text{T}}; \vec{\beta}_{bad})\mathcal{M}(\vec{\beta}_{bad}; \vec{C}_{bad}), \tag{9.6}
$$

$$
\mathcal{L}_{had}(p_{\text{T}}; \vec{\beta}_{had}) = \mathcal{F}_{had}(p_{\text{T}}; \vec{\beta}_{had})\mathcal{M}(\vec{\beta}_{had}; \vec{C}_{had}), \tag{9.7}
$$

where

$$
\begin{array}{rcl}
\mathcal{F}_s & : & \text{the normalized probability density function derived from signal} \\
& & \text{Monte Carlo samples,} \\
\Delta_{norm} & : & \text{the systematic uncertainty of the signal normalization,} \\
\mathcal{N} & : & \text{the normal distribution,} \\
\mathcal{F}_{bad} & : & \text{the normalized probability density function derived from the con-} \\
& & \text{trol samples of badly reconstructed tracks,} \\
\mathcal{F}_{had} & : & \text{the normalized probability density function derived from the con-} \\
& & \text{trol samples of interacting hadron tracks,} \\
\mathcal{M}_{had} & : & \text{the multivariate normal distribution,} \\
C_{bad} & : & \text{the covariance matrix of the normalized probability density func-} \\
& & \text{tion of badly reconstructed tracks,} \\
C_{had} & : & \text{the covariance matrix of the normalized probability density func-} \\
& & \text{tion of interacting hadron tracks.}
\end{array}
$$

The hypothesis test uses the profile likelihood ratio [85] to compare two hypothesis of 'background-only' and 'signal+background' models.

9.2   Fit results

Figures 9.2 (a) and (b) show the p_{T} distributions of candidate tracks with the best-fit spectra derived by the 'signal + background' and 'background only' fits, respectively. By the 'signal + background' fitting, the signal strength of LL01 model results in less than 0.048 at 68%CL,

119
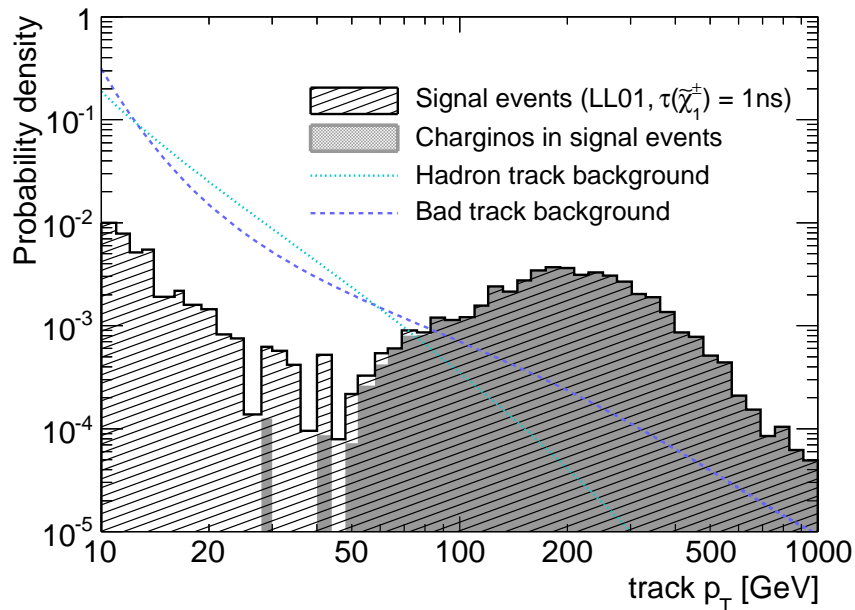
Figure 9.1: Probability density functions employed for the background estimation and the signal extraction. The dotted line is the shape of the p_T distribution in the control sample of the interacting hadron tracks. The dashed line is the shape of the badly reconstructed tracks. The hatched histogram is the p_T distribution of the signal Monte Carlo (LL01).

i.e. no excess of data observed and expected number of background events is 303.9 ± 16.7. The observed p_T spectra is consistent with the background-only hypothesis. f_{bad} is nearly zero as expected. Furthermore, the results with 'background only' fits are also consistent with that of the 'signal + background' fits. The resulting values of the fit parameters are summarized in Table 9.1.

Table 9.1: Summary of the fit

	signal(LL01)+background	background only
Signal strength	<0.048 (68% CL)	—
Number of background events	303.9 ± 16.7	304.0 ± 16.9
Fraction of bad tracks	$1.5 \times 10^{-6} \pm 1.7 \times 10^{-1}$	$2.2 \times 10^{-8} \pm 1.4 \times 10^{-1}$
p-value of null hypothesis	—	0.50

9.3 Validation

Various of validations for the fitting and the background estimation are performed.
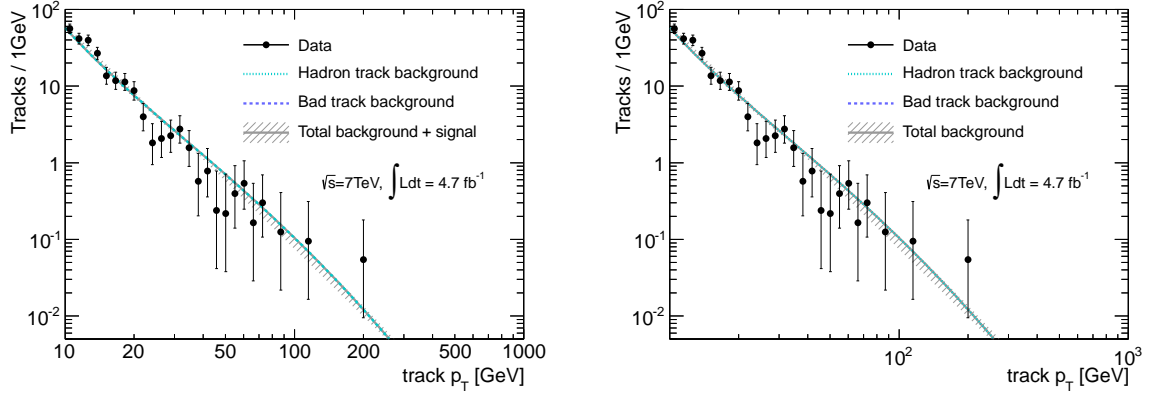
(a) signal+background fit
(b) background-only fit

Figure 9.2: The p_T distribution of candidate tracks with the best-fit shape of the 'signal + background' and 'background only' model. The signal point of LL01 and $\tau_{\tilde{\chi}_1^\pm} = 1$ ns are used, but the best-fit signal contribution is found to be zero.

9.3.1 The Background Shape with Alternative Functions

In order to assess any possible biases on the fit result due to the choice of the functional form especially for the hadron background tracks, the fit results with alternative functions are compared. The shapes of interacting hadron tracks are derived by adopting the following functional forms that are expected to reasonably describe the data:

$$f(x) = \frac{a_0(1 + x)^{a_1}}{x^{a_2 + a_3 \ln x}}, \tag{9.8}$$

$$f_1(x) = \frac{a_0(a_1 + x)^{a_2}}{x^{a_3 + a_4 \ln(x)}}, \tag{9.9}$$

$$f_2(x) = \frac{a_0}{(a_1 + a_2 x + a_3 x^2)}, \tag{9.10}$$

$$f_3(x) = \frac{a_0}{(a_1 + a_2 x + a_3 x^2)^{a_4}}, \tag{9.11}$$

$$f_4(x) = \frac{a_0}{(a_1 + a_2 x + a_3 x^2 + a_4 x^3)^{a_5}}, \tag{9.12}$$

$$f_5(x) = \frac{a_0 \exp(-x/a_1)}{(a_2 + x)^{a_3}}. \tag{9.13}$$

The best-fit shapes of each functional form and the resulting χ^2 values of the fit are shown in Figure 9.3 and Table 9.2. In the figure, the distributions are normalized to unity. They shows an agreement comparatively with each other down to the fourth order of magnitude. The choice of the functional form for the background tracks has a negligible impact on the final results.

9.3.2 Validation of the Signal Extraction Method

A closure test is performed based on an ensemble of pseudo-experiments of observing three hundred and four events with various values of fit parameters. This pseudo-experiments are

Function	χ^2
$f(x)$	47.00
$f_1(x)$	44.41
$f_2(x)$	89.54
$f_3(x)$	67.08
$f_4(x)$	67.08
$f_5(x)$	66.04

Table 9.2: Corresponding χ^2 values for the interacting hadron track.
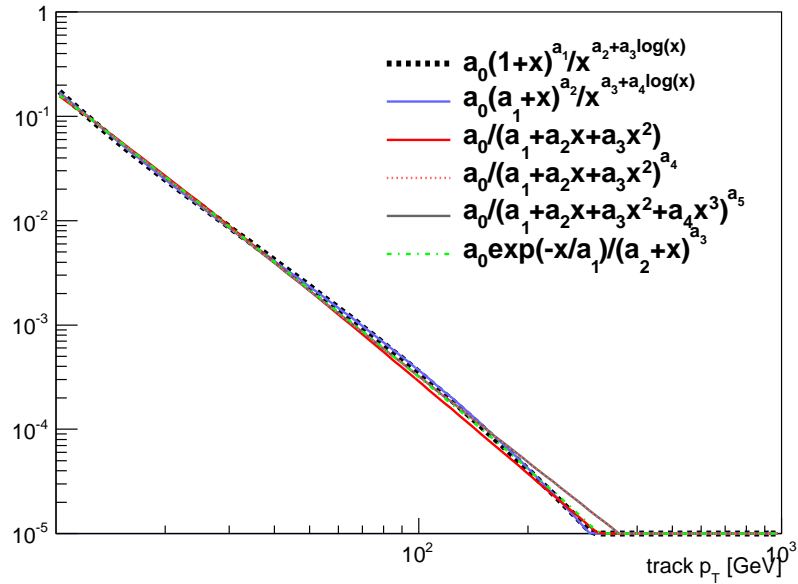
Figure 9.3: Best-fit form of alternative functions for interacting hadron track shape.

performed on the assumption of the appearance of signal events. Figures 9.4 and 9.5 show fitted values of f_{bad} and μ as a function of the value used as input ($f_{bad}^{(true)}$). In addition, Figures 9.4 (c) and 9.5 (c) show $f_{bad}^{(fitted)} - f_{bad}^{(true)}$ distributions with the pseudo-experiments without and with signals, respectively.

The signal strength obtained by the pseudo-experiments injecting the LL01 signal results in around one for difference $f_{bad}^{(true)}$. The fitted value $f_{bad}^{(fitted)}$ is also correctly estimated for $f_{bad}^{(true)}$ with the deviation $\sigma(f_{bad}) \sim 0.2$. Hence, if the signals are in the observed data, this data-driven method works properly. On the other hand, the signal strength obtained by the pseudo-experiments without signals results in around zero for any $f_{bad}^{(true)}$. The fitted value $f_{bad}^{(fitted)}$ obtained by the pseudo-experiments is also correctly estimated. Therefore, even if the signal is absent in the observed data, this method estimates the number of signals and the fraction of the badly reconstructed tracks.

9.3.3 Distributions of Candidate Tracks

After all the selection cuts are applied, 304 events containing a high-p_{T} isolated track candidates are remained in the entire data. Figures 9.6 (a) and (b) are the distributions of the number of hits in the TRT inner and middle modules for candidate tracks. The background expectations of interacting hadron tracks and badly reconstructed tracks are derived from control samples and normalized to the observed number of candidate tracks. $N_{\mathrm{TRT}}^{\mathrm{inner}}$ and $N_{\mathrm{TRT}}^{\mathrm{middle}}$ of badly reconstructed tracks is small because this track does not originate from a actual particle. On the other hand, $N_{\mathrm{TRT}}^{\mathrm{inner}}$ and $N_{\mathrm{TRT}}^{\mathrm{middle}}$ of interacting hadron tracks, which are associates to true charged particle, becomes large.

The observed tracks follows the distributions of the interacting hadron tracks. This is consistent with the result of the estimation that the interacting hadron tracks are dominant background as expected.
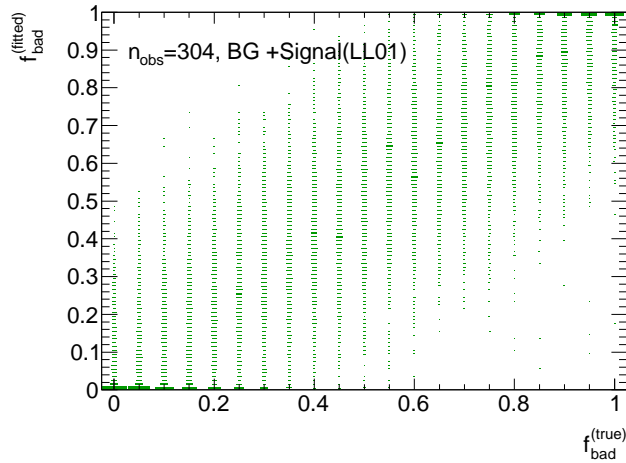
(a) f_{bad}^{fitted} vs. f_{bad}^{true}
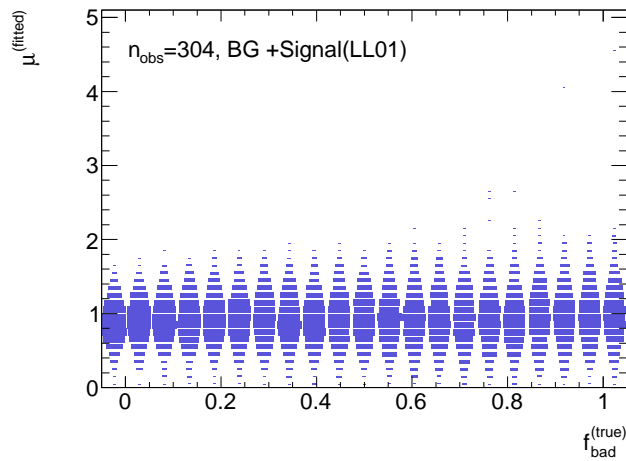
(b) μ^{fitted} vs. f_{bad}^{true}
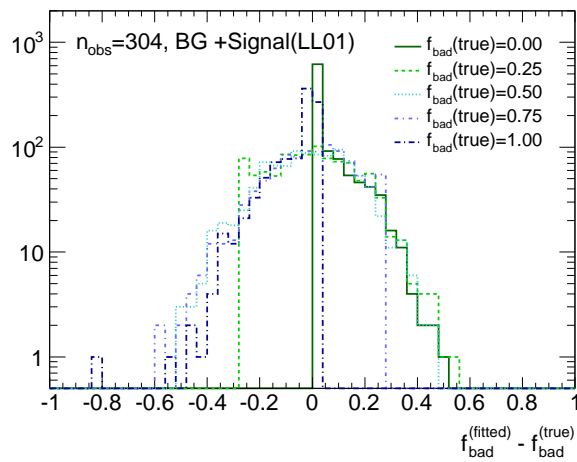
(c) $f_{bad}^{fitted} - f_{bad}^{true}$

Figure 9.4: The fitted parameters of f_{bad} (a) and μ (b) as a function of true f_{bad} derived from pseudo-experiments observing 304 events including signals (LL01). The pull distributions of f_{bad} (c) for various true values are also shown.
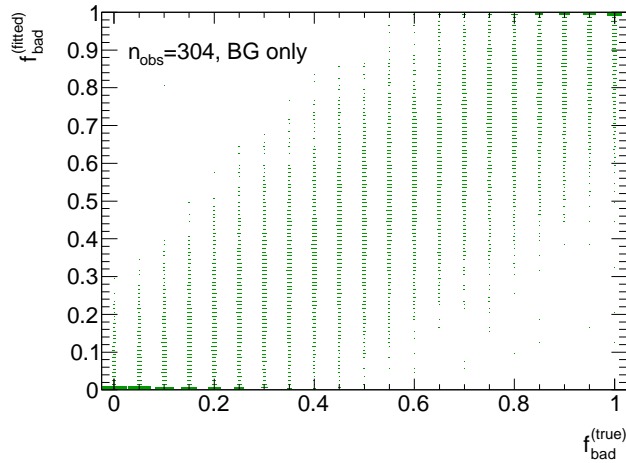
(a) $f_{\mathrm{bad}}^{\mathrm{fitted}}$ vs. $f_{\mathrm{bad}}^{\mathrm{true}}$
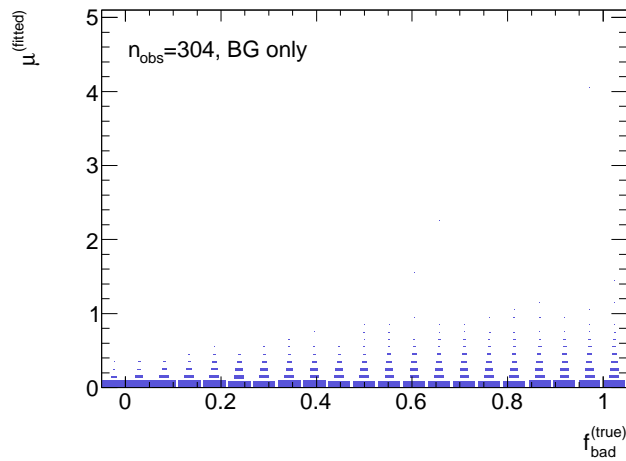
(b) μ^{fitted} vs. $f_{\mathrm{bad}}^{\mathrm{true}}$
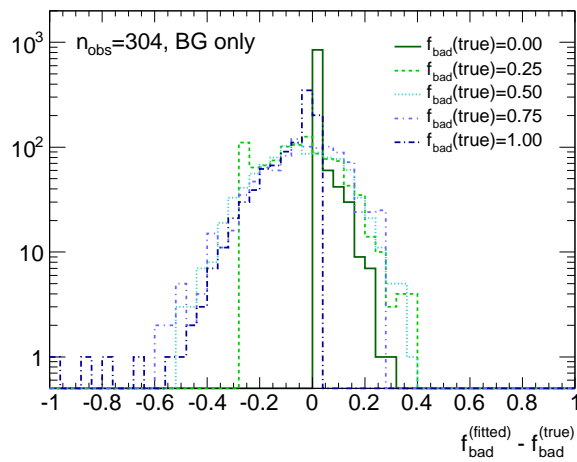
(c) $f_{\mathrm{bad}}^{\mathrm{fitted}} - f_{\mathrm{bad}}^{\mathrm{true}}$

Figure 9.5: The fitted parameters of f_{bad} (a) and μ (b) as a function of true f_{bad} derived from pseudo-experiments observing 304 events with the only backgrounds. The pull distributions of f_{bad} (c) for various true values are also shown.

(a) The TRT inner module

(b) The TRT middle module
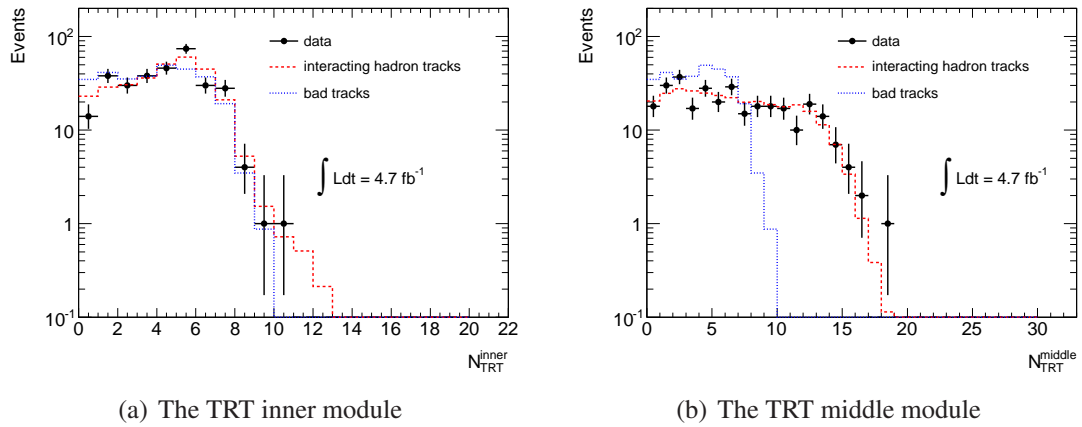
Figure 9.6: The distributions of the number of hits in the TRT module. The background expectations are derived from the control samples and normalized to the observed number of tracks. (a) and (b) show the distributions of hits in the inner module and the middle module, respectively.

Chapter 10

Results and Discussion

10.1 Results

Following the absence of an excess of data in the p_T spectrum of the high-p_T isolated disappearing tracks, the constraint on the isolated disappearing tracks is set.

10.1.1 Model Independent Limits

Model-independent upper limits on the cross-section times the acceptance for the non-SM processes with the final state satisfying the kinematic and track selection criteria are calculated. Figure 10.1 shows the upper limit at 95% CL on a cross section times acceptance from a counting of candidate tracks fulfilling that $p_T > p_T^0$ as a function of p_T^0, where p_T^0 is the threshold on the track p_T. The expected p_T spectrum of background tracks is derived by the background-only fit in the region $10 < p_T \leq 50$ GeV. A limit of less than 10^{-3} pb for $p_T^0 > 100$GeVon the cross-section times the acceptance is set at 95% CL.

10.1.2 Constraints on the Production Cross Section and the Properties of $\tilde{\chi}_1^\pm$

The upper limits on the production cress section for a given model at 95% confidence level is set by a point where the confidence level 'signal+background' hypothesis falls behind 5% when scanning a confidence level along various values of signal strength μ_s. Figure10.2, 10.3 and 10.4 show the upper limits on the cross section of LL01, LL02 and LL03 models at 95% CL as a function of the proper lifetime of the chargino. The interval $0.2 < \tau_{\tilde{\chi}_1^\pm} < 90$ ns is excluded for the LL01 model. A limit on the production cross section for chargino having a lifetime $1 < \tau_{\tilde{\chi}_1^\pm} < 2$ ns is set to be less than 8.7×10^{-3} pb. With the given dataset, the sensitivity is not enough to constrain the LL03 model at any value of $\tau_{\tilde{\chi}_1^\pm}$.

Figure 10.5 shows the constraint on the chargino mass and lifetime.The constraint on chargino mass up to nearly 118 GeV with the lifetime of $1 \sim 2$ ns is set at 95% CL. This constraint is obtained by interpreting the cross section limits for the LL01, LL02 and LL03 models described above. Using the upper limits of μ_s of the given models for each lifetime, the point at which the μ_s gives a value below one is calculated by using the linear interpolation. Figure 10.6 shows
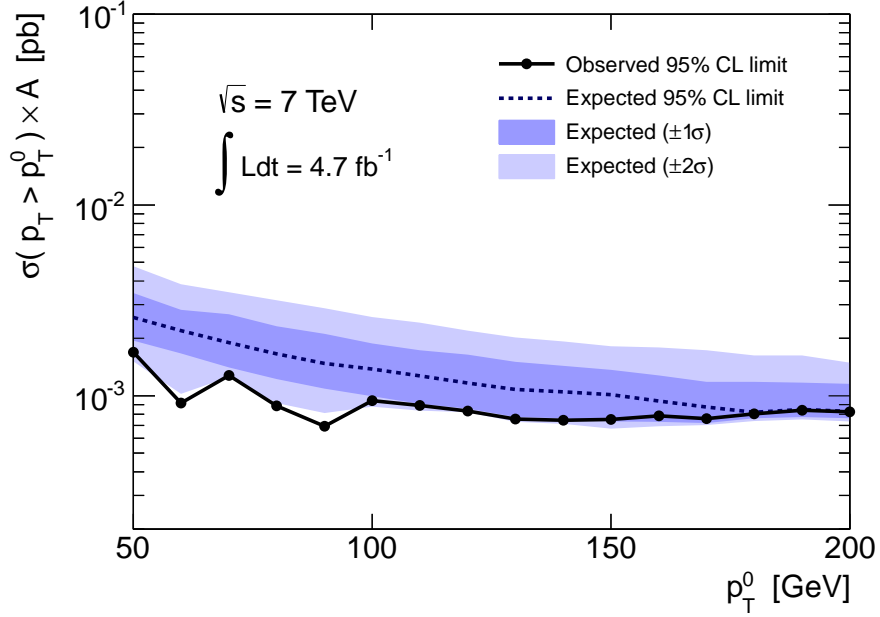
Figure 10.1: Model-independent upper limits on the cross section times the acceptance for an non-SM physics production with an isolated disappearing track with $p_T > p_T^0$ as a function of p_T^0. The observed bound at 95% CL and the expected bound with an integrated luminosity of 4.71 fb^{-1} are shown. The background estimate is derived from the background-only fit in the region $10 < p_T \leq 50$ GeV.
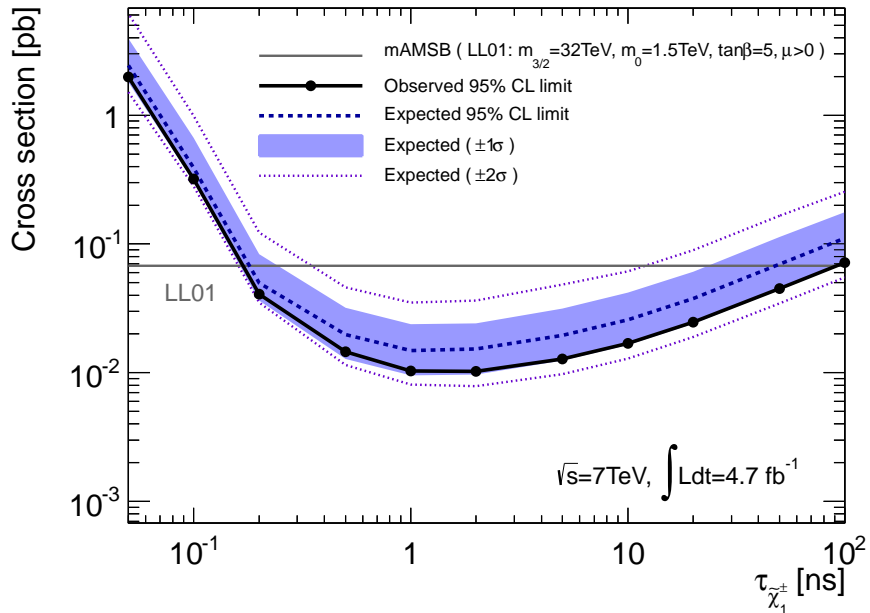
Figure 10.2: The observed and expected upper limits on the signal cross section as a function of chargino lifetime at 95% CL for $m_{\tilde{\chi}_1^\pm} = 90.2$ GeV. The band and dotted line indicate the range where the limit is expected to lie, assuming no signal. The line of 6.79×10^{-2} pb corresponds to the theoretical cross section of the LL01 model.
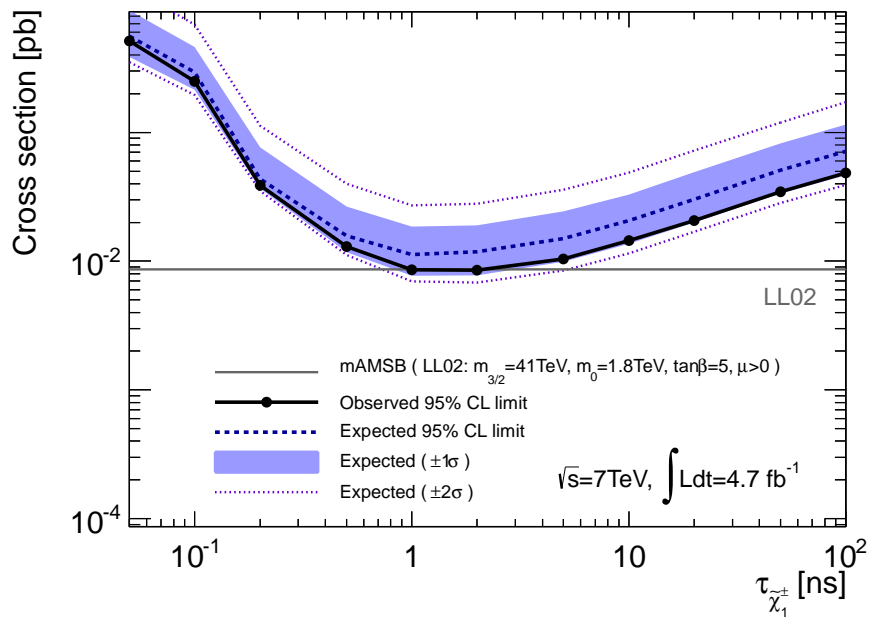
Figure 10.3: The observed and expected upper limits on the cross section as a function of the chargino lifetime at 95% CL for $m_{\tilde{\chi}_1^\pm} = 117.8$ GeV. The line of 8.66×10^{-3} pb corresponds to the theoretical cross section of the LL02 model.
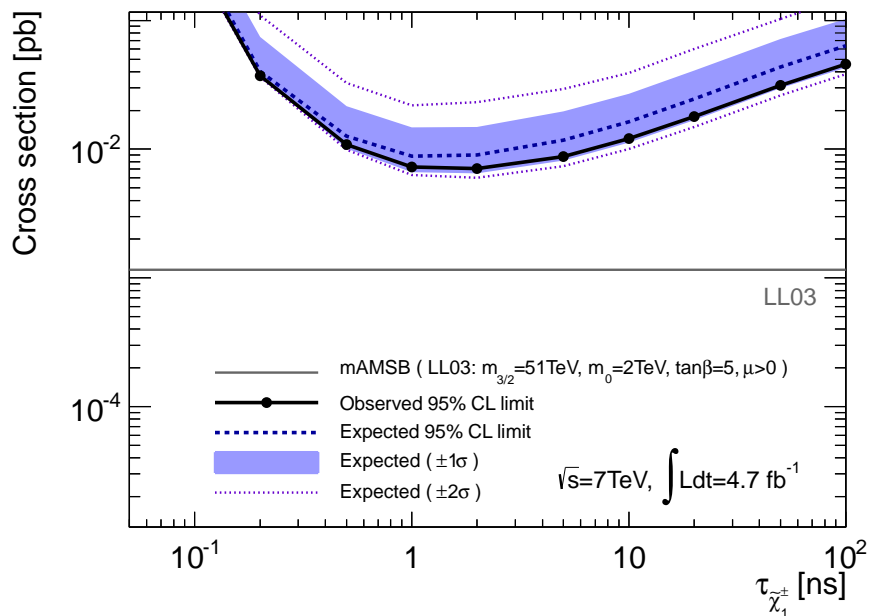
Figure 10.4: The observed and expected upper limits on the cross section as a function of the chargino lifetime at 95% CL for $m_{\tilde{\chi}_1^\pm} = 147.7$ GeV. The line of 1.16×10^{-3} pb corresponds to the theoretical cross section of the LL03 model.
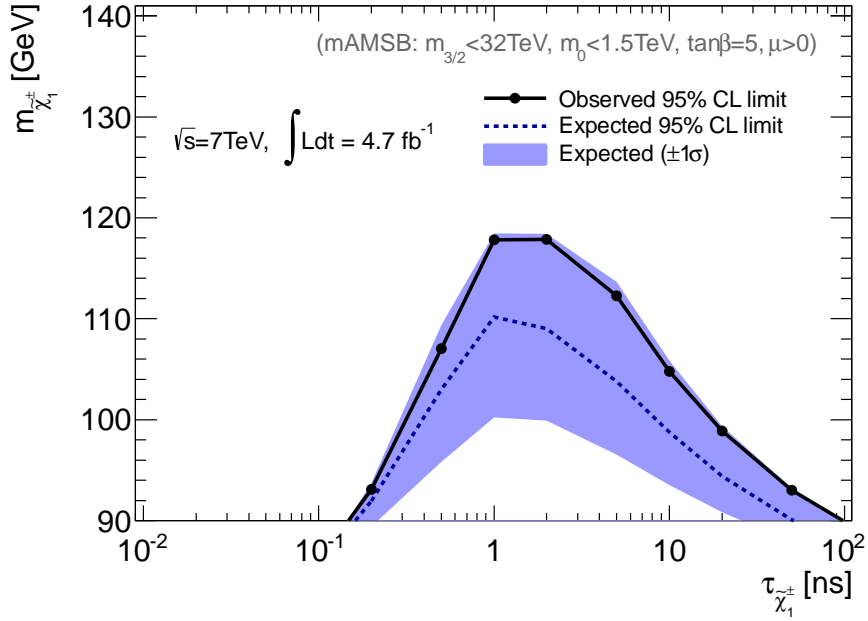
Figure 10.5: The constraint on the chargino mass and lifetime with 4.7fb^{-1} data. The observed bound is set at 95% CL. The black line shows the observed bound and the dashed blue line shows the expected bound. The constraint on chargino mass up to nearly 118 GeV with the lifetime of $1 \sim 2$ ns is set.

the constraint on the AMSB models in the m_0-$m_{\frac{3}{2}}$ plane. The constraint is calculated by interpreting the results on the assumption of $\tau_{\tilde{\chi}_1^\pm} = 0.3(1.0)$ ns. In the region of $m0 > 2000$ GeV, the constraint of $m_{\frac{3}{2}} < 34(38)$ TeV is set. The constraint on a chargino with $\tau_{\tilde{\chi}_1^\pm} = 1$ ns is set to be around 120 GeV in the region that $m_0 > 2000$ GeV while the constraint on a chargino with $\tau_{\tilde{\chi}_1^\pm} = 0.3$ ns is set to be around 100 GeV in the same $m_{\frac{3}{2}}$ region. In the small m_0 region, more stringent limits are set: $m_{\frac{3}{2}} < 38(48)$ TeV for $m_0 = 1000$ GeV at 95% CL.

10.2   Discussion

The direct search for decaying chargino is performed in this analysis. The method for the identification of the disappearing tracks is established in order to distinguish the exotic signals of the high-p_T tracks disappearing in the detector. For this search, the TRT detector is essential because it has a large number of drift tubes and provide continuous hits for charged particles. The analysis techniques newly developed in this dissertation make it possible to explore new long-lived particles expected to appear in many SUSY scenarios, even in pp collisions where huge background particles prevent finding such signatures.

Moreover , a search for the AMSB with the direct chargino pair production is promising as an extension of this analysis. The $\tilde{\chi}_1^\pm$ has a lighter mass than that of colored sparticle, which leads to a larger production cross section as mentioned in Section 4.1.1. The production of the AMSB events via electroweak process in pp collisions is as following:

$$pp \rightarrow \tilde{\chi}_1^\pm \tilde{\chi}_1^0 j, \quad pp \rightarrow \tilde{\chi}_1^+ \tilde{\chi}_1^- j, \tag{10.1}$$
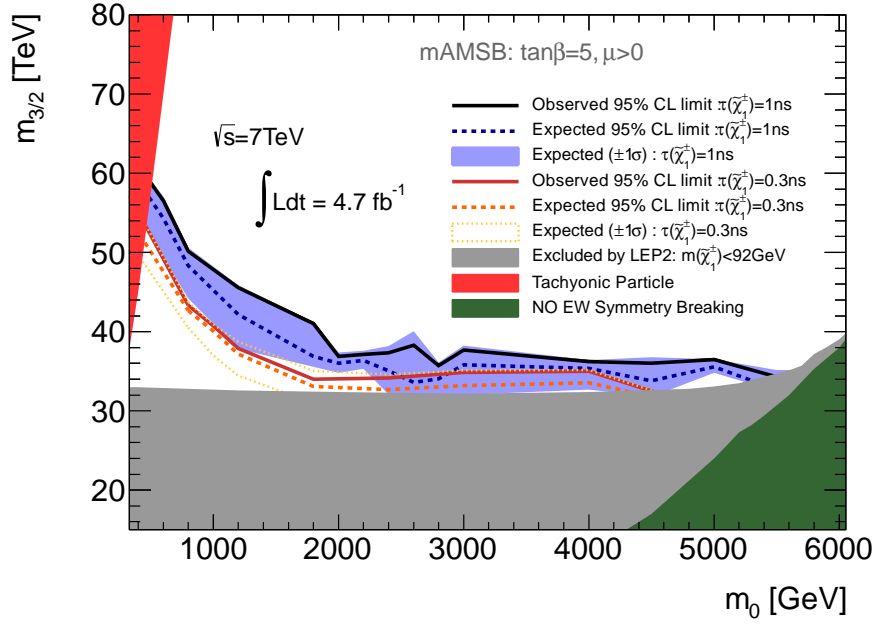
(a) with expected band
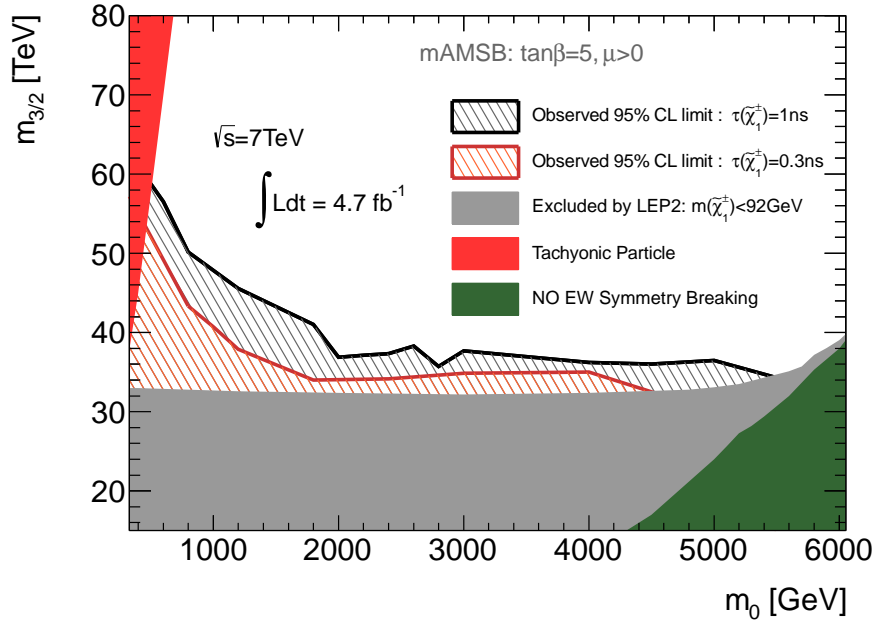
(b) without expected band

Figure 10.6: The constraint on the AMSB models in the m_0-$m_{\frac{3}{2}}$ plane. (a) shows the observed and expected upper limits. (b) shows the only observed excluded region. The black line and the dashed blue line show the observed and the expected upper limits for chargino having a lifetime $\tau_{\tilde{\chi}_1^\pm} = 1$ ns at 95% CL, respectively. The red line and the dashed orange line show the obserbed and the expected upper limits for chargino having a lifetime $\tau_{\tilde{\chi}_1^\pm} = 0.3$ ns at 95% CL, respectively. The red region is theoretically excluded because the sfermion becomes a tachyon due to a small m_0. The green region is also theoletically excluded due to no electroweak symmetry breaking. The mass of chargino in the gray region is below 92 GeVand is experimentally excluded by the LEP2.

131

where j denotes an energetic jet from initial-state radiation used to trigger the signal event. However, these jets in these events are soft or absent, therefore, the dedicated trigger for the events must be thought out well.

In addition, the use of pixel-seeded tracks may help to improve the sensitivity. This analysis is based on well-reconstructed tracks. Hence, it is impossible to detect charginos decaying before the TRT detector as mentioned in Section 4.1. The number of chargino falls exponentially as a function of the decay length. The charge of the hits in the pixel detector is read out, and expected to be also useful for the search for the short track with large dE/dx originating from charginos decaying in the SCT detector. However, the underlying hits from hadrons such as pions is enormous at pp collisions. These extended searches require dedicated studies on the track reconstruction and its performance.

There are many ideas for improving the sensitivities of the search for long-lived charginos. It may be challenging to develop the trigger dedicated for the direct chargino pair production and the method for the detection of the short track with large dE/dx. However, they must be very interesting and attracting studies and lead further understandings of the physics on the supersymmetry.

Chapter 11

Summary

The search for long-lived charginos inspired by the AMSB models is performed using 4.7 fb^{-1}data of pp collisions at $\sqrt{s} = 7$ TeV with the ATLAS detector.

The AMSB model is a very attractive SUSY model for a simple mechanism of the SUSY mediation. In the AMSB model, the wino is the lightest gaugino. The dominant component of the lightest chargino $\tilde{\chi}_1^{\pm}$ and the lightest neutralino $\tilde{\chi}_1^0$ are charged and neutral wino respectively. The mass of $\tilde{\chi}_1^{\pm}$ and $\tilde{\chi}_1^0$ are degenerated and the difference of masses are nearly a few hundred MeV. Due to the mass degeneracy, the lifetime of the lightest chargino becomes long. The lightest chargino produced in LHC decays to energetic neutralino and a soft charged pion. When the charginos decay in the inner detector of the ATLAS, the exotic signal of the chargino is expected. The lightest chargino having a long lifetime is reconstructed as a high-p_T track with the detector. Neutralino escapes detection and a soft charged particle is hard to be reconstructed in the detector. Therefore, the chargino decaying in the tracking volume is expected to be reconstructed as "disappearing "track.

In this dissertation, a method for detecting such chargino tracks is newly developed. The TRT detector is suitable for detecting the long-lived chargino signals. The TRT detector consists of a large number of the drift tubes and the number of hits are proportional to the decay point of a particle. In this analysis, the number of TRT hits in the outer module ($N_{\text{TRT}}^{\text{outer}}$) is employed for identification of the decaying track in the inner detector. The high-p_T isolated tracks is required that $N_{\text{TRT}}^{\text{outer}}$ is less than five as a chargino track selection

In this search, the data of pp collisions collected with the ATLAS detector is corresponding to 4.7fb^{-1}. The analysis is focused on the colored sparticle pair production process. As event selection criteria, large missing E_T and multiple energetic jets are required. The chargino track selections are required for the events fulfilling these event selection.

After the selection requirements are applied, the major backgrounds are *Interacting hadron track* and *Badly reconstructed track*. Interacting hadron track is a dominant source of the background for this analysis. This track originates from jets or taus and makes hadron interaction with the TRT detector material. The second source of the background is badly reconstructed tracks. This is a high-p_T mis-reconstructed track of the low-momentum particle which is scattered in the silicon detector materials.

In order to estimate backgrounds and extract the signal yields, the data-driven method is employed by using the unbinned maximum likelihood techniques. The p_T spectra of the signal and two backgrounds are used for the estimation. The p_T spectra of two background are

extracted from these control samples of each backgrounds. The p_T spectrum of the candidate tracks is consistent with the background-only hypothesis and no excess of data is found.

New constraints on the chargino properties and the AMSB model parameters are then set. The constraint on a chargino with $\tau_{\tilde{\chi}_1^\pm} = 1$ ns is set up to around 120 GeV in the region that $m_0 > 2000$ GeV while the constraint on a chargino with $\tau_{\tilde{\chi}_1^\pm} = 0.3$ ns is set up to around 100 GeVin the same $m_{\frac{3}{2}}$ region. In the small m_0 region ($m_0 < 2000$ GeV), the constraint on a chargino with $\tau_{\tilde{\chi}_1^\pm} = 0.3$ ns having a mass $m_{\tilde{\chi}_1^\pm} \sim 150$ GeV is set at 95%CL.

Bibliography

[1] A. Zee, *Fearful Symmetry: The Search for Beauty in Modern Physics.* Princeton University Press, 2nd ed., 2007.

[2] V. J. Stenger, *TIMELESS REALITY: Symmetry Simplicity, and Multiple Universes.* Prometheus Books, 2000.

[3] F. Halzen and A. D. Martin, *QUARKS & LEPTONS: An Introductory Course in Modern Particle Physics.* John Wiley & Sons, Inc., 1984.

[4] ATLAS Collaboration, *Observation of a new particle in the search for the Standard Model Higgs boson with the ATLAS detector at the LHC.*, Phys. Lett. **B716** (2012) 1.

[5] CMS Collaboration, *Observation of a new boson at a mass of 125 GeV with the CMS experiment at the LHC*, Phys. Lett. **B716** (2012) 30.

[6] S. P. Martin, *A Supersymmetry Primer*, `arXiv:hep-ph/9709356v6`.

[7] H. Baer and X. Tata, *Weak Scale Supersymmetry From Superfields to Scattering Events.* Cambridge University Press, 2006.

[8] I. Aitchison, *Supersymmetry in Particle Physics An Elementary Introduction.* Cambridge University Press, 2007.

[9] P. Labelle, *Supersymmetry Demystified.* The McGraw-Hill Companies, Inc., 2010.

[10] H. Miyazawa, *Baryon Number Changing Currents*, Prog. Theor. Phys **36** (1966) 1266.

[11] Y. Golfand and E. Likhtman, *EXTENSION OF THE ALGEBRA OF POINCARE GROUP GENERATORS AND VIOLATION OF P INVARIANCE*, Pis'ma ZhETF **13** (1971) 452.

[12] D. Volkov and V. Akulov, *POSSIBLE UNIVERSAL NEUTRINO INTERACTION*, Pis'ma ZhETF **16** (1972) 621.

[13] J. Wess and B. Zumino, *SUPERGAUGE TRANSFORMATIONS IN FOUR DIMENSIONS*, Nucl. Phys. B **70** (1974) 39.

[14] S. Dimopoulos and H. Georgi, *SOFTLY BROKEN SUPERSYMMETRY AND SU(5)*, Nucl. Phys. B **193** (1981) 150.

[15] D. Kazakov, *Supersymmetry in particle physics:the renormalization group viewpoint*, Phys. Rep. **344** (2001) 309.

[16] G. F. Giudice, M. A. Luty, H. Murayama, and R. Rattazzi, *Gaugino Mass without Singlets*, JHEP **12** (1998) 027, `arXiv:hep-ph/9810442`.

[17] L. Randall and R. Sundrum, *Out of this world supersymmetry breaking*, Nucl. Phys. **B557** (1999) 79–118, `arXiv:hep-th/9810155`.

[18] A. J. Barr, C. G. Lester, M. A. Parker, B. C. Allanach, and P. Richardson, *Discovering anomaly-mediated supersymmetry at the LHC*, JHEP **03** (2003) 045.

[19] ALEPH Collaboration, A. Heister et al., *Search for charginos nearly mass degenerate with the lightest neutralino in e+e- collisions at centre-of-mass energies up to 209 GeV*, Phys. Lett. **B533** (2002) 223–236, `arXiv:hep-ex/0203020`.

[20] OPAL Collaboration, *Search for nearly mass degenerate charginos and neutralinos at LEP*, Eur. Phys. J. **C29** (2003) 479–489, `arXiv:hep-ex/0210043`.

[21] DELPHI Collaboration, *Search for SUSY in the AMSB scenario with the DELPHI detector*, Eur. Phys. J. **C34** (2004) 145–156, `arXiv:hep-ex/0403047`.

[22] LEP2 SUSY Working Group, *Combined LEP Chargino Results, up to 208 GeV for low DM*, `http://lepsusy.web.cern.ch/lepsusy/www/inoslowdmsummer02/charginolowdm_pub.html`.

[23] ATLAS Collaboration, *Search for anomaly-mediated supersymmetry breaking with the ATLAS detector based on a disappearing-track signature in pp collisions at $\sqrt{s}$=7 TeV*, Eur. Phys. J. **C72** (2012) 1993.

[24] L. Evans and P. B. (editors), *LHC Machine*, JINST **3** (2008) S08001.

[25] ATLAS Collaboration, G. Aad et al., *The ATLAS Experiment at the CERN Large Hadron Collider*, JINST **3** (2008) S08003.

[26] CMS Collaboration, *CMS technical proposal*, CERN-LHCC-94-38, CERN, Geneva, 1994.

[27] LHCb Collaboration, *LHCb technical proposal*, CERN-LHCC-98-004, CERN, Geneva, 1998.

[28] TOTEM Collaboration, *Total cross section, elastic scattering and diffractive dissociation at the LHC: Technical Proposal*, CERN-LHCC-99-007, CERN, Geneva, 1999.

[29] ALICE Collaboration, *ALICE: Technical proposal for a Large Ion collider Experiment at the CERN LHC*, CERN-LHCC-95-71, CERN, Geneva, 1995.

[30] UA1 Collaboration, G. ARNISON et al., *EXPERIMENTAL OBSERVATION OF ISOLATED LARGE TRANSVERSE ENERGY ELECTRONS WITH ASSOCIATED MISSING ENERGY AT $\sqrt{s}$ = 540 GeV*, Phys. Lett. **B122** (1983) 103.

[31] UA2 Collaboration, M. BANNER et al., *OBSERVATION OF SINGLE ISOLATED ELECTRONS OF HIGH TRANSVERSE MOMENTUM IN EVENTS WITH MISSING TRANSVERSE ENERGY AT THE CERN $\bar{p}p$ COLLIDER*, Phys. Lett. **B122** (1983) 476.

[32] UA1 Collaboration, G. ARNISON et al., *EXPERIMENTAL OBSERVATION OF LEPTON PAIRS OF INVARIANT MASS AROUND 95GeV/c² AT THE CERN SPS COLLIDER*, Phys. Lett. **B126** (1983) 398.

[33] UA2 Collaboration, P. BAGNAIA et al., *EVIDENCE FOR $Z^0 \rightarrow e^+ e^-$ AT THE CERN $\bar{p}p$ COLLIDER*, Phys. Lett. **B129** (1983) 130.

[34] ATLAS Collaboration, G. Aad et al., *Detector and physics performance: Technical Design Report, 1*, CERN-LHCC-99-014, CERN, Geneva, 1999.

[35] ATLAS Collaboration, G. Aad et al., *Detector and physics performance: Technical Design Report, 2*, CERN-LHCC-99-015, CERN, Geneva, 1999.

[36] ATLAS Collaboration, *ATLAS inner detector: Technical Design Report, 1*, CERN-LHCC-97-016, CERN, Geneva, 1997. http://atlas.web.cern.ch/Atlas/GROUPS/INNER_DETECTOR/TDR/tdr.html.

[37] ATLAS Collaboration, *ATLAS inner detector: Technical Design Report, 2*, CERN-LHCC-97-017, CERN, Geneva, 1997. http://atlas.web.cern.ch/Atlas/GROUPS/INNER_DETECTOR/TDR/tdr.html.

[38] ATLAS TRT Collaboration, E. Abat et al., *The ATLAS Transition Radiation Tracker (TRT) proportional drift tube: design and performance*, JINST **3** (2008) P02013.

[39] ATLAS TRT Collaboration, E. Abat et al., *The ATLAS TRT Barrel Detector*, JINST **3** (2008) P02014.

[40] ATLAS TRT Collaboration, E. Abat et al., *The ATLAS TRT end-cap detectors*, JINST **3** (2008) P10003.

[41] K. Kleinknecht, *Detectors for particle radiation*. Cambridge University Press, 2nd ed., 1998.

[42] V. L. GINZBURG, *CERTAIN THEORETICAL ASPECTS OF RADIATION DUE TO SUPERLUMINAL MOTION IN A MEDIUM*, Sov. Phys. Usp. **2** (1960) 874.

[43] M. L. Cherry, G. Hertmann, D. Müller, and T. A. Prince, *Transition radiation from relativistic electrons in periodic radiators*, Phys. Rev. **D10** (1974) no. 11, 3594.

[44] B. Dolgoshein, *Transition radiation detectors*, Nucl. Instrum. Methods Phys. Res., Sect. **A326** (1993) 434.

[45] ATLAS Collaboration, *ATLAS Experiment - Public Results*, https://twiki.cern.ch/twiki/bin/view/AtlasPublic/.

[46] ATLAS Collaboration, G. Aad et al., *The ATLAS Simulation Infrastructure*, Eur. Phys. J. **C70** (2010) 823–874, arXiv:1005.4568 [physics.ins-det].

[47] G. Barrand et al., *GAUDI - A software architecture and framework for building LHCb data processing applications*, in *CHEP2000*. Padova, February, 2000.

[48] GEANT4 Collaboration, S. Agostinelli et al., *GEANT4: A simulation toolkit*, Nucl. Instrum. Meth. **A506** (2003) 250–303.

[49] T. Cornelissen, M. Elsing, A. Wildauer, N. van Eldik, E. Moyse, W. Liebig, N. Piacquadio, K. Prokoev, and A. Salzburger, *Updates of the ATLAS Tracking Event Data Model (Release 13)*, ATL-SOFT-PUB-2007-003, CERN, Geneva, Dec, 2007.

[50] T. Cornelissen, M. Elsing, S. Fleischmann, W. Liebig, E. Moyse, and A. Salzburger, *Concepts, Design and Implementation of the ATLAS New Tracking (NEWT)*, ATL-SOFT-PUB-2007-007. ATL-COM-SOFT-2007-002, CERN, Geneva, Mar, 2007.

[51] A. Salzburger, *The ATLAS Track Extrapolation Package*, ATL-SOFT-PUB-2007-005. ATL-COM-SOFT-2007-010, CERN, Geneva, Jun, 2007.

[52] ATLAS Collaboration, *Performance of primary vertex reconstruction in proton-proton collisions at $\sqrt{s} = 7TeV$ in the ATLAS experiment*, ATLAS-CONF-2010-069, CERN, Geneva, Jul, 2010.

[53] ATLAS Collaboration, *Performance of the ATLAS Inner Detector Track and Vertex Reconstruction in the High Pile-Up LHC Environment*, ATLAS-CONF-2012-042, CERN, Geneva, Mar, 2012.

[54] R. Frühwirth, W. Waltenberger, and P. Vanlaer, *Adaptive Vertex Fitting*, J. Phys. **G34** (2007) N343. CERN-CMS-NOTE-2007-008.

[55] M. Cacciari, G. P. Salam, and G. Soyez, *The anti-k_t jet clustering algorithm*, JHEP **04** (2008) 063.

[56] ATLAS Collaboration, *Expected electron performance in the ATLAS experiment*, ATL-PHYS-PUB-2011-006, CERN, Geneva, May, 2011.

[57] ATLAS Collaboration, G. Aad et al., *Electron performance measurements with the ATLAS detector using the 2010 LHC proton-proton collision data*, Eur. Phys. J. **C72** (2012) 1909.

[58] R. Nicolaidou, L. Chevalier, S. Hassani, J. Laporte, E. LeMenedeu, and A. Ouraou, *Muon identification procedure for the ATLAS detector at the LHC using Muonboy reconstruction package and tests of its performance using cosmic rays and single beam data*, J. Phys.: Conf. Ser. **219** (2010) 032052.

[59] S. Hassani, L. Chevalier, E. Lançon, J.-F. Laporte, R. Nicolaidou, and A. Ouraou, *A muon identification and combined reconstruction procedure for the ATLAS detector at the LHC using the (MUONBOY, STACO, MuTag) reconstruction packages*, Nucl. Instrum. Methods Phys. Res., Sect. A **572** (2007) 77.

[60] T. Lagouri, D. Adams, K. Assamagan, M. Biglietti, G. Carlino, G. Cataldi, F. Conventi, A. Farilla, Y. Fisyak, S. Goldfarb, E. Gorini, K. Mair, L. Merola, A. Nairz, A. Poppleton, M. Primavera, S. Rosati, J. Shank, S. S. andL. Spogli, G. Stavropoulos, M. Verducci, and T. Wenaus, *A muon identification and combined reconstruction procedure for the ATLAS detector at the LHC at CERN*, IEEE. Trans. Nucl. Sci. **51** (2004) no. 6, 3030.

[61] D. Adams, K. Assamagan, M. Biglietti, G. Carlino, G. Cataldi, F. Conventi, A. Farilla, Y. Fisyak, S. Goldfarb, E. Gorini, T. Lagouri, K. Mair, L. Merola, A. Nairz, A. Poppleton, M. Primavera, S.Rosati, J. Shank, S. Spagnolo, L. Spogli, G. Stavropoulos, M. Verducci, and T. Wenaus, *Track Reconstruction in the ATLAS Muon Spectrometer with MOORE*, ATL-SOFT-2003-007, CERN, Geneva, Oct, 2003.

[62] ATLAS Collaboration, *Performance of missing transverse momentum reconstruction in proton-proton collisions at $\sqrt{s}$ = 7TeV with ATLAS*, Euro. Phys. J. **C72** (2012) 1844.

[63] M. Bahr, S. Gieseke, M. Gigg, D. Grellscheid, K. Hamilton, et al., *Herwig++ Physics and Manual*, Eur.Phys.J. **C58** (2008) 639–707, arXiv:0803.0883 [hep-ph].

[64] A. Sherstnev and R. S. Thorne, *Parton Distributions for LO Generators*, Eur. Phys. J. **C55** (2008) 553–575, arXiv:0711.2473 [hep-ph].

[65] M. Krämer and A. Kulesza, *NLO+NLL SUSY-QCD*, http://web.physik.rwth-aachen.de/service/wiki/bin/view/Kraemer/SquarksandGluinos.

[66] W. Beenakker, R. Hpker, M. Spira, and P. Zerwas, *Squark and Gluino Production at Hadron Colliders*, Nucl. Phys. **B492** (1997) 51–103.

[67] A. Kulesza and L. Motyka, *Threshold resummation for squark-antisquark and gluino-pair production at the LHC*, Phys. Rev. Lett. **102** (2009) 111802.

[68] A. Kulesza and L. Motyka, *Soft gluon resummation for the production of gluino-gluino and squark-antisquark pairs at the LHC*, Phys. Rev. **D80** (2009) 095004.

[69] W. Beenakker, S. Brensing, M. Krmer, A. Kulesza, E. Laenen, and I. Niessen, *Soft-gluon resummation for squark and gluino hadroproduction*, JHEP **0912** (2009) 041.

[70] T. Sjostrand, S. Mrenna, and P. Z. Skands, *PYTHIA 6.4 Physics and Manual*, JHEP **0605** (2006) 026, arXiv:hep-ph/0603175.

[71] M. L. Mangano, M. Moretti, F. Piccinini, R. Pittau, and A. D. Polosa, *ALPGEN, a generator for hard multiparton processes in hadronic collisions*, JHEP **0307** (2003) 001, arXiv:hep-ph/0206293 [hep-ph].

[72] S. Frixione and B. R. Webber, *Matching NLO QCD computations and parton shower simulations*, JHEP **06** (2002) 029, arXiv:hep-ph/0204244.

[73] S. Frixione and B. R. Webber, *The MC@NLO 3.3 event generator*, arXiv:hep-ph/0612272.

[74] G. Corcella et al., *HERWIG 6.5 release note*, arXiv:hep-ph/0210213.

[75] J. M. Butterworth, J. R. Forshaw, and M. Seymour, *Multiparton interactions in photoproduction at HERA*, Z. Phys. **C72** (1996) 637–646, arXiv:hep-ph/9601371.

[76] P. M. Nadolsky, H.-L. Lai, Q.-H. Cao, J. Huston, J. Pumplin, D. Stump, W.-K. Tung, and C.-P. Yuan, *Implications of CTEQ global analysis for collider observables*, Phys. Rev. **D78** (2008) 013004, arXiv:0802.0007 [hep-ph].

[77] J. Pumplin, D. Stump, J. Huston, H. Lai, P. M. Nadolsky, and W. Tung, *New generation of parton distributions with uncertainties from global QCD analysis*, JHEP **0207** (2002) 012, `arXiv:0201195 [hep-ph]`.

[78] ATLAS Collaboration, G. Aad et al., *Jet energy measurement with the ATLAS detector in proton-proton collisions at $\sqrt{s} = 7\ TeV$*, .

[79] A. Martin, W. Stirling, R. Thorne, and G. Watt, *Parton distributions for the LHC*, Eur.Phys.J. **C63** (2009) 189–285, `arXiv:0901.0002 [hep-ph]`.

[80] ATLAS Collaboration, *Jet energy scale and its systematic uncertainty in proton-proton collisions at sqrt(s)=7 TeV in ATLAS 2010 data*, ATLAS-CONF-2011-032, CERN, Geneva, Mar, 2011.

[81] ATLAS Collaboration, G. Aad et al., *Charged-particle multiplicities in pp interactions measured with the ATLAS detector at the LHC*, New J.Phys. **13** (2011) 053033, `arXiv:1012.5104 [hep-ex]`.

[82] ATLAS Collaboration Collaboration, G. Aad et al., *Measurements of underlying-event properties using neutral and charged particles in pp collisions at 900 GeV and 7 TeV with the ATLAS detector at the LHC*, Eur.Phys.J. **C71** (2011) 1636, `arXiv:1103.1816 [hep-ex]`.

[83] ATLAS Collaboration, *Luminosity Determination in pp Collisions at sqrt(s) = 7 TeV using the ATLAS Detector in 2011*, ATLAS-CONF-2011-116, CERN, Geneva, Aug, 2011.

[84] ATLAS Collaboration Collaboration, G. Aad et al., *Luminosity Determination in pp Collisions at sqrt(s)=7 TeV Using the ATLAS Detector at the LHC*, Eur.Phys.J. **C71** (2011) 1630, `arXiv:1101.2185 [hep-ex]`.

[85] G. Cowan, K. Cranmer, E. Gross, and O. Vitells, *Asymptotic formulae for likelihood-based tests of new physics*, Eur. Phys. J. **C71** (2011) 1554, `arXiv:1007.1727 [physics.data-an]`.

[86] H. Burkhardt and P. Grafstrom, *Absolute Luminosity From Machine Parameters*, , May, 2007.

[87] W.Kozanecki, A.J.Bevan, B.F.Viaud, Y.Cai, A.S.Fisher, C.OGrady, B.Lindquist, A.Roodman, J. Thompson, and M.Weaver, *Interaction-point phase-space characterization using single-beam and luminous-region measurements at PEP-II*, Nucl. Instrum. Methods Phys. Res., Sect. A,Accel. Spectrom. Detect. Assoc. Equip. **607** (2009) 293–391.

[88] S. van der Meer, *CALIBRATION OF THE EFFECTIVE BEAM HEIGHT IN THE ISR*, , 1968.

[89] R. Früwirth, *APPLICATION OF KALMAN FILTERING TO TRACK AND VERTEX FITTING*, Nucl. Instr. and Meth. **A262** (1987) 444.

[90] E. J. Wolin and L. L. Ho, *Covariance Matrices for Track Fitting with the Kalman Filter*, Nucl. Instr. and Meth. **A219** (1993) 493.

[91] F. James, *Statistical Methods in Experimental Physics*. World Scientific Publishing Co. Pte. Ltd., 2nd ed., 2006.

Appendix A

Luminosity Determination

A.1 Luminosity

The instantaneous luminosity [84] at pp collider is expressed as,

$$\mathcal{L} = \frac{R_{\text{inel}}}{\sigma_{\text{inel}}} \tag{A.1}$$

where R_{inel} is the rate of inelastic collisions and σ_{inel} is the pp inelastic cross section. This expression is also described as

$$\mathcal{L} = \frac{\mu n_{\text{b}} f_{\text{r}}}{\sigma_{\text{inel}}} \tag{A.2}$$

where μ, n_{b} and f_{r} are the average number of inelastic interaction per bunch crossing, the number of bunch crossing and a revolution frequency, respectively. The instantaneous luminosity also can be rewritten as

$$\mathcal{L} = \frac{\mu^{\text{vis}} n_{\text{b}} f_{\text{r}}}{\varepsilon \sigma_{\text{inel}}} = \frac{\mu^{\text{vis}} n_{\text{b}} f_{\text{r}}}{\sigma_{\text{vis}}} \tag{A.3}$$

where ε is the efficiency for an inelastic pp collision to satisfy the event selection, and μ^{vis} is defined as $\varepsilon\mu$, which is the average number of visible inelastic interaction per bunch crossing. The visible cross section σ_{vis} is defined as $\varepsilon\sigma_{\text{inel}}$, which is the calibration constant that relates μ^{vis} to $\mathcal{L}$. μ^{vis} is measured by using several sub-detectors in the ATLAS.

In terms of the beam parameters, the absolute luminosity is expressed as,

$$\mathcal{L} = n_{\text{b}} f_{\text{r}} n_1 n_2 \int \rho_1(x, y) \rho_2(x, y) dx dy, \tag{A.4}$$

where n_1 and n_2 are the numbers of particles in the two colliding bunches and $\rho_1(x, y)$ and $\rho_2(x, y)$ are two transverse beam distributions[86, 87, 88]. For equal Gaussian beams,

$$\rho_1(x, y) = \rho_2(x, y) = \frac{1}{\sqrt{2\pi}\Sigma_x\Sigma_y} \exp\left[-\frac{x^2}{2\Sigma_x^2} - \frac{y^2}{2\Sigma_y^2}\right]. \tag{A.5}$$

where Σ_x and Σ_y characterize the widths of the horizontal and vertical beam profiles.

$$
\begin{aligned}
\mathcal{L} &= n_b f_r n_1 n_2 \int \frac{1}{2\pi \Sigma_x^2 \Sigma_y^2} \exp\left[-\frac{x^2}{\Sigma_x^2} - \frac{y^2}{\Sigma_y^2}\right] dx dy \\
&= n_b f_r n_1 n_2 \frac{1}{2\pi \Sigma_x^2 \Sigma_y^2} \Sigma_x \Sigma_y \\
&= \frac{n_b f_r n_1 n_2}{2\pi \Sigma_x \Sigma_y}
\end{aligned}
\tag{A.6}
$$

For determination of Σ_x and Σ_y, *van der Meer (vdM) Scan* is employed. The observed event rate is recorded when scanning the two beams across each other in x-direction and y-direction. This measurements gives two bell-shaped curves, with the maximum rate at zero separation. Σ_x and Σ_y can be extracted from these curves. Using Σ_x and Σ_y determined by the *vdM* scan, the luminosity $\mathcal{L}$ is calculated by Equation A.6. σ_{vis} is also extracted from A.3 using the measured value of $\mathcal{L}$.

The *vdM* technique allows the determination of σ_{vis} without *a priori* knowledge of the inelastic pp cross section. The ATLAS uses the *vdM* technique for the determination of the absolute luminosity. The basic time unit for storing luminosity information is referred as the *Luminosity Block* (LB) which is set by the ATLAS DAQ system. The duration of a LB is about two minutes. All data quality information are stored for each LB.

A.2   Luminosity Detector

Several detectors such as the Inner Detector or the Forward Detector are employed for the luminosity determination. In the several sub-detectors of the ATLAS, the Beam Conditions Monitor (BCM) is mainly used for the luminosity calculation. The primary purpose of BCM is monitoring beam loses and providing fast feedback to the accelerator operation. The BCM consists of two arms of diamond sensors located at $Z = \pm 184$ cm and $r = 5.5$ cm. It uses programmable front-end electronics to histogram the single-sided and coincidence rates as function of Bunch Crossing Identifier (BCID). These histograms are read out by a software and made available to other online applications. The BCM has a excellent timing (0.7ns) which allows for the rejection of backgrounds from beam-halo.

A.3   Luminosity Calculation

The calculation of instantaneous luminosity is performed by the Online Luminosity Calculator (OLC). The task of OLC is retrieving the raw luminosity information such as hit counts or number of colliding bunches n_b and using these data to determine μ. There are several algorithm for calculation and the OLC outputs the instantaneous luminosity, which is averaged over all colliding BCIDs for each algorithm.

Main algorithm using the BCM detector counts the number of events per bunch crossings (BC) in which at least one hit above threshold occurs on either the A-side, the C-side or both. The value of μ_i^{vis} used to determine the bunch luminosity $\mathcal{L}_i$ in BCID i is obtained from the raw number of counts N_i and the number of bunch crossings N_{BC}. The algorithm is assuming that:

- the number of pp interactions occurring in any BC obeys a Poisson distribution.

- the efficiency to detect a single inelastic pp interaction is constant.

The bunch luminosity is given by

$$\mathcal{L}_i = \frac{\mu_i^{\text{vis}} f_r}{\sigma_{\text{vis}}}. \tag{A.7}$$

using the value of σ_{vis} measured during the vdM scans for the algorithm considered. The Poisson probability for observing zero events in a given bunch crossing is $P_0(\mu^{\text{vis}}) = e^{-\mu^{\text{vis}}}$. Then, by using the raw number of counts N, the probability of observing at least one event is

$$\begin{aligned} P(\mu^{\text{vis}}) &= \frac{N}{N_{\text{BC}}} \\ &= 1 - P_0(\mu^{\text{vis}}) \\ &= 1 - e^{-\mu^{\text{vis}}}. \end{aligned} \tag{A.8}$$

In terms of μ^{vis}, the event counting rate is given as

$$\mu^{\text{vis}} = -\ln\left(1 - \frac{N}{N_{\text{BC}}}\right). \tag{A.9}$$

By using the μ^{vis} determined by the detector and the σ_{vis} measured by vdM scans, the bunch luminosity is obtained.

Appendix B

Details of Concepts for Tracking

B.1 Pattern Recognition

B.1.1 Histogramming

Histogramming methods is widely uses as a common technique for a pattern recognition. Track momentum p as expressed by using a curvature ρ as

$$p = 0.3B\rho, \tag{B.1}$$

where B is a magnetic field. A radius of a curvature is proportional to the momentum of a track. Therefore, the higher momentum track has, the nearer to a line the trajectory of the track becomes. By assuming tracks come from a origin of the coordinate, the point corresponding to a track make a peak in the histogram filled the ϕ information of hits in the detector. This technique is for high momentum tracks originating from the origin of the coordinate. Therefore, it isn't suitable for tracks with low momentum or not from the collision.

B.1.2 Hough Transform

Hough transform technique is also commonly used in tracking. This technique is a transformation from hits information in detector to the parameter space. For example, (x, y) information of hits is transformed to parameters by assuming a line

$$d = x\cos\theta + y\sin\theta, \tag{B.2}$$

where, d is a distance from the origin to a track and θ is a azimuthal angle of a normal line to the track. Each hits are transformed to d by scanning values of θ and filled in a histogram. A peak in the histogram corresponds to a track.

B.2 Track Fitting

After the pattern recognition, track fitting is performed. In this section, some of major methods in tracking is explained.

B.2.1 Global χ^2 Fit

The measurement in a `Surface`, i.e. information of a hit is employed for track fitting.

$$c = \begin{pmatrix} m_1 \\ \vdots \\ m_n \end{pmatrix} = f(x) + \epsilon, \tag{B.3}$$

where ϵ is a random noise and $\langle \epsilon \rangle = 0$. The covariance matrix V is defined as

$$\begin{aligned} V &= \langle (c - \langle c \rangle)(c - \langle c \rangle)^{\mathrm{T}} \rangle \tag{B.4} \\ &= \langle (c - \langle f(x) \rangle)(c - \langle f(x) \rangle)^{\mathrm{T}} \rangle. \tag{B.5} \end{aligned}$$

$$\tag{B.6}$$

Global χ^2 fit calculates χ^2 by using the track information and the detector measurements.

$$f(x) = f(x_0) + A(x - x_0), \tag{B.7}$$

where A is defined as

$$A = \left. \frac{\partial f(x)}{\partial x} \right|_{x=x_0}. \tag{B.8}$$

χ^2 is defined as

$$\chi^2 = (c - f(x))^{\mathrm{T}} V^{-1} (c - f(x)), \tag{B.9}$$

and the track fitting is performed as χ^2 is minimized.

B.2.2 Kalman Filter

The global χ^2 fit is the method which employs all the measurements for track fitting comprehensively while Kalman Filter is the method that repeats fitting a tracks state with the neighboring measurement recursively.[89, 90] Kalman Filter is a technique for filtering discrete data and devised by S.E. Kalman in 1960. This filtering technique is used in high energy physics for tracking.

Kalman Filter mainly consists of three steps: *Prediction*, *Filtering* and *Smoothing*. Discrete states of a track and the corresponding measurements of a detector are expressed as x_k and $m_k (k = 1, \ldots, N)$. The relation of x_k and m_k is

$$m_k = H_k x_k + \epsilon_k, \tag{B.10}$$

where ϵ_k is errors of measurements and in ideal case,

$$\langle \epsilon_k \rangle = 0. \tag{B.11}$$

The covariance matrix of ϵ_k is expressed as

$$\mathrm{cov}[\epsilon_k] \equiv V_k. \tag{B.12}$$

Moreover, the transition of (k-1)-th state of a track to the k-th state is expressed as

$$x_k = F_k x_{k-1} + \omega_k, \tag{B.13}$$

where ω_k is a process noise through the transition. ω_k fulfills that

$$\langle \omega_k \rangle = \mathbf{0}. \tag{B.14}$$

The covariance matrix of ω_k is expressed as

$$\mathrm{cov}[\omega_k] \equiv Q_k. \tag{B.15}$$

$\tilde{x}_{k|j}$ denotes the predicted state estimate using the $0, \cdots, j$ states and the covariance matrix of $x_k - \tilde{x}_{k|j}$ is expressed as $C_{k|j}$.

$$r_{k|j} = m_k - H_k \tilde{x}_{k|j} = H_k(x_k - \tilde{x}_{k|j}) + \epsilon_k. \tag{B.16}$$

$$\mathrm{cov}[r_{k|j}] \equiv R_{k|j}. \tag{B.17}$$

B.2.3 Prediction

Prediction is the estimation of the state at a future time. Extrapolation of the state vector is expressed as

$$\tilde{x}_{k|k-1} = F_{k-1} \tilde{x}_{k-1|k-1}. \tag{B.18}$$

Extrapolation of the covariance matrix is expressed as

$$\begin{aligned}
C_{k|k-1} &= \mathrm{cov}[x_k - \tilde{x}_{k-1|k-1}] \\
&= \mathrm{cov}[x_k - F_{k-1} \tilde{x}_{k-1|k-1}] \\
&= \mathrm{cov}[F_{k-1}(x_k - \tilde{x}_{k-1|k-1}) + \omega_{k-1}] \\
&= F_{k-1} C_{k-1|k-1} F_{k-1}^T + Q_{k-1}.
\end{aligned} \tag{B.19}$$

Residuals of the prediction is given by

$$r_{k|k-1} = m_k - H_k \tilde{x}_{k|k-1}. \tag{B.20}$$

Covariance of the predicted residuals is expressed as

$$\begin{aligned}
R_{k|k-1} &= \mathrm{cov}[m_k + H_k \tilde{x}_{k|k-1}] \\
&= \mathrm{cov}[H_k x_k - H_k \tilde{x}_{k|k-1} + \epsilon_k] \\
&= \mathrm{cov}[H_k(x_k - \tilde{x}_{k|k-1}) + \epsilon_k] \\
&= H_k C_{k|k-1} H_k^T + V_k.
\end{aligned} \tag{B.21}$$

B.2.4 Filtering

Filtering is the estimation of the present state based on all past measurements. Using the residual $r_{k|k-1}$, the track state is updated as

$$\begin{aligned}
\tilde{x}_{k|k} &= \tilde{x}_{k|k-1} + K_k \tilde{r}_{k|k-1} \\
&= \tilde{x}_{k|k-1} + K_k(m_k - H_k \tilde{x}_{k|k-1}).
\end{aligned} \tag{B.22}$$

Here, the matrix $\boldsymbol{K}_k$ is required to be

$$\frac{\partial(\mathrm{Tr}\boldsymbol{C}_{k|k})}{\partial \boldsymbol{K}_k} = 0, \tag{B.23}$$

where $\boldsymbol{C}_{k|k}$ is a covariance matrix of $\boldsymbol{x}_k - \tilde{\boldsymbol{x}}_{k|k}$

$$\boldsymbol{C}_{k|k} = \mathrm{cov}[\boldsymbol{x}_k - \tilde{\boldsymbol{x}}_{k|k}]. \tag{B.24}$$

Then, $\boldsymbol{K}_k$ satisfies

$$\boldsymbol{K}_k = \boldsymbol{C}_{k|k-1}\boldsymbol{H}_k^T\boldsymbol{R}_{k|k-1}^{-1}. \tag{B.25}$$

$\boldsymbol{K}_k$ is called a Kalman gain matrix.

B.2.5 Smoothing

Smoothing is the estimation of the state at some time in past based on the all measurements. By repeating prediction and smoothing, $\tilde{\boldsymbol{x}}_{k|k}$ is obtained. This procedure is called *forward filtering*. However, only $\tilde{\boldsymbol{x}}_{N|N}$ contains the all measurements and $\tilde{\boldsymbol{x}}_{k|k}$ ($k < N$) has information of $i = 0, \cdots, k$. In order to evaluate track state $\tilde{\boldsymbol{x}}_{k|k}$ using the all measurements, the prediction and the filtering are performed from N-th state backwardly. This procedure is called *backward filtering*. By using the covariance matrix of prediction with backward filtering $\boldsymbol{C}_{k|k+1}^{\mathrm{b}}$, the covariance matrix of k-th state is written as

$$\boldsymbol{C}_{k|n}^{-1} = \boldsymbol{C}_{k|k}^{-1} + (\boldsymbol{C}_{k|k+1}^b)^{-1}. \tag{B.26}$$

The prediction with all the measurements $\tilde{\boldsymbol{x}}_{k|n}$ is expressed as

$$\tilde{\boldsymbol{x}}_{k|n} = \boldsymbol{C}_{k|n}(\boldsymbol{C}_{k|k}^{-1}\tilde{\boldsymbol{x}}_{k|k} + (\boldsymbol{C}_{k|k+1}^b)^{-1}\tilde{\boldsymbol{x}}_{k|k+1}^b). \tag{B.27}$$

Appendix C

Hypothesis Test

A hypothesis test is performed by using the unbinned maximum likelihood estimator in order to evaluate how well the observed data agree with the signal model. In this section, the theory of the estimation [91] is reviewed briefly.

C.1 Maximum Likelihood Method

Estimation can be considered as the measurement of parameters by making use of the limited number of observations. A function of the observations which is called the *estimator* is employed for the estimation of parameters. The values yielded by using the estimator for a set of observation is called the *estimate*.

In the maximum likelihood method, the likelihood function of N observations $\boldsymbol{X} = (X_1, X_2, \cdots, X_N)$ is defined as,

$$L(\boldsymbol{X}|\theta) = \prod_{i=1}^{N} f(X_i, \theta), \tag{C.1}$$

where $f(X_i, \theta)$ is the probability density function of observation $\boldsymbol{X}$. The maximum likelihood estimation of the parameter θ is the estimation of the value $\hat{\theta}$ for which $L(\boldsymbol{X}|\theta)$ has the maximum value. It is more convenient for the estimation by using log-likelihood,

$$\ln L(\boldsymbol{X}|\theta) = \sum_{i=1}^{N} \ln f(X_i, \theta). \tag{C.2}$$

Then the likelihood equation,

$$\frac{\partial}{\partial \theta} \ln L(\boldsymbol{X}|\theta) = \frac{\partial}{\partial \theta} \sum_{i=1}^{N} \ln f(X_i, \theta) = 0, \tag{C.3}$$

is a necessary condition for the existence of a maximum in likelihood estimator. It is assumed that

$$\int f(X_i, \theta) = 1. \tag{C.4}$$

For r parameters $\boldsymbol{\theta} = (\theta_1, \theta_2, \cdots, \theta_r)$, a set of r likelihood equations are given as

$$\frac{\partial}{\partial \theta_j} \ln L(\boldsymbol{X}|\boldsymbol{\theta}) = 0, \quad j = 1, 2, \cdots, r. \tag{C.5}$$

C.2   P-value

The goodness-of-fit tests compare the experimental data with their probability density function under the null hypothesis H_0, leading the statement that if H_0 were true and the experiments are performed many times, the data would obtained as the observed data from H_0 with a probability P. This probability is called p-value. A small value of p-value means a bad fit. In order to the construct a test for the goodness-of-fit, (1)a test statistic, which is a function of the data and H_0 and (2) a way to calculate the probability of exceeding the observed value of the test statistic for H_0 are needed.

If a test statistic is expressed as $t = t(X)$ with data X, the p-value is given by

$$P = \int_{X:t>t_0} P(X|H_0), \tag{C.6}$$

where $t_0 = t(X_0)$ and $P(X|H_0)$ is a probability with X under H_0.

C.3   The Profile Likelihood Ratio

For the estimation of background and signal yields, the profile likelihood ratio is used for the hypothesis test. In this section, the profile likelihood ratio is summarized briefly.

In order to test a hypothesized value of μ, the profile likelihood ratio using likelihood function L is given by

$$\lambda(\mu) = \frac{L(\mu, \hat{\hat{\theta}})}{L(\hat{\mu}, \hat{\theta})}. \tag{C.7}$$

θ represents the parameters characterizing the shape of the probability density function. The quantity $\hat{\hat{\theta}}$ denotes the value of θ that maximizes L for specified μ. $L(\hat{\mu}, \hat{\theta})$ is the maximized likelihood function with $\hat{\mu}$ and $\hat{\theta}$.

From Equation C.7, λ satisfies $0 \le \lambda \le 1$. When λ is near to one, the data and the hypothesized value of μ have good agreement. As a test statistic,

$$t_\mu = -2\ln\lambda(\mu) \tag{C.8}$$

is often employed. Then, in order to quantify the goodness-of-fit, the p-value is defined as,

$$P = \int_{t_\mu^{\text{obs}}}^{\text{inf}} f(t_\mu|\mu)dt_\mu, \tag{C.9}$$

where t_μ^{obs} is the value of the statistic t_μ observed from the data and $f(t_\mu|\mu)$ denotes the probability density function of t_μ. When $\hat{\mu}$ is Gaussian distributed, t_μ follows a chi-square distribution.